Ultrasonic Additive Manufacturing of Steel: Process, Modeling, and Characterization

Dissertation

Presented in Partial Fulfillment of the Requirements for the Degree Doctor of Philosophy in the Graduate School of The Ohio State University

By

Tianyang Han, B.S., M.S.

Graduate Program in Mechanical Engineering

The Ohio State University

2020

Dissertation Committee:

Professor Marcelo J. Dapino, Advisor

Professor David Hoelzle

Professor Farhang Pourboghrat

Abstract

Ultrasonic additive manufacturing (UAM) is a solid-state manufacturing technology that produces near-net shape metallic parts. UAM has been demonstrated to make robust structures with a variety of material combinations such as Al-Al, Al-Ti, Cu-Cu, and Al-Cu. However, UAM welding of high strength steels has proven challenging. The focus of this work is to develop a fundamental understanding of the structure-property-process relationship of UAM steel welding through experiments and modeling.

Process and post-processing methods to improve UAM steel weld quality were investigated. A custom shear test was first developed and optimized to test the mechanical strength of UAM builds. The second study demonstrated the UAM fabrication of stainless steel 410 builds which possess, after post-processing, mechanical properties comparable with bulk 410 material. Fracture surface analyses confirm the weld quality improvement caused by increasing the baseplate temperature and the application of hot isostatic pressing (HIP) post weld. In the third study, a higher weld power is demonstrated by using a cobalt-based sonotrode coating, achieving shear strengths comparable to bulk 4130 material without post treatment.

Weld parameters for making UAM 4130 builds were optimized via a design of experiments study. Baseplate temperature of 400 °F (204.4 °C), amplitude of 31.5 μm,

welding speed of 40 in/min (16.93 mm/s), and normal force of 6000 N were identified as optimal within the selected process window. Analysis of variance and main effect plots show that normal force, amplitude, and welding speed are significant for interfacial temperature. Similar analyses show that normal force and amplitude have a statistically significant effect on shear strength.

Residual stress in UAM 4130 samples was measured for the first time using neutron diffraction. The maximum tensile residual stress for UAM 4130 is found to be relatively low at 176.5 MPa, which suggests a potentially better fatigue performance of UAM builds compared to fusion-based additive manufactured parts. FE models that describe the stress distribution and predict the fatigue performance of UAM steel builds were developed. The models predict that the fatigue cracking of the interface between the baseplate and the first layer of foil (0th interface) occurs while welding the 10th layer of 4130 steel foil, which agrees with the experimental observation. Further computational analyses indicate that a taller crack-free UAM steel build can be produced if a higher shear strength can be achieved at the 0th interface using a relatively higher welding speed and lower ultrasonic power input.

A UAM thermal model predicting the temperature rise due to heat generation from frictional sliding and plastic deformation during the UAM welding process was developed. Computational case studies indicate that a decrease in welding speed, an increase in vibration amplitude, a decrease in normal force, or an increase in baseplate temperature would lead to an increase in the peak temperature. Overall, 26 out of 32 measured peak temperatures fall into the range predicted by the UAM thermal model. The agreement between model predictions and experimental results validates the UAM thermal model.

This is dedicated to my wife and my family.

Acknowledgments

I would like to thank my advisor, Prof. Marcelo Dapino for allowing me the opportunity to work in the Smart Materials and Structures Lab. His guidance and help have been much appreciated throughout my PhD study. I would also like to thank Prof. David Hoelzle and Prof. Farhang Pourboghrat for serving on my committee. Thanks to Prof. Suresh Babu of University of Tennessee for his help and insight on microstructural analysis aspects of this research.

In addition, I would like to thank my colleagues in the Smart Materials and Structures Lab, Dr. Leon Headings for his inspiring advice and critical feedback on my research, Tommie Blackledge for proofreading my work, Dr. Paul Wolcott, Dr. Adam Hehr, Dr. Zhangxian Deng, Dr. Sheng Dong, Dr. Venkata Siva Chillara, Bryant Gingerich, Hongqi Guo, Gowtham Venkatraman, Jennifer Morris, Ningxiner Zhao, Yitong Zhou, Sai Vemula, Arun Ramanathan, Sean Chilelli, Ismail Nas, Shuting Wang, and Brad Losey for their help and support.

Thanks to Dr. Chih-Hsiang Kuo of the University of Tennessee, Dr. Niyanth Sridharan of the Oak Ridge National Lab, Dr. Aslan Miriyev of Swiss Federal Laboratories for Materials Science and Technology, and Prof. Nachum Frage of Ben-Gurion University for their contributions to the microstructural evaluations in this work. I

Lastly, I would like to thank my friends and family for their support. I would like to particularly thank my wife and best friend Yilin Li for her unconditional love and support. I could not complete this journey without her help. I am very grateful to my parents for their continuous support and encouragement throughout my academic pursuit.

Vita

January 14, 1990 .... Born - Shenyang, Liaoning, China

July, 2013 .... B.S. Mechanical Engineering,
                                          Xi'an Jiaotong University,
                                          Xi'an, Shaanxi, China

May, 2015 .... M.S. Mechanical Engineering,
                                          University of Michigan,
                                          Ann Arbor, Michigan, USA

2015-2020 .... Graduate Research Associate,
                                          The Ohio State University
                                          Columbus, Ohio, USA

Publications

Research Publications

L. Asaf, A. Miriyev, N. Sridharan, T. Han, E. Tuval, S.S. Babu, M.J. Dapino, and N. Frage "Ultrasonic additive manufacturing of steel: method, post-processing treatments and properties". *Journal of Materials Processing Technology 256 (2018): 183-189.*

Z. Deng, M.B. Gingerich, T. Han, and M.J. Dapino "Yttria-stabilized zirconia-aluminum matrix composites via ultrasonic additive manufacturing". *Composites Part B: Engineering 151 (2018): 215-221.*

CH. Kuo, N. Sridharan, T. Han, M.J. Dapino, and S.S. Babu "Ultrasonic additive manufacturing of 4130 steel using Ni interlayers". *Science and Technology of Welding and Joining 24.5 (2019): 382-390.*

T. Han, CH. Kuo, N. Sridharan, L.M. Headings, S.S. Babu, and M.J. Dapino "Effect of preheat temperature and post-process treatment on the microstructural and mechanical properties of stainless steel 410 made via ultrasonic additive manufacturing". *Material Science and Engineering: Part A 769 (2020): 138457.*

T. Han, CH. Kuo, N. Sridharan, L.M. Headings, S.S. Babu, M.J. Dapino "Effect of weld power and interfacial temperature on mechanical strength and microstructure of carbon steel 4130 fabricated by UAM". *Manufacturing Letters 25 (2020): 64-69.*

T. Han, L.M. Headings, R.Hahnlen, and M.J. Dapino "Design of experiments determination of optimum parameters for ultrasonic additive manufacturing of carbon steel 4130". *Journal of Manufacturing Science and Engineering, under review.*

T. Han, M.B. Gingerich, L.M. Headings, and M.J. Dapino "Evaluation and application of a shear test method developed to characterize the strength of ultrasonic additive manufactured materials". *In preparation.*

T. Han, L.M. Headings, R.Hahnlen, and M.J. Dapino "Neutron diffraction residual stress measurement in carbon steel 4130 fabricated by ultrasonic additive manufacturing". *In preparation.*

T. Han, L.M. Headings, R.Hahnlen, and M.J. Dapino "Fatigue prediction during ultrasonic additive manufacturing of steels". *In preparation.*

T. Han, L.M. Headings, R.Hahnlen, and M.J. Dapino "Thermal modeling of ultrasonic additive manufacturing". *In preparation.*

Fields of Study

Major Field: Mechanical Engineering

    Studies in:

        Ultrasonic Additive Manufacturing
        Finite Element Method
        Mechanical Characterization

Table of Contents

List of Tables

List of Figures

Chapter 1

Introduction

Overview

Vehicle weight reduction is widely recognized as an effective method to address the increasing concerns about greenhouse gas emissions, fuel consumption, and battery range. It is found that 10% reduction in vehicle weight leads to 7% fuel savings [10]. In the U.S., new light-duty vehicles are required to achieve 54.5 miles per gallon (mpg) by 2025, compared with 35.5 mpg as of 2016 [11]. To accomplish such aggressive goals, redesign of the current vehicle structures, substitution of some of the materials used in vehicles with lighter composites and alloys, and integration of reinforcement fibers in steel structure are necessary. Advanced manufacturing technologies must be investigated and employed to achieve these targets. Particularly, since steel accounts for more than 50% of the weight of an average passenger car, it is of great interest to explore methods to enable light-weighting by welding steel with other metals or reinforcing steel with high-strength fibers. As such, ultrasonic additive manufacturing can provide solutions to these light-weighting challenges.

1.1 Ultrasonic Additive Manufacturing

Ultrasonic additive manufacturing (UAM), also known as ultrasonic consolidation, is a solid-state manufacturing process that combines additive welding and subtractive machining [23]. During the welding process, a rolling sonotrode is used to apply a force normal to metal foil feedstock along with ultrasonic (20 kHz) transverse vibrations. The resulting localized plastic deformation has the effect of collapsing asperities and dispersing oxides and contaminants at the welding interface, generating nascent metal surfaces that produce gapless metallurgical bonds. This welding process is repeated either next to, or on top of, the preceding layer of foils to build up a component. Normal force, vibration amplitude, weld speed, and baseplate temperature are the key parameters used to control the UAM process. After the welding is done, a computer numerical control (CNC) stage is often employed to selectively remove material and machine the part to final dimensions. The subtractive stage can also be used to make arbitrary internal features such as channels and cavities for embedding reinforcement fibers [24, 79] and thermally-sensitive materials like nickel titanium shape memory alloys [25, 28] and fiber optics [54]. A schematic of the UAM process is shown in Figure 1.1.

A key advantage of the UAM process is that it is typically performed at temperatures that are less than one half of the melting temperature of the constituent materials [39]. This enables embedding thermally sensitive materials and sensors, which is difficult to achieve with traditional fusion-based manufacturing methods. This feature also allows dissimilar material joining, such as Al-Ti [67, 78] and Al-ceramic [16], to be achieved by UAM without the creation of brittle phases.
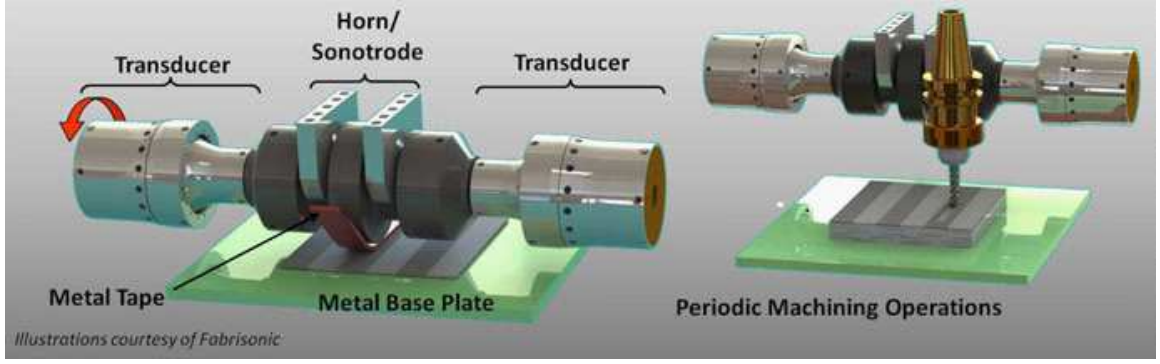
Figure 1.1: Schematic of the UAM process.

An example of a Al-ceramic welding achieved by UAM is shown in Figure 1.2. This type of metal to ceramic weld can also be achieved through fusion-based welding. However, the strength of the metal to ceramic interface achieved by UAM is 72 MPa, which is higher than the strength achieved by fusion-based welding [74]. As the joints cool down from the melting point (T_m) to room temperature in fusion welding, large residual stress is found at the metal to ceramic weld interface due to the difference in coefficients of thermal expansion. Higher temperature $(> T_m)$ and longer welding duration (minutes or hours) are also required for fusion-based welding, as compared to lower baseplate temperature ($0.5T_m$) and shorter welding duration (60 ms) for UAM [16].

1.2 Ultrasonic Additive Manufacturing of Steel

1.2.1 Background

In the early stages of research on UAM welding of steel, Tuttle [73] showed that it was possible to weld AISI austenitic stainless steel 316L (SS 316L) foil to a steel baseplate. However, no foil-to-foil bonding was achieved. The peel test, as shown in
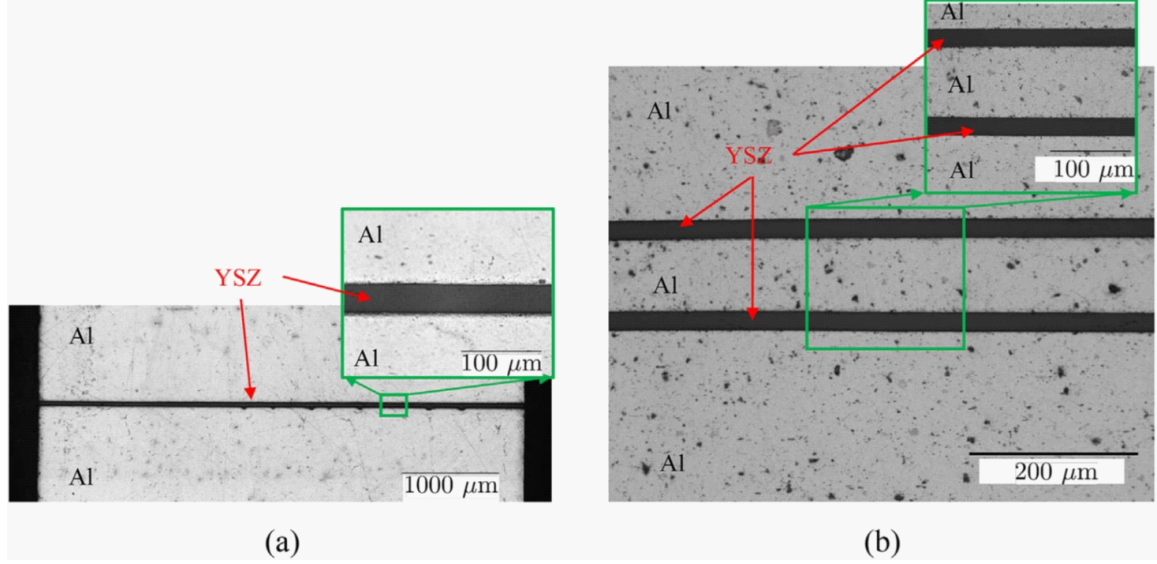
Figure 1.2: (a) Optical micrograph across the width of the Yttria-stabilized zirconia (YSZ) to Al welding interface on an as-welded shear sample and (b) optical micrograph showing two layers of YSZ films welded within an Al structure.[16]

Figure 1.3, was used to quantify the weld strength. However, this test only provides an indication of weld strength in a comparative manner. The absolute strength of UAM welds relative to bulk material is unknown. In addition to limited mechanical strength information, the optical image showing that the foil was partially bonded to the baseplate in some region also indicates the UAM steel weld is weak. This study proposed to use higher baseplate temperature to improve the weld quality, but failed to implement it due to equipment limitations.

Gonzalez et al. [22] used thinner SS 316L foils to achieve steel foil-to-foil bonding via UAM and identified the optimum parameter set for welding SS 316L based on optical images and linear weld density. A Taguchi-based design of experiments (DOE) study was conducted to find the optimal parameters in the selected process
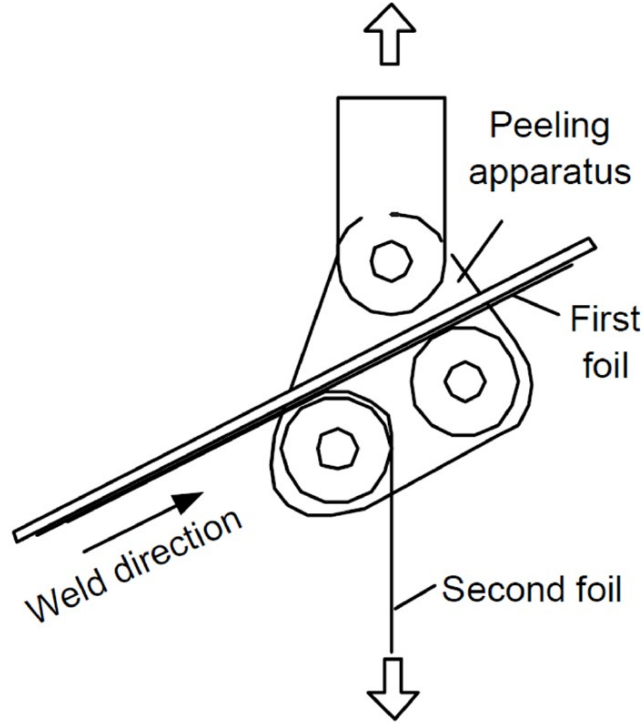
Figure 1.3: Schematic of the peel test setup [38].

window. Linear weld density (LWD), which is a measurement quantifying the void content within a UAM build through optical imaging, was used as the response variable. An example cross section image of UAM build is shown in Figure 1.4, where a measurement of the void length along the total interface length indicates the LWD. LWD is a useful method to determine whether voids exist. However, lack of voids does not mean the weld is strong. A recent study [33] has shown that the LWD is poorly correlated with mechanical strength. The effect of baseplate temperature, which is an important process parameter for UAM, has not been investigated. It is noted that these studies were conducted before the available ultrasonic power was

enhanced from 1 kW to 9 kW. The performance of early UAM technology is inferior than current technology.
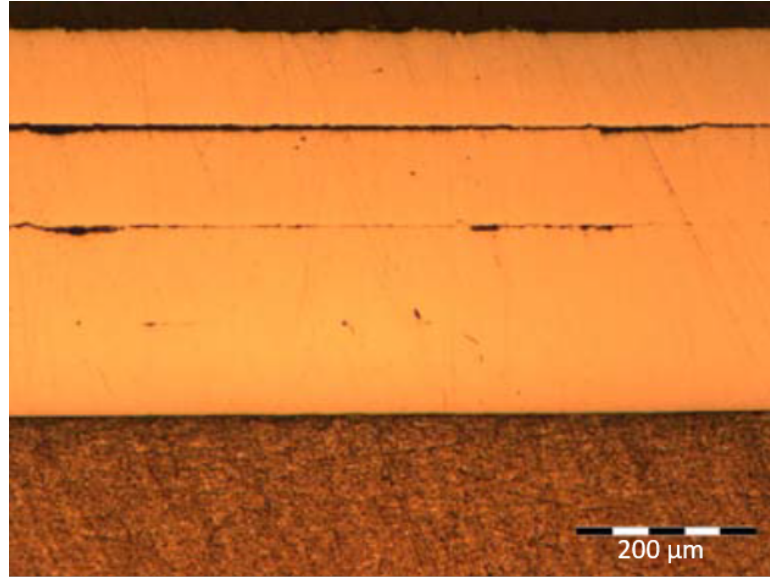
Figure 1.4: Example cross-sectional image of UAM SS 316L [22].

In a recent study by Asaf et al. [42], AISI steel 4130 was welded using a 9 kW UAM system. A few interfacial defects such as cracking and voids were observed within the as-welded UAM steel build. Two post-processing methods, hot isostatic pressing (HIP) and spark plasma sintering (SPS), were then employed to improve the structural homogeneity and mechanical properties of the builds. The HIP process applies both isostatic gas pressure and elevated temperature onto the component to reduce the porosity in metals and improve the mechanical properties. It is a common post-treatment process not just for UAM but also for other fusion-based additive manufacturing process. SPS is a current-assisted powder sintering technique, which applies pressure and heat onto the UAM build through a graphite die. It has been

6

used as a post-heat treatment method for UAM Al-Ti [78]. However, one drawback of this technique is that the graphite die may introduce carbon into the material thus affecting the material homogeneity in the z-direction.

As presented in Figure 1.5(a) and Figure 1.5(b), voids and cracks were found at the interfaces of as-welded UAM 4130. After SPS treatment, most voids and cracks are healed and mitigated. Only a small amount of voids were observed in SPS treated UAM 4130 samples, as shown in Figure 1.5(c) and Figure 1.5(d). A relatively larger
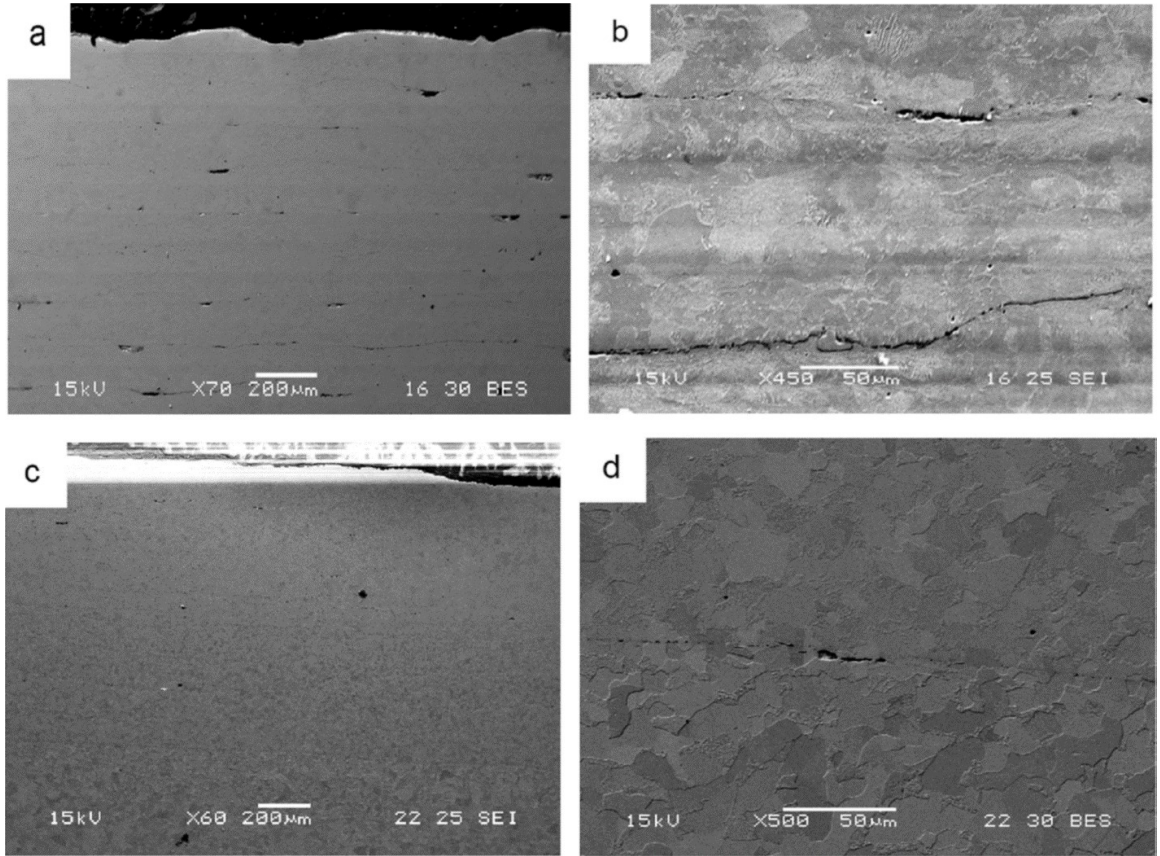
Figure 1.5: Scanning electron microscope (SEM) images of (a,b) as-welded UAM 4130 and (c,d) SPS treated UAM 4130 [42].

number of interfacial defects were observed at the interface of HIP treated UAM 4130 builds, as shown in Figure 1.6.
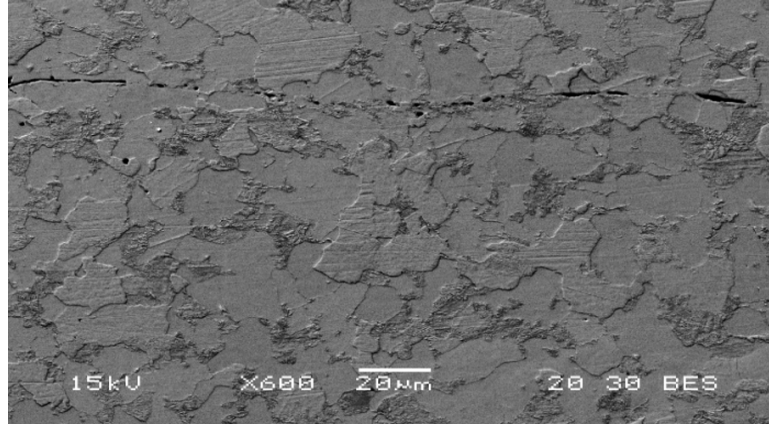
Figure 1.6: SEM images of HIP treated UAM 4130 [42].

Further microstructural analyses were done by electron backscatter diffraction (EBSD). Figure 1.7(a) shows that extensive grain refinement takes place at the interface of as-welded UAM 4130 builds. The interface can be easily located due to the obvious cracks. The interface of HIP treated UAM 4130, by contrast, can not be distinguished by EBSD analysis as shown in Figure 1.7(b). An intimate contact of the foils and grain growth were found at the interface after HIP. Similar results were found for SPS-treated UAM 4130.

As shown in Figure 1.8, a customized shear testing method was used to characterize the mechanical strength of the interface of UAM 4130 builds. This type of shear test was first applied on UAM samples by Wolcott et al. [78]. Unlike the peel test used by Tuttle [73], the shear test can provide material properties that can be used to benchmark against bulk material. Even though the shear test method is a useful
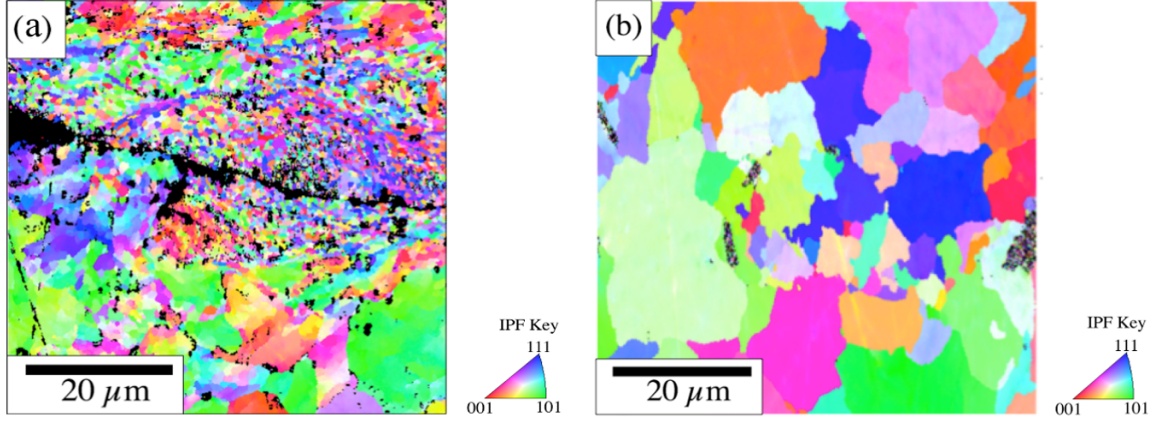
Figure 1.7: EBSD of the interface of (a) as-welded UAM 4130 and (b) HIP treated UAM 4130 [42].

tool for testing UAM samples, recent studies have revealed that it could suffer from high variability. Further validation and development of this test method is needed to standardize it for UAM application.

The shear test results show that both treatments increase the average maximal shear load by more than 100% compared to as-welded UAM 4130. However, the shear strength is not obtained and benchmarked to solid material in this study. The higher standard deviation of post treated builds also indicates some variation produced by the two treatment methods, which need further investigation.

In a recent study by Kuo et al. [40], a method to achieve UAM steel-steel weld with Ni interlayers was proposed. The concept is to use interlayers between the steel layers and then dissolve the interlayer material into the steel layers with a post-weld heat treatment (PWHT). UAM of soft-hard dissimilar metal combinations such as steel-tantalum [65] and steel-aluminum [66] have been demonstrated. Most of the plastic deformation was found on the softer material and metallurgical bonding was formed

9
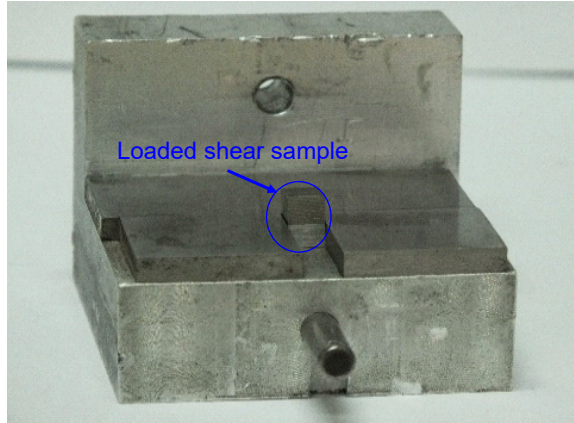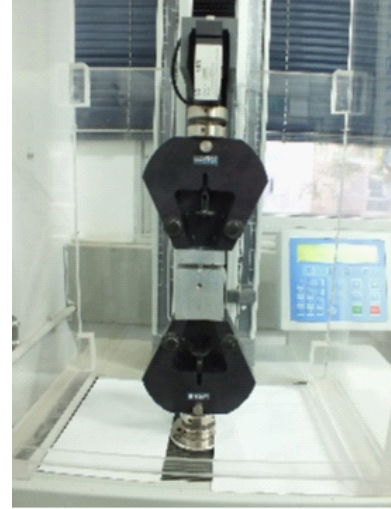
Figure 1.8: (a) Half of the shear test fixture with a loaded shear sample and (b) the shear fixture mounted in the load frame [42].

at the interface. However, neither tantalum or aluminum can be fully diffused into steel. The formation of a brittle intermatallic layer during PWHT is another concern for these material combinations. Thus, a new interlayer material selection is based on the following criteria: (1) lower hardness than steel, (2) higher melting point than UAM processing temperatures, (3) reduced intermetallic formation tendency during PWHT, and (4) ability to dissolve into steel.

With a review of Fe-X binary phase diagrams with different alloying additions X, nickel was then selected as the interlayer material based on its good solubility in body-centered cubic (BCC) ferrite and face-centered cubic (FCC) austenite structures. One major challenge to diffuse Ni into Fe is the proper selection of temperature for PWHT. Lower PWHT temperatures lead to incomplete diffusion. Higher PWHT temperatures result in enhanced diffusion. However, if the temperature is higher

10

than the upper critical temperature Ac3, the diffusivity of Ni in a steel matrix would drop due to the allotropic transformation of BCC to FCC [47, 14]. Moreover, higher temperatures may also lead to the formation of Kirkendall voids due to the significant difference in diffusivity of Ni and Fe at the weld interface, which will lower the weld strength. Thus, one purpose of this study is to find suitable PWHT temperatures to fully diffuse Ni into Fe.
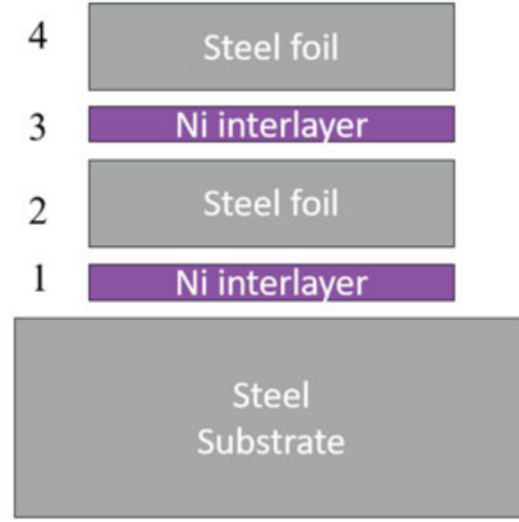
Figure 1.9: Schematic of steel-Ni bilayer arrangement [40].

In this study by Kuo et al., 0.127 mm (0.005 inch) thick annealed AISI 4130 steel foils and 0.025 mm (0.001 inch) thick Ni 201 foils was welded using UAM. As shown in Figure 1.9, a bilayer arrangement was used where a steel and Ni layer are welded in one step. It noted that the sonotrode is only in contact with the steel layer in this arrangement.

A thermodynamic calculation was then performed using THERMOCALC and DICTRA to simulate the post weld heat treatment. A PWHT temperature of 1000 K
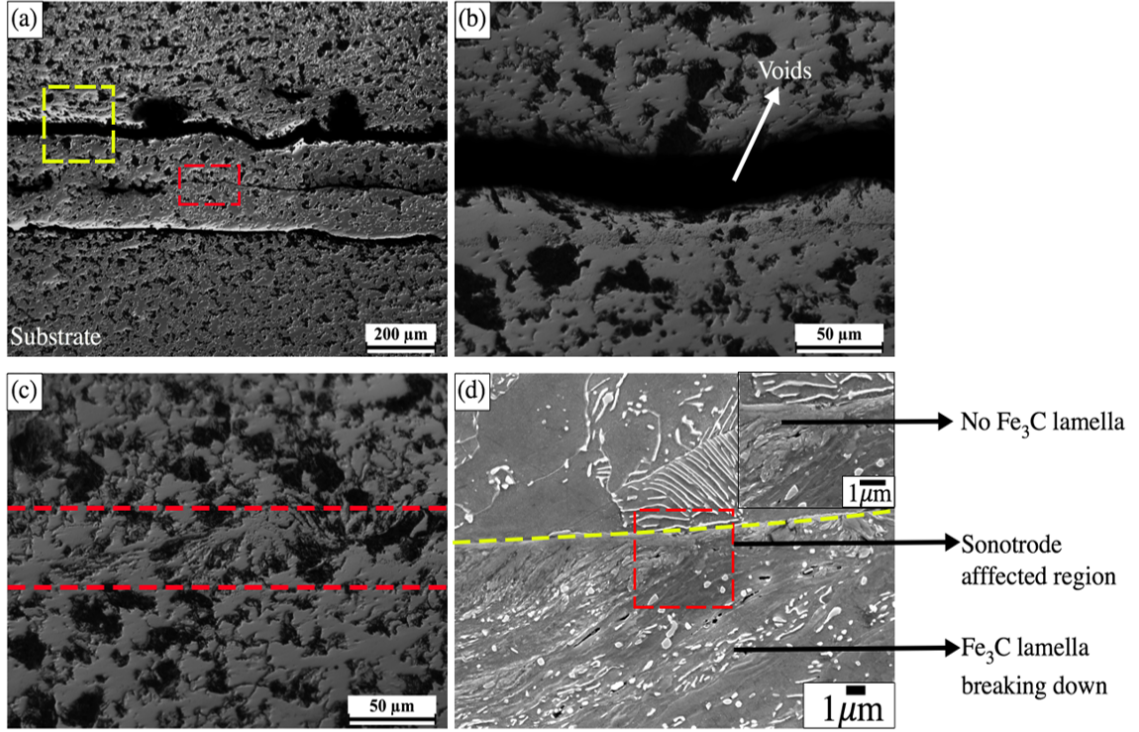
Figure 1.10: Optical image of (a) welding interface of as-welded UAM 4130 without Ni interlayers, (b) unbonded region at a higher magnification, (c) bonded region at a higher magnification, and (d) SEM image of the bonded region [40].

and a holding time of 1 hour, 2 hours, and 10 hours were selected for experimental validation. Microstructural analyses were done by optical imaging, SEM, and EBSD for UAM 4130 with and without Ni interlayers. As presented in Figure 1.10, bonded and unbonded zones at the interface of as-welded UAM 4130 without Ni interlayer were identified. The unbonded zone is formed due to the lack of plastic deformation, which is confirmed by the higher magnification image shown in Figure 1.10(c). In contrast, the bonded zone is formed due to extensive plastic deformation, which can be inferred from the decomposition of cementite laths near the interface, as shown in Figure 1.10(d).
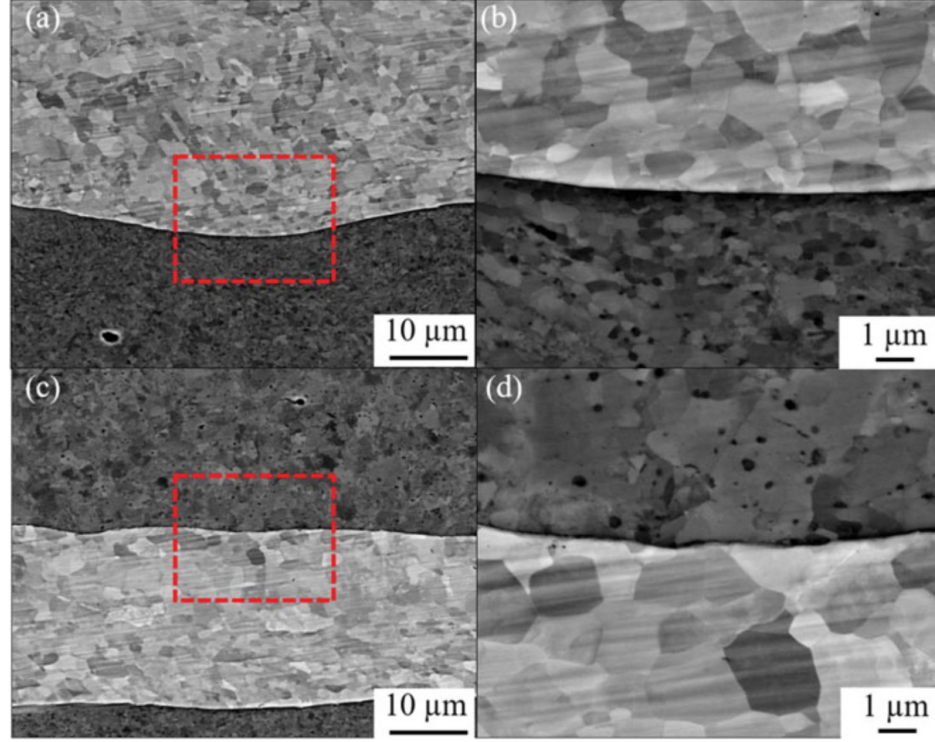
Figure 1.11: SEM images of the welding interface of as-welded UAM 4130 with Ni interlayers: (a) rough steel interface area at a lower magnification, (b) rough steel interface area at a higher magnification, (c) flat steel interface area at a lower magnification, and (d) flat steel interface area at a higher magnification [40].

SEM images of the weld interface of UAM 4130 with Ni interlayer are presented in Figure 1.11. Fewer voids and non-uniform grain refinement were found at the Ni-steel interface. Grain refinement is found to be more pronounced in the rough surface region where the Ni flows along the contours of the steel, as shown in Figure 1.11(a). On the other hand, less refinement was found near the flat surface region, as shown in Figure 1.11(c).

Further EBSD analyses are presented in Figure 1.12. The ferrite grains at the interfaces in the as-welded UAM 4130 without Ni interlayers are much finer compared

13
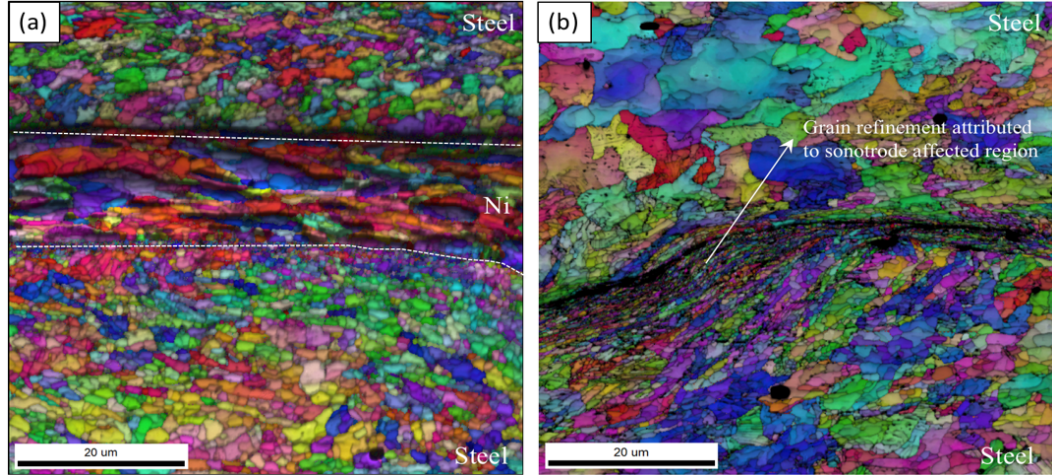
Figure 1.12: EBSD of the interface of (a) as-welded UAM 4130 with Ni interlayers and (b) as-welded UAM 4130 without Ni interlayers [40].

to the as-welded UAM 4130 with Ni interlayers. This reduction in grain size may result from the higher power input applied to the UAM steel samples without Ni interlayers.

Micrographs of the heat treated and as-welded samples with Ni interlayers are presented in Figure 1.13. The SEM images show contrast at the Ni-Fe interfaces, which suggests the inter-diffusion of Ni into steel. In addition, there is a zone in the steel adjacent to the Ni foil showing a different contrast, which is attributed to the formation of an FCC layer. Even though significant grain growth in the Ni layer occurred during the heat treatment, the grain growth in the FCC zone was limited. The extent of the inter-diffusion is measured using energy dispersive X-ray spectroscopy (EDS). As presented in Figure 1.13, the EDS micrographs show that an inter-diffusion zone about 10 μm for the sample, which has been treated for 10
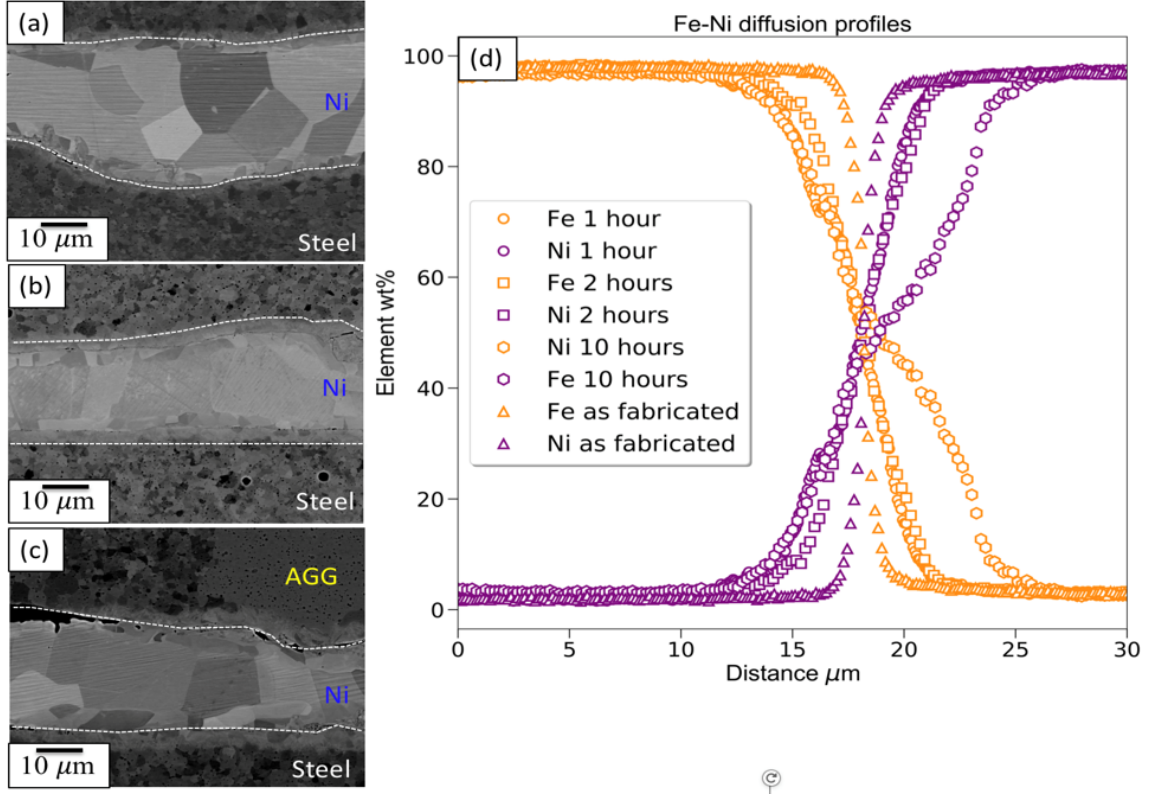
Figure 1.13: SEM images of the UAM Ni-steel welding interfaces after heat treatment at 1000 K for (a) 1 hour, (b) 2 hours, (c) 10 hours, and (c) EDS line scans of interdiffusion zones of Fe (purple) and Ni (orange) in the as-welded and PWHT samples [40].

hours. This suggests that a Ni interlayer with a thicknesses < 10 μm may completely dissolve in the steel leading to the formation of a steel-steel bonding interface.

1.2.2   Problem Statement

UAM has been proven to produce robust similar metal builds in Al-Al [33, 80, 63, 24] and Cu-Cu [68] material systems. However, UAM welding of high strength steel remains challenging.

As-welded UAM steel possesses insufficient weld strength, about 50% that of the bulk material. To take advantage of the full potential of UAM to make steel joints, process development to improve the strength of UAM steel to be comparable to that of bulk material is necessary. It is speculated that increased process temperature or increased ultrasonic weld power would improve the weld strength, where increased process temperature reduces the yield strength of the material and increased weld power induces intensified high strain rate deformation. However, currently both the power and temperature inputs are restricted by practical limits. When ultrasonic power input is increased, the top of the steel foil tends to weld to the sonotrode due to galling, a form of adhesive wear shown in Figure 1.14. To avoid this phenomenon, the power input must be restricted, which limits the resulting strength of UAM 4130 steel builds. A baseplate temperature of 204 °C, which is also the upper baseplate temperature limit of commercial UAM systems, can be used to soften the material. However, this baseplate temperature may not be sufficient to achieve a weld with shear strength comparable to that of bulk steel. Post heat treatment methods may be needed to further improve the strength of UAM steel builds.

During UAM steel welding, undesired cracking can occur between the baseplate and the first foil as build height increases. An example image of cracking that occured at that interface is presented in Figure 1.15. There is no work in the literature on characterization of UAM cracking phenomena or proposed methods to mitigate them. Therefore, it is necessary to develop understanding of the causes of cracking through modeling and experiments to propose strategies to mitigate cracking. The expectation is that lowering welding parameters (normal force, welding speed, and welding amplitude), especially welding amplitude, will mitigate cracking. However,
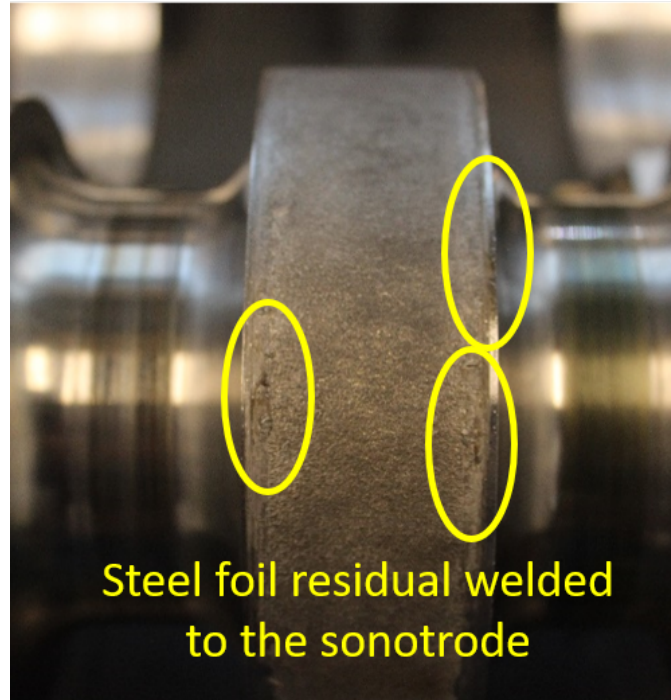
Figure 1.14: Image of galling that occurred during UAM steel welding.

the weld process needs to be optimized to maintain interfacial strength while reducing fatigue stress and cycles. Analytical models to further aid the design of the UAM steel welding process are also needed.

This dissertation pursues a fundamental understanding of the structure-property-process relationship of UAM steel welding. AISI martensitic stainless steel 410 (SS 410) foil and AISI carbon steel 4130 foil will be used as the material platform for investigation. The understanding of these relationships can then be extended for other materials. Strategies and methods to achieve robust UAM steel welding will be proposed first. A method to use a higher preheat temperature (still below melting temperature) and post heat treatment methods such as hot isostatic pressing (HIP) to
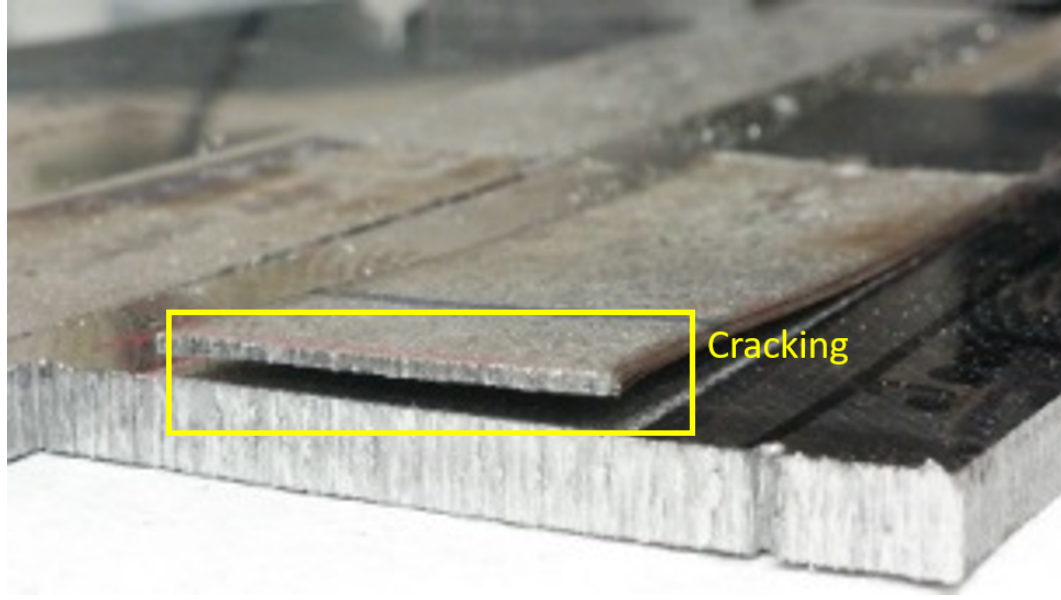
Figure 1.15: Image of cracking that occurred during UAM steel welding.

improve the mechanical strength of UAM steel builds will be developed. An alternative method to achieve robust UAM steel welds by using a cobalt-based hard-facing alloy coated sonotrode to increase the galling threshold and allow a higher power input will be studied. To further investigate the effect of weld parameters on weld quality of UAM steel, a design of experiments (DOE) study will be conducted.

Finite element (FE) models that describe the stress distribution and predict fatigue performance during welding will be developed to aid the design of welding parameters to mitigate cracking. Neutron diffraction residual stress measurement will be attempted to gain a deeper insight into the effect of residual stress on the fatigue performance of UAM steel builds. Since recent work shows that a higher baseplate temperature improves UAM weld quality for steels, understanding the effect of temperature on the interfacial strength is critical for optimizing the weld process. There

is work in the literature on measurement of weld temperature for aluminum as well as models for temperature rise based purely on frictional sliding or plastic deformation. In addition to involving conflicting assumptions, neither modeling approach has been well validated; consequently, a UAM thermal model will be developed and validated.

1.2.3 Dissertation Outline

The outline of this dissertation is as follows. Process development studies including the application of an increased baseplate temperature, post heat treatment HIP, and an increased power input to achieve robust UAM steel welds are presented in Chapter 2. A DOE study based on a Taguchi L16 design array to investigate the influence of parameters including baseplate temperature, amplitude, welding speed, and normal force on the interfacial temperature and shear strength of UAM steel is presented in Chapter 3. Neutron diffraction residual stress measurements and the development of FE models to predict fatigue performance of UAM steel are introduced in Chapter 4. The development and validation of a UAM thermal model to predict interfacial temperatures of UAM steel are presented in Chapter 5. Lastly, key findings and contributions of this work as well as discussion of future work are summarized in Chapter 6.

Chapter 2

Process Development for UAM Welding of Steel

Overview

The focus of this chapter is on benchmarking the mechanical strength of UAM steel against bulk materials, proposing and identifying process and post-process methods to improve UAM steel weld quality. The first study introduces the design, anaylsis, and application of a custom shear test method, which is used to characterize the mechanical strength of UAM builds. The second study investigates the effect of preheat temperature and post-process treatment HIP on the mechanical strength and microstructure of UAM steel. The third study examines the influence of the weld power and interfacial temperature.

2.1 Development and Analysis of a Shear Test Method to Characterize the Strength of Ultrasonic Additive Manufactured Materials

Even though many mechanical test methods have been employed to characterize UAM-made materials, there are no existing standards. Since the UAM-fabricated builds have a unique laminated construction, quantification of the interfacial strength between layers is critical to understand the strength of entire UAM structures. In previous UAM research, peel testing [38, 12] has been used to provide comparative interfacial strength information. This test is easy to conduct, but the test results cannot be compared with bulk material properties; it also does not do well enough to break a strong bond. Push pin testing [84] is another testing method that provides comparative interfacial strength information. However, the test cannot provide material properties to benchmark against solid material. Test specimens for push-pin testing requires more materials. The Z tensile test has been also used to assess the weld quality of UAM builds. However, Z tensile tests cannot estimate the strength of a specified interface and cost a longer time to make the specimens [33]. Thus, a new testing method to characterize the mechanical strength of a specific interface of UAM builds is needed.

Among all mechanical tests, shear testing is selected due to its capability to provide absolute interfacial strength information that can be benchmarked against bulk material. Shear tests can be classified as direct transverse shear and pure torsional shear depending on the way that the shearing load is applied. A torsional shear test is usually used to characterize the shear behavior and properties of materials. Since the torsional shear sample cannot assess the strength of a specified interface, this
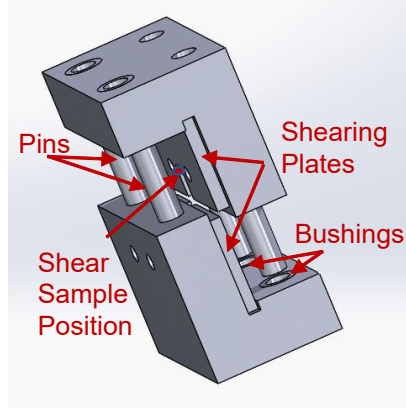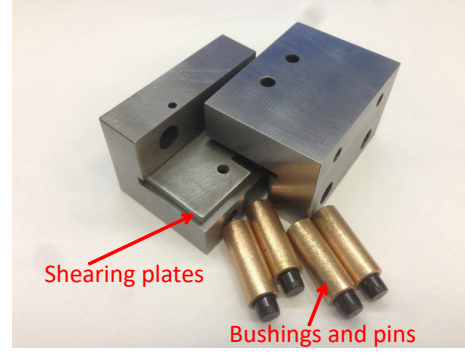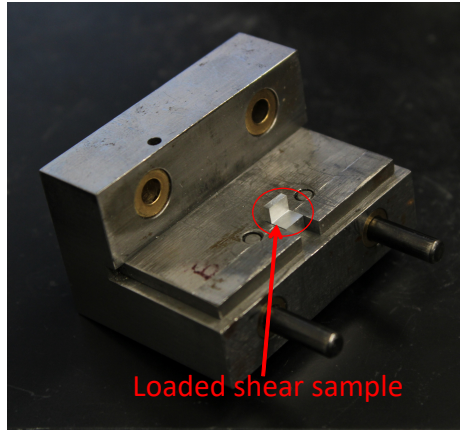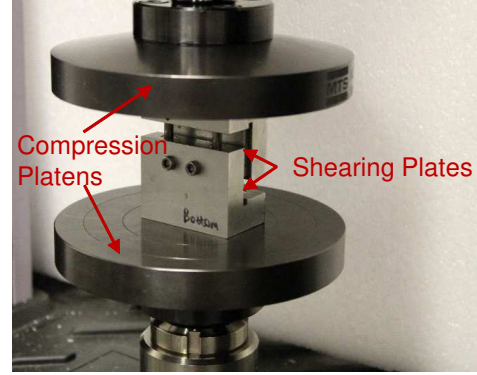
Figure 2.1: Shear test design including (a) conceptual schematic of shear fixture, (b) image of disassembled parts, (c) half of the shear fixture with loaded shear sample, and (d) experimental setup of the shear test with loaded sample.

test method is not utilized in this study. The transverse shear test, which provides an approximate estimate of the shear strength of the material, is selected instead. There are a number of transverse shear tests in the literature such as the double notched shear test [56] and the Iosipescu test [34, 53]. However, a mixed failure modes are often reported for the double notched shear test that the crack does not always propagate along the desired interface. The Iosipescu test requires a sample

height that is 30 times the typical height of a UAM steel build. Hence, a custom shear test method was developed. This test method allows localized characterization of a specified interface at different regions of the UAM build. This shear test was first introduced by Wolcott et al [78]. It has already been adopted in several UAM studies [42, 26, 27, 40, 16]. However, the development, validation, and analysis of this method were never summarized and presented. In this study, the shear test method was first validated with solid cast Al materials. Then a finite element (FE) model was built to understand the influence of different shape and dimension including full-size and stepped sample design on the shear test results. Finally, the shear test method was applied to UAM-made Al and steel.
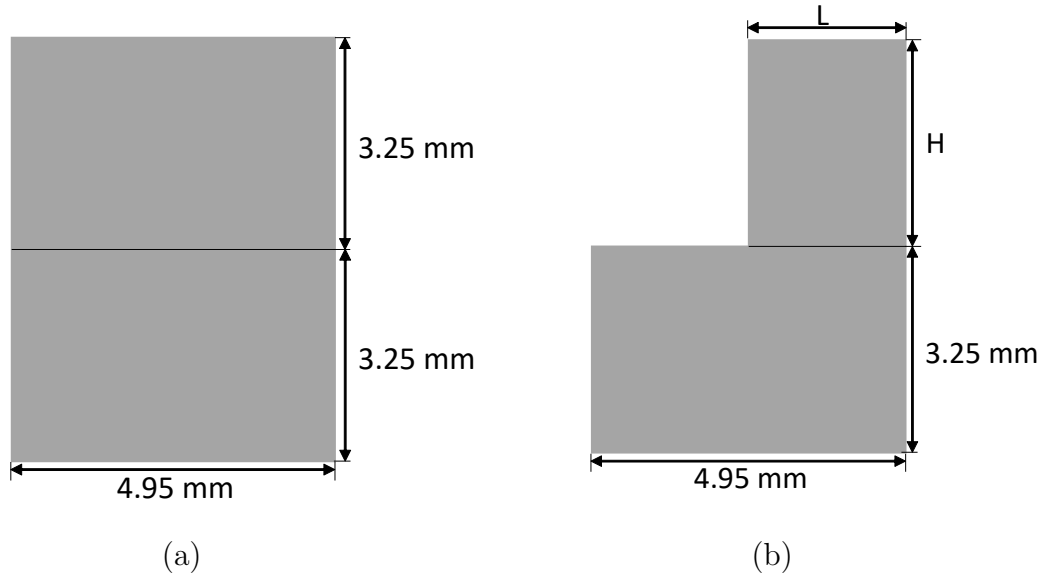
Figure 2.2: Schematics of (a) full-size sample and (b) stepped sample. The desired shearing interfaces are marked with solid black lines.

2.1.1 Design of the Shear Test Method

A schematic of the shear fixture is shown in Fig. 2.1(a). The fixture is composed of two identical "L" shape shearing blocks and two identical shearing plates. Shearing blocks are made of 4130 steel and each of them is assembled with two steel pins and two copper bushings as shown in Fig. 2.1(b). Shearing plates are made of heat treated S7 tool steel. The UAM shear sample is placed into the slots in the shearing plates, as presented in Fig. 2.1(c). During testing, the shearing blocks are pressed by the compression platens of the load frame as shown in Fig. 2.1(d). The shearing blocks then slide together to shear the sample at the interface between the shearing plates.

Table 2.1: Shear strength of solid Al 6061 T6.

Sample	Shear strength of full-size samples (MPa)	Shear strength of stepped samples (MPa)
1	238.0	220.8
2	231.6	205.8
3	228.9	205.2
4	231.5	208.7
5	233.2	218.8
Average	232.6	211.9
Reference [3]	207	207

The shear strength is defined as $\tau = F/A$, where F is the maximum compression force on the fixture during the shear test process that is read from the load frame and A is the initial cross-sectional area of the sample loaded in shear, which is measured with a micrometer.
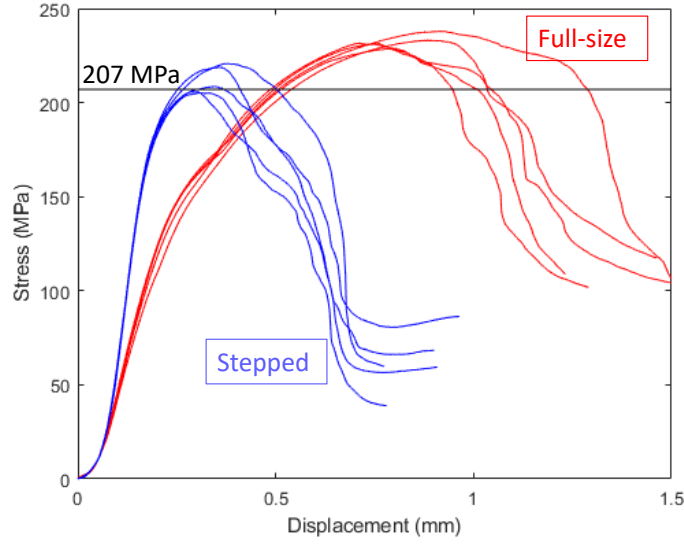
Figure 2.3: Individual stress versus displacement curves of full-size and stepped samples with the reference value plotted as a solid black line.

2.1.2 Validation of the Shear Test

Solid Al 6061 T6 with a known shear strength [3] was tested to verify the accuracy of the proposed shear test method. The nominal width of a shear sample is fixed at 4.95 mm (0.195 inch). The length in the shearing direction and the height of the sample need to be optimized. As shown in the schematic in Fig. 2.2(a), a shear sample with a length of 4.95 mm (0.195 inch) and a height of 3.25 mm (0.128 inch) is defined as a full-size sample. As shown in Fig. 2.2(b), a shear sample with a length of L that is smaller than 4.95 mm and a height of H that is no larger than 3.25 mm is defined as a stepped sample. The designated shearing interfaces are marked with solid black lines. The expectation is that the stepped sample may provide a more accurate and reliable measurement than the full-size sample because the travel distance is short and a lower bending moment is anticipated. To verify this assumption, full-size samples as well

25
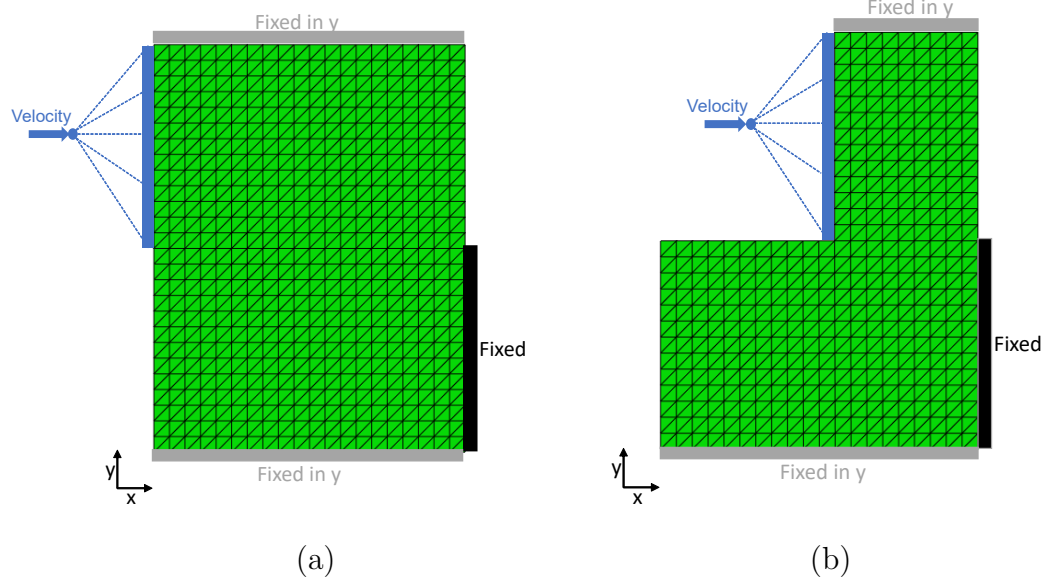
Figure 2.4: Boundary conditions and mesh details of (a) full-size sample and (b) stepped sample.

as stepped samples with an arbitrary width of 2.24 mm and a full height of 3.25 mm are machined from Al 6061 T6. The test was then conducted on five samples for each geometry. A summary of the shear test results for both geometries is provided in Table 2.1. Individual stress curves are presented in Fig. 2.3, with the reference value indicated by a solid black line. As shown, the testing of the stepped condition gives a shear strength measurement of 211.9 MPa, which is a 2.3% overestimation compared to the reference value of 207 MPa. By contrast, the testing of full-size samples generates an measurement of 232.6 MPa, which is a larger overestimation of 12.4%.
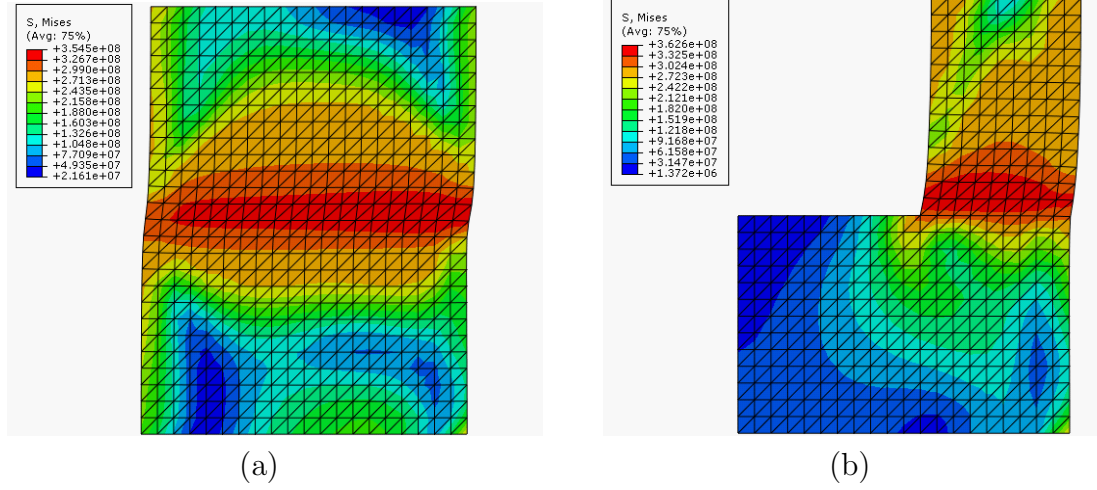
Figure 2.5: Stress distribution map of (a) full-size sample and (b) stepped sample.

2.1.3 Finite Element Modeling of the Shear Test

To further understand the physical meaning of the stress curve and estimate the stress distribution in the shear sample, a two-dimensional finite element (FE) model was developed in Abaqus. The mesh details and boundary conditions of the model are shown in Fig. 2.4. Triangular element is used in this study due to its better performance during element deletion caused by shear damage. The mesh is iteratively refined until the balance between convergence and the peak load variation is reached. The bottom half of the right surface of the material is fixed. A boundary velocity of 0.02 mm/s is applied a virtual control point as shown in Fig. 2.4. Then, a structural distributing coupling is defined between the point and the top half of the left surface. The motion defined on the point is used to simulate the compression from the load frame. The top and bottom surfaces of the material are constrained in the y direction. The shear stress is calculated as $\tau = F_r/A_e$, where F_r is the reaction force applied on the fixture and A_e is the effective shearing area.

27

The elasticity and plasticity of Al 6061 T6 are used to define the material. The model presumes that the equivalent plastic strain at the damage $\bar{\epsilon}_S^{pl}$ is defined as a function of the shear stress ratio θ_S and strain rate $\dot{\epsilon}^{pl}$ [59]. The criterion for shear damage initiation is satisfied when

$$\omega_S = \int \frac{d\bar{\epsilon}^{pl}}{\bar{\epsilon}_S^{pl}(\theta_S, \dot{\epsilon}^{pl})} = 1, \tag{2.1}$$

where ω_S is a state variable that increases proportional to the incremental change in equivalent plastic strain. In this study, these shear damage properties for Al 6061 T6 are calibrated from a trial and error process and defined as presented in Table 2.2.

Table 2.2: Shear damage properties used for modeling Al 6061 T6.

Fracture strain $\bar{\epsilon}^{pl}$	Shear stress ratio θ_S	Strain rate $\dot{\epsilon}^{pl}$
0.1	0.33	2

The stress distribution map prior to the shear failure is shown in Fig. 2.5. The stress concentrated in the desired regions in both the full-size and stepped samples. Simulated shear stress versus displacement curves are compared to experimental results for the full-size and stepped samples in Fig. 2.6. For the full-size sample, the maximum shear stress is measured as 237.0 MPa and simulated as 210.0 MPa. For the stepped sample, the maximum shear stress is measured as 207.8 MPa and simulated as 214.8 MPa. The simulated maximum stress is close to the measured value for both cases. The simulated displacement is smaller than the measured displacement because the simulation assumes perfect sample geometry and alignment with the shear fixture as well pure transverse shear during testing. However, in practice, geometries are not

perfect and small angle rotation and bending may happen simultaneously with transverse shear loading. Therefore, the measured displacement does not have a precise physical meaning with regards to the material properties of the sample. Similar to other transverse shear testing methods, this miniature shear method can provide a pretty close approximation of the shear strength using peak shear load. However, it is not the best tool to estimate the shear stress versus displacement curve. Of note, the initial slope of the simulated shear stress versus the displacement curve remains constant since a perfect contact scenario is assumed. However, the initial slope of the experimental curve gradually increases from 0 to a constant value, which may result from the initial engagement and contact between the shearing plates and the samples.
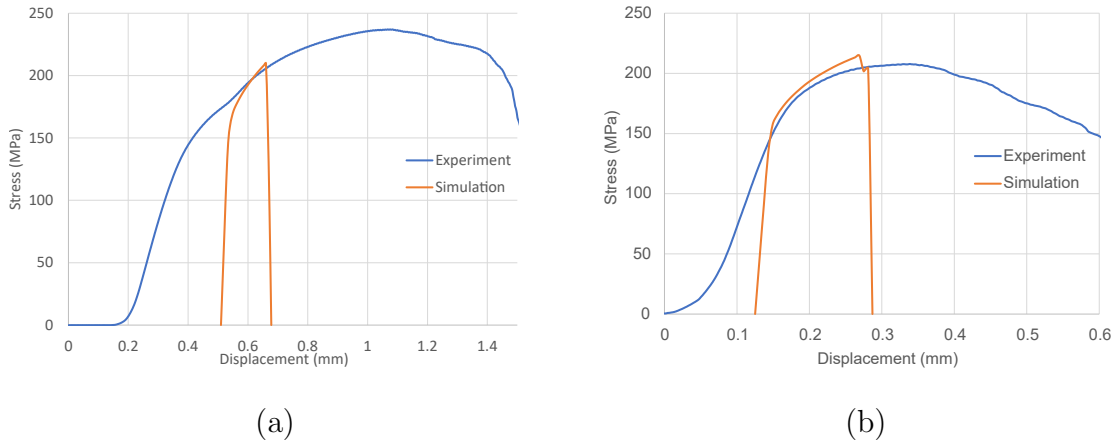
Figure 2.6: Comparison of shear test results between experiments and FE simulations of (a) full-size sample and (b) stepped sample.

2.1.4 Application of the Shear Test on UAM samples

Shear testing of the solid Al 6061 T6 samples has demonstrated the feasibility of this test method and the use of the stepped shape. The dimensions of the length

L and the height H need further optimization. It is expected that a shorter length requires a shorter traveling distance and would be more accurate. However, this dimension is constrained by practical limits. Since the stepped sample is machined to its final dimension using CNC machining, the stepped part would be sheared off during machining if the length is too short. Thus, after a trial and error process, the minimal length is found to be 1.42 mm (0.056 inch). It is also speculated that a full height stepped part of 3.25 mm tall would prevent sample rotation within the fixture during testing and provide a more accurate measurement. But, the full height sample requires extra cost in time and material to make the UAM sample. Moreover, for certain material such as steels, undesired cracking can occur as build height increases, which make it difficult to make full height samples under current processing conditions. To understand if build height affects the test results, shear samples of UAM-made Al 6061 were produced with short, middle, and tall heights as shown in the schematics of Fig. 2.7.
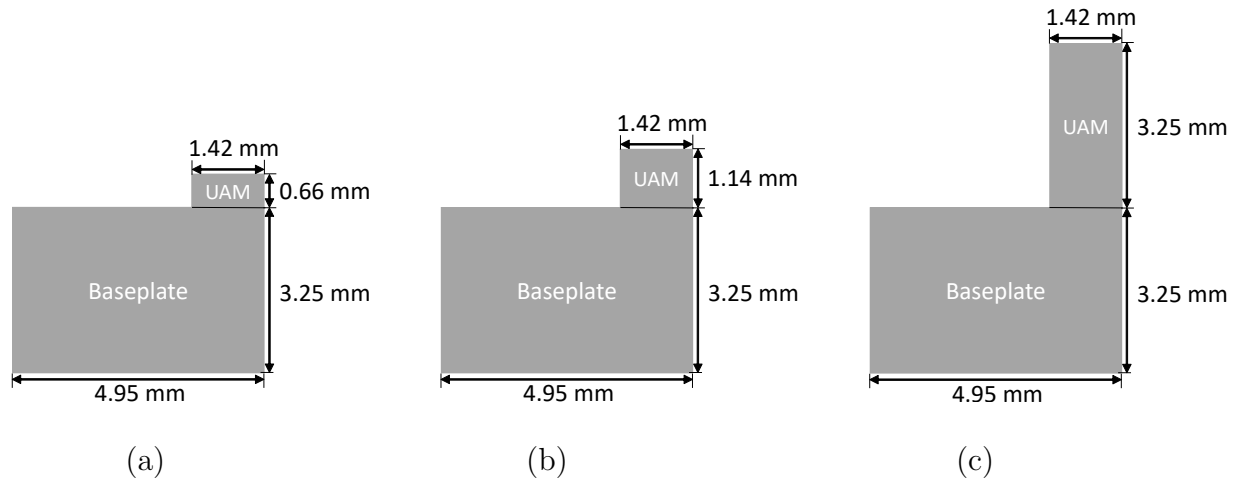
Figure 2.7: Schematic of (a) short height, (b) middle height, and (c) tall height shear samples with nominal dimensions.

Table 2.3: Process parameters used to weld Al 6061 H18 and carbon steel 4130.

Parameters	Al 6061 H18	steel 4130
Normal force (N)	4000	6500
Vibration amplitude (μm)	35.0	30.0
Weld speed (mm/s)	85	21
Baseplate temperature (°C)	24	204

Table 2.4: Shear test results for UAM Al 6061 H18.

Sample	Shear strength of short height sample (MPa)	Shear strength of middle height sample (MPa)	Shear strength of tall height sample (MPa)
1	88.9	90.0	82.8
2	82.2	85.6	81.1
3	78.5	84.0	78.9
4	89.0	87.2	78.4
Average	84.7	86.7	80.3
Std	4.5	2.2	1.7

All samples were made using a Fabrisonic SonicLayer 4000 9 kW UAM system. Twenty-two layers of 0.152 mm (0.006 in) thick, 25.4 mm (1 in) wide Al 6061 H18 foils were welded onto a 6.35 mm (0.25 in) thick Al 6061 T6 baseplate. Welding parameters used to make these builds are shown in Table 4.1. A 0.25 inch square end mill was used to extract the shear samples from the UAM build. Then, the shear samples were fixed in a high precision vise and machined to their final dimensions. Images of the

shear samples with varied height are shown in Fig. 2.8. Four shear samples for each case were tested using an MTS C43.504 50 kN load frame. The shear test results are shown in Table 2.4. Despite the large height variation of 78%, the measured shear strength of UAM Al 6061 H18 varies little as 8%. These results have demonstrated the viability of using short height stepped shear samples to characterize the shear strength of UAM samples.

(a)   (b)   (c)
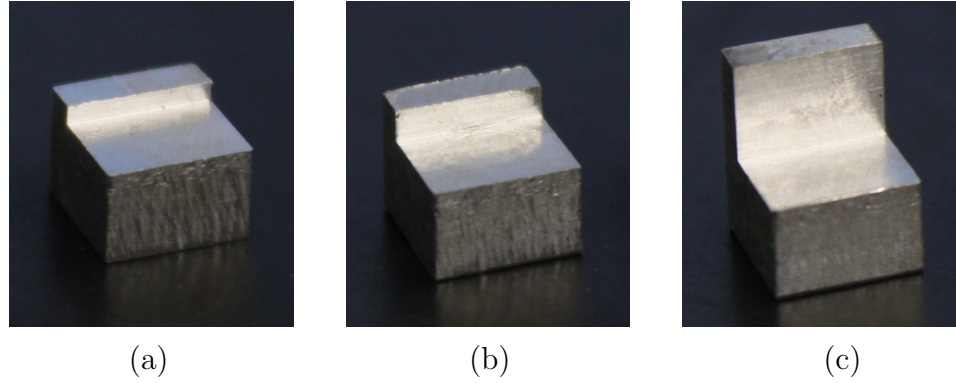
Figure 2.8: Machined shear samples of UAM Al 6061 H18 with (1) short, (2) middle, and (3) tall height dimensions as specified in Fig. 2.7.

To further expand the application of this shear test to the UAM steel domain, UAM 4130 steel builds were made using the parameters shown in Table 4.1. Nine layers of 0.127 mm (0.005 in) thick, 25.4 mm (1 in) wide annealed carbon steel 4130 foils[1] were welded onto a 6.35 mm (0.5 in) thick ASTM A36 carbon steel baseplate. Four shear samples with the dimensions of the middle height sample shown in Fig. 2.7 were made and tested. The test results are shown in Table 2.5. As presented, the low

[1]The welding width of the sonotrode is 20.3 mm (0.8 inch).

standard deviation (std) as 13.4 MPa proves the validity of the data and indicates the viability of this method for testing different UAM materials.

Table 2.5: Shear test results for UAM 4130.

Sample	Shear strength (MPa)
1	156.3
2	158.0
3	142.1
4	178.4
Average	158.7
Std	13.4

2.1.5 Summary

A custom shear test method was developed to characterize the mechanical strength of a specific interface of UAM builds. The shear test method was first validated with solid cast Al 6061 T6. Testing of stepped samples gives 2.3% error compared to the reference, while testing of full size samples generates 12.4% error. A finite element (FE) model was then built to understand the influence of different sample shapes on the shear test results. The simulated stress versus the displacement curve matches better with the experimental curve for the stepped sample. These results are consistent with experimental results, which demonstrate that the stepped sample has a better performance than the full-size sample. Finally, the shear testing method was applied to UAM Al 6061 H18 and UAM 4130 steel and consistent measurements

were obtained. The results also indicate that the height of shear samples has little effect on the measured shear strength.

2.2 Effect of Preheat Temperature and Post-process Treatment on the Microstructure and Mechanical Properties of UAM SS 410

The purpose of this study is to investigate the effect of pre-heat baseplate temperatures and post-process HIP on the mechanical properties and the microstructure of UAM-fabricated SS 410. Even though different preheat temperatures were shown not to have a significant impact on the bond quality of UAM structures in a design of experiment study on Al alloys [80], there is evidence that preheat temperatures may be beneficial for steel welding [73, 22]. Thus, varied pre-heat temperatures are used in this study to investigate their effect on UAM steel weld quality. Furthermore, the influence of HIP as a post-process method to improve mechanical and microstructural properties of UAM steel builds is investigated. As introduced in Chapter 2.1, a custom shear test was designed to test the mechanical strength of UAM samples that were built under different conditions. The shear strength of UAM-fabricated SS 410 was benchmarked against bulk SS 410. An optical microscope, SEM and EBSD analyses, as well as microindentation and nanoindentation tests, were used to gain deeper insights into the effects of the UAM process on the microstructure and hardness of weld interfaces and bulk material.

2.2.1 Experimental Methods

Sample Fabrication and Test Plan

In this study, all samples were manufactured using a Fabrisonic SonicLayer 4000 9 kW UAM system. Nine layers of 0.127 mm (0.005 in) thick, 25.4 mm (1 in) wide annealed SS 410 steel foils[2] were automatically fed and welded onto a 6.35 mm (0.5 in) thick ASTM A36 hot-rolled carbon steel baseplate.

Pilot welds were performed to identify viable weld parameters; those include normal force, vibration amplitude, weld speed, and baseplate preheat temperature. As is common practice in UAM work, weld parameters were considered viable when a welded foil could not be pulled off by hand. A baseplate temperature of 38°C (100°F) is the lowest temperature that a UAM SS 410 weld is formed successfully within the process window. A baseplate temperature of 204°C (400°F) is the recommended upper limit for commercial UAM machines. The process parameters and levels that are selected for building UAM samples in this study are listed in Table 2.6.

Table 2.6: Process parameters used for SS 410 weld.

Parameters	Level 1	Level 2
Normal force (N)	6000	6000
Vibration amplitude (μm)	31.08	31.08
Weld speed (m/s)	0.017	0.017
Baseplate temperature (°C)	38	204

[2]The welding width of the sonotrode is 20.3 mm (0.8 inch).

Four different treatment combinations were utilized as shown in Table 2.7. Mechanical shear testing utilizing the custom shear fixture introduced in Chapter 2.1 was conducted on all samples. SEM and EBSD analyses were also employed on samples that were welded at a baseplate temperature of 204°C (400°F) to be tested for both as-welded and HIP treatment conditions.

Table 2.7: Test plan.

Pre-heat Temperature	As-welded	HIP
38°C (100°F)	Shear	Shear
204°C (400°F)	Shear/SEM/EBSD	Shear/SEM/EBSD

HIP Processing

One UAM SS 410 build for each weld condition was treated under HIP. Typical HIP systems deliver up to 2000°C temperature and up to 207 MPa pressure [50]. The process parameters summarized in Table 2.8 were determined based on previous HIP studies on similar materials like carbon steel 4130 [42] and composite TiB-SS 316L [4]. After HIP treatment, the mechanical properties of the builds were examined by shear testing and the microstructural characteristics were investigated by SEM and EBSD analyses as outlined in Table 2.7.

Shear Testing

The shear test method introduced in Chapter 2.1 was used to characterize the mechanical strength of UAM steel builds in this study. As presented in Figure 2.9(a), a

Table 2.8: Process parameters selected for HIP UAM SS 410.

Hold Temperature	Hold Pressure	Hold Time	Atmosphere
1121°C	103.42 MPa	4 hours	Argon
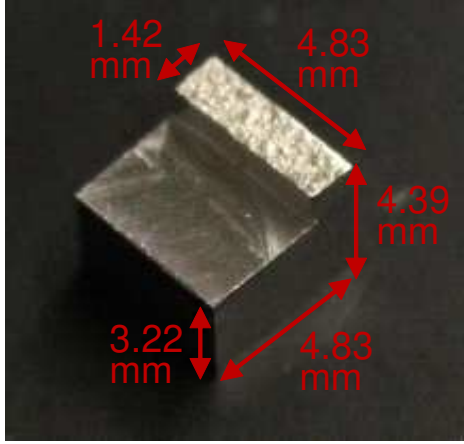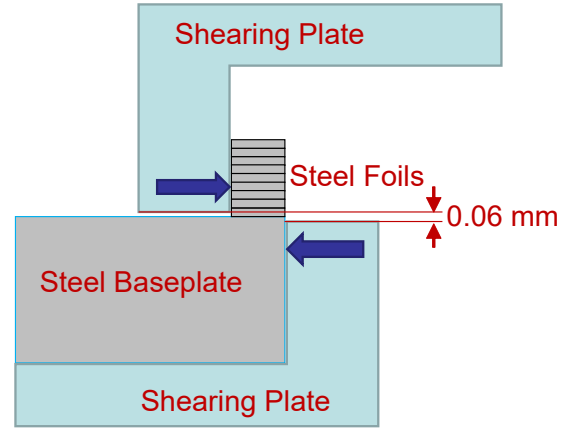
(a)   (b)

Figure 2.9: Shear test details including (a) image of stepped shear sample with nominal dimensions and (b) schematic of test loading condition.

stepped sample geometry has been employed in this study to ensure that the shear occurs at the interface between the baseplate and the first layer of foil. The stepped shear samples were loaded into the fixture and then tested on an MTS C43.504 50 kN load frame. A schematic of the loading condition is shown in Figure 2.9(b). The tests were conducted on three samples for each weld and treatment condition.

Microstructural Analyses

Microstructural analyses including optical imaging, SEM, EBSD, microindentation, and nanoindentation were performed to investigate the global and local changes in microstructure and hardness of UAM samples. In order to preserve the microstructures developed during the UAM and HIP process, samples were sectioned using a low-speed saw with coolant to minimize heating. Then, the samples were mounted in conductive bakelite and polished according to standard metallography preparation procedures. A final polish was performed using colloidal silica to remove the deformed layer on the surface of EBSD samples. Vilella's reagent was used to etch SEM and optical imaging samples. EBSD was performed using a JEOL 6500 machine equipped with an EBSD detector, SEM was performed using a Zeiss EVO MA15 at 20 kV, and optical imaging was performed using a Leica DM4000M to investigate the microstructure changes due to the UAM and HIP processes. Microindentation tests were carried out with a LECO LM100 to quantify global hardness properties of the UAM steel samples. Nanoindentation tests were performed with an Inforce 1000 machine to obtain local hardness properties across UAM interfaces.

2.2.2 Results

Shear Test Results

A summary of the shear test results for all four treatment conditions is provided in Table 2.9. Individual loading curves are presented in Figure 2.10. Three samples were intended to be tested for each condition. However, one as-welded sample for each baseplate temperature condition failed during machining. No loading curves were obtained for those two samples. As shown, for samples that were welded at a

baseplate temperature of 38°C, the shear strength of HIP treated samples is 337.80 MPa compared with a shear strength of 137.51 MPa for as-welded samples. Similarly, for samples that were welded at a baseplate temperature of 204°C, HIP treatment more than doubles the shear strength. The average shear strength of HIP/204°C samples is 344 MPa, which falls in the nominal shear strength range of annealed bulk SS 410 of 330 MPa to 470 MPa. These results suggest that the HIP process significantly increases the mechanical strength of the bonding interface.

The standard deviation of shear strength for each condition is also given to characterize the variation of the shear test results. For the 204°C condition, the HIP process reduces the standard deviation from 13.57 MPa to 2.28 MPa. However, the results of the 38°C condition do not show the same trend, which needs further investigation. It is observed that the three loading curves of the HIP/38°C condition are not consistent with each other, which suggests that the HIP treatment did not heal all of the interfacial defects and bring interfacial properties of all three samples to the same level.

Slight increases in the shear strength and decreases in the standard deviation are found for as-welded structures when baseplate temperature increases from 38°C to

Table 2.9: Average ultimate shear strength of UAM-made SS 410.

Baseplate Temperature	38°C		204°C	
Treatment	As-welded	HIP	As-welded	HIP
Shear Strength (MPa)	137.51	337.80	154.22	344.39
Standard Dev. (MPa)	21.99	64.43	13.57	2.28
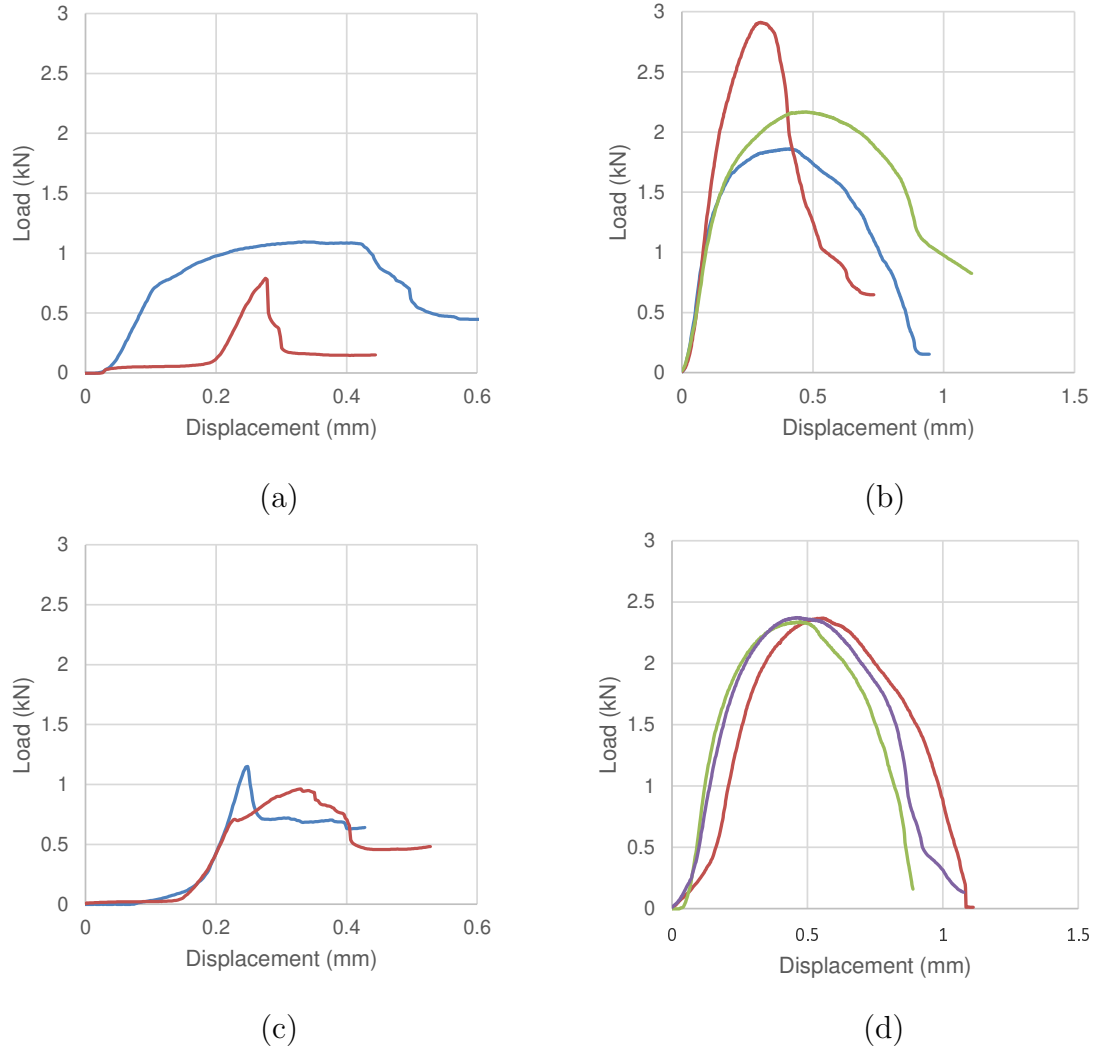
Figure 2.10: Shear test measurements for (a) as-welded/38°C, (b) HIP/38°C, (c) as-welded/204°C, and (d) HIP/204°C. The nominal shear resisting area is $6.85\,\text{mm}^2$.

204°C. In similar fashion, the HIP/204°C condition has a higher shear strength and much lower standard deviation compared to the HIP/38°C condition. These results indicate that the increase of the baseplate temperature increases the shear strength of the bonding interface and improves consistency of the weld quality.

<div align="center">(a)   (b)</div>
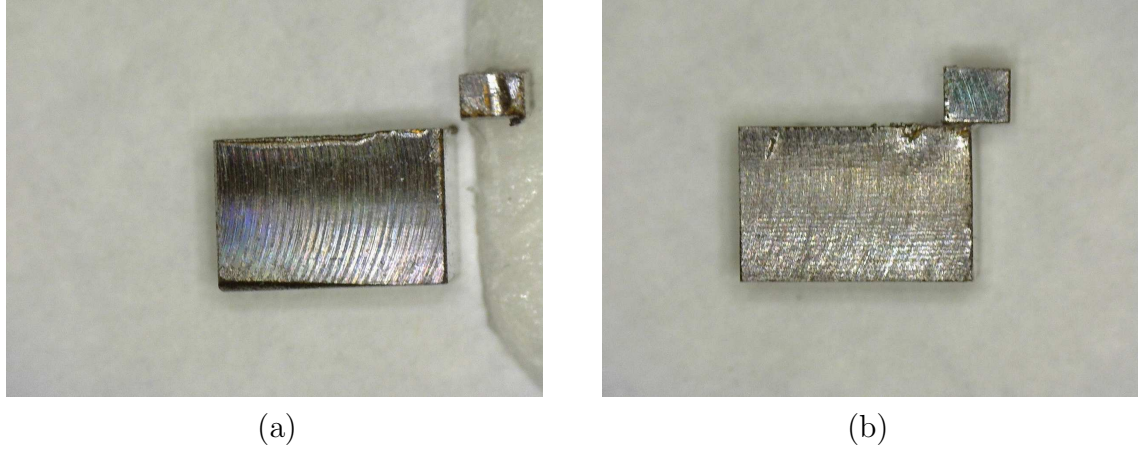
Figure 2.11: Post-shear images for (a) as-welded/204°C sample, and (b) HIP/204°C sample.

Images of typical post-shear test samples are provided in Figure 2.11. The as-welded/204°C sample broke into two separate parts and the foil part of the sample was sheared off after a short loading displacement, while the HIP treated samples exhibited a higher resistance to shear and a more ductile failure mode.

The fracture surfaces of the post-shear UAM samples were examined using SEM by collaborators from University of Tennessee (UTK). A manual point-count method [33] was used to quantify the fracture surface failure modes. Ten randomly located SEM images were taken for each treatment condition. Each SEM image was then evenly divided into 117 grids. Each grid was counted as one of four failure features including machined surface, brittle failure, ductile failure, and flow. The area fraction of each failure feature for different treatment conditions is calculated and showed in Table 2.10. The definition for each failure feature is listed below and representative fracture surface images for different treatment conditions are shown in Figure 2.12.

- Machined surface: smooth surface area with small dark dots following the machining direction. Indicates no metallurgical bonding

- Brittle failure: sheared-off region with straight/sharp fracture

- Ductile failure: metallurgical bonding area with typical circular cup/cone type fracture normal to the fracture surface

- Flow: texture area produced by indentation of asperities. Indicates no metallurgical bonding but may provide mechanical interlocking

Machined surface is the area where no bond was formed. Ductile failure represents the area where metallurgical bonding was formed during welding. Brittle failure and flow are the regions where mechanical interlocking is formed instead of metallurgical bonding. It is expected that mechanical interlocking is weaker than metallurgical bonding.

Table 2.10: Area fraction of the failure features presented on the fracture surface.

Failure feature	as-welded/38°C	HIP/38°C	as-welded/204°C	HIP/204°C
Brittle failure	21.7%	7.7%	19.6%	1.5%
Machined surface	36.6%	N/A	N/A	N/A
Flow	27.4%	6.2%	3.9%	2.7%
Ductile failure	14.3%	86.1%	76.5%	95.8%

As shown in Table 2.10, a machined surface is only found for the as-welded/38°C condition, which indicates a lack of plastic deformation at the welding interface. Compared with the as-welded/38°C sample, as-welded/204°C samples have larger ductile

areas, smaller brittle and flow areas, and no machined surface, which means that higher baseplate temperature promotes metallurgical bonding at the welding interface. In addition, post-HIP samples exhibit larger ductile failure areas compared to as-welded samples, which indicates that further bond improvement is achieved with HIP. The results are consistent with the shear test results shown in Figure 2.10. These fractured surface analyses, post-shear image examinations, and shear test results all suggest that a higher baseplate temperature and HIP treatment improve the mechanical strength and ductility of the UAM SS 410 weld interface.
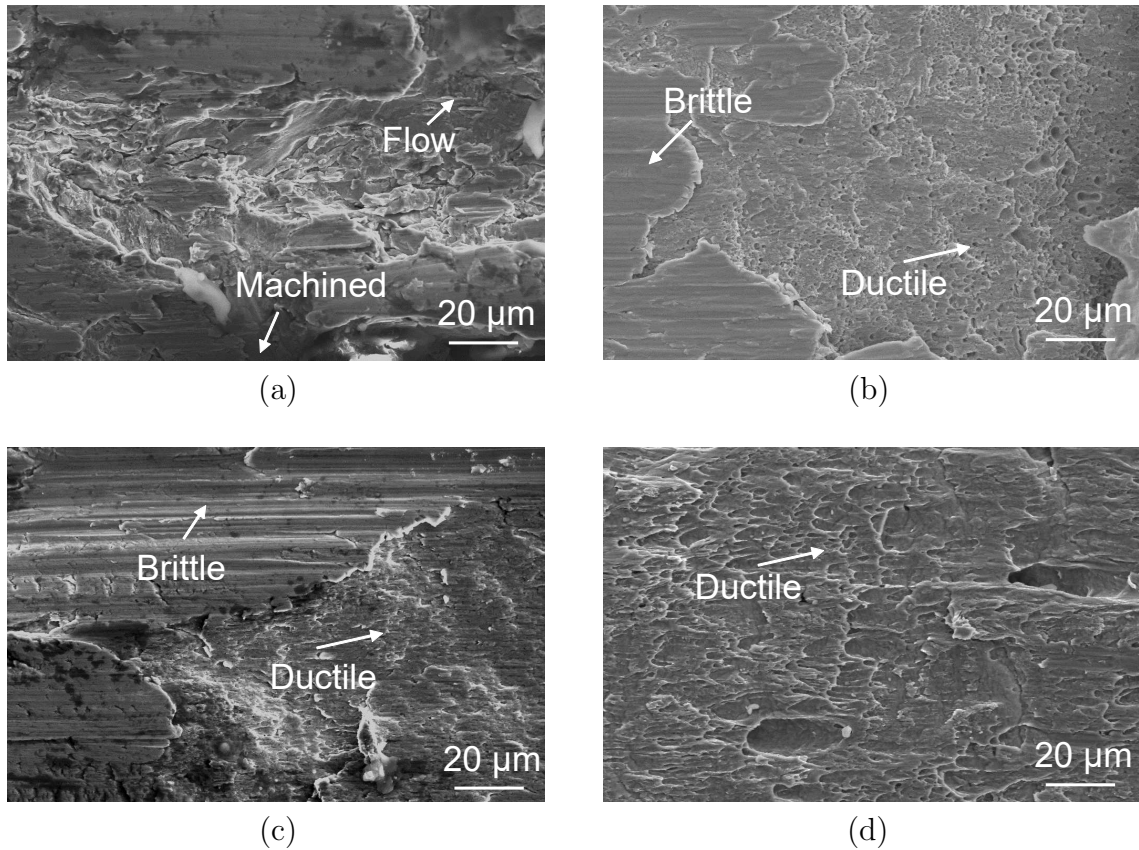
Figure 2.12: SEM of the post-shear fractured surface of samples (a) as-welded/38°C, (b) HIP/38°C, (c) as-welded/204°C, and (d) HIP/204°C.

Microstructural evaluations

UAM SS 410 samples that were prepared at a baseplate temperature of 204°C were analyzed with SEM and EBSD by collaborators from UTK. The back-scattered electrons (BSE) micrographs in Figure 2.13(a) and 2.13(c) show that the interface (marked with black arrows) of as-welded UAM SS 410 predominantly consists of ferrite grains. Figure 2.13(b) and 2.13(d) will be discussed in the next section. EBSD micrographs of bonded and unbonded areas at the same UAM interface are shown in Figure 2.14. The image quality mapping is shown in Figure 2.14(b), while the inverse pole figure (IPF) is overlaid with the image quality mapping in Figure 2.14(a) and 2.14(c). The coordinate system of the specimen is defined as the accumulating direction (AD), the vibrating direction (VD), and the rolling direction (RD) [57]. EBSD of the as-received 410 foil in Figure 2.14(d) shows an equiaxed grain structure. Both bonded and unbonded areas at the interface appear to have highly deformed grains after the UAM process.

The micro texture presented in Figure 2.15 shows the presence of a strong alpha fiber <110> ∥VD. Since no other variants, particularly Goss variants, are visible, the result suggests that the new grains do not occur from nucleation and growth, but evolve due to plasticity of the shear region [45]. As shown in Figure 2.16, a similar alpha texture <110> ∥VD is observed in the high strain rate deformed interstitial-free steel sample [45]. These similar texture patterns indicate that both the bonded and unbonded areas of the UAM interface may have experienced high strain rate deformation. The unbonded area is speculated to be a zone where excessive plastic deformation breaks the previously formed bonds.
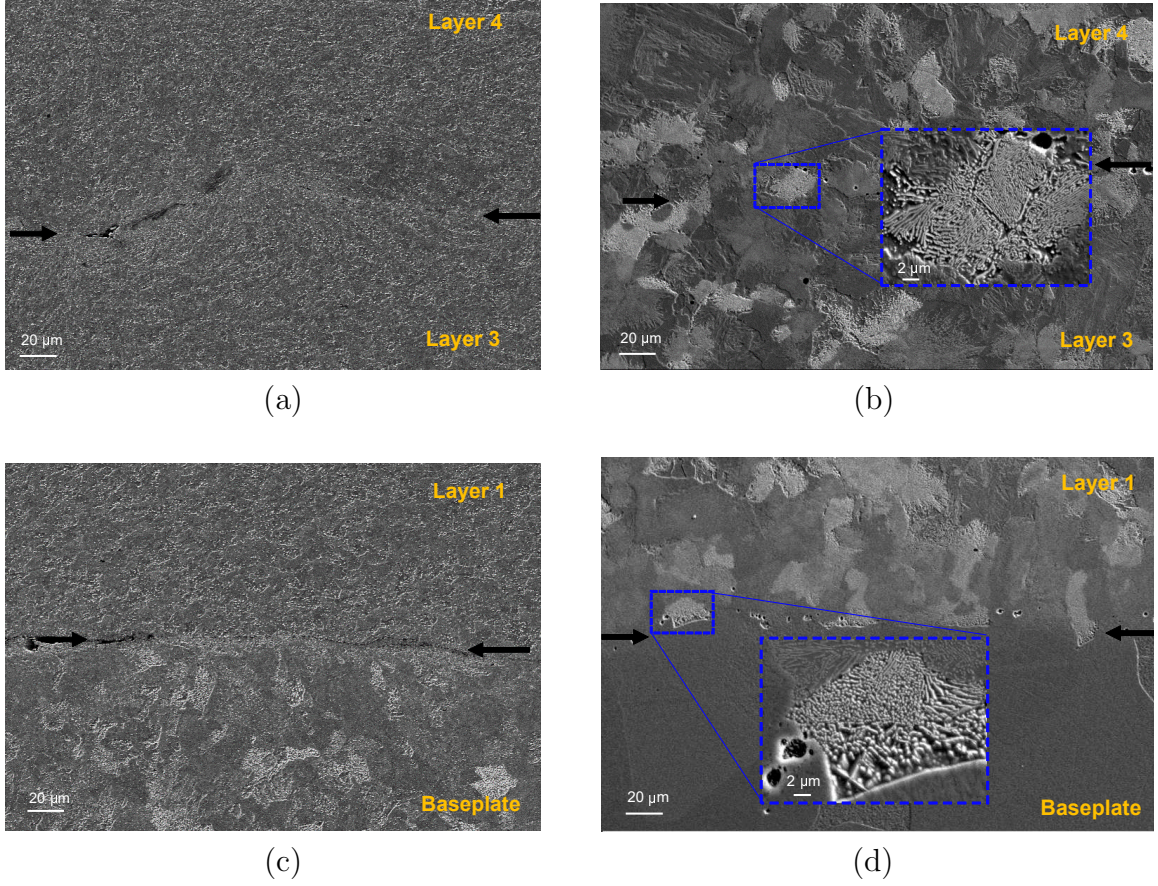
Figure 2.13: Back-scattered electron micrographs of the UAM interfaces: (a) as-welded interface between the 3rd layer and the 4th layers of foil, (b) post-HIP interface between the 3rd and the 4th layers of foil, (c) as-welded interface between the baseplate and the 1st layer of foil, and (d) post-HIP interface between the baseplate and the 1st layer of foil.

As discussed before, HIP increases the shear strength of UAM SS 410. To further investigate the influence of HIP on microstructure changes, samples that were prepared at a baseplate temperature of 204°C were analyzed with SEM and EBSD. In the previous study on UAM of carbon steel 4130 [42], the UAM interfaces consist predominantly of only ferrite and the authors assume that the presence of nonmetallic inclusions at the interface results in the nucleation of ferrite and prevents the
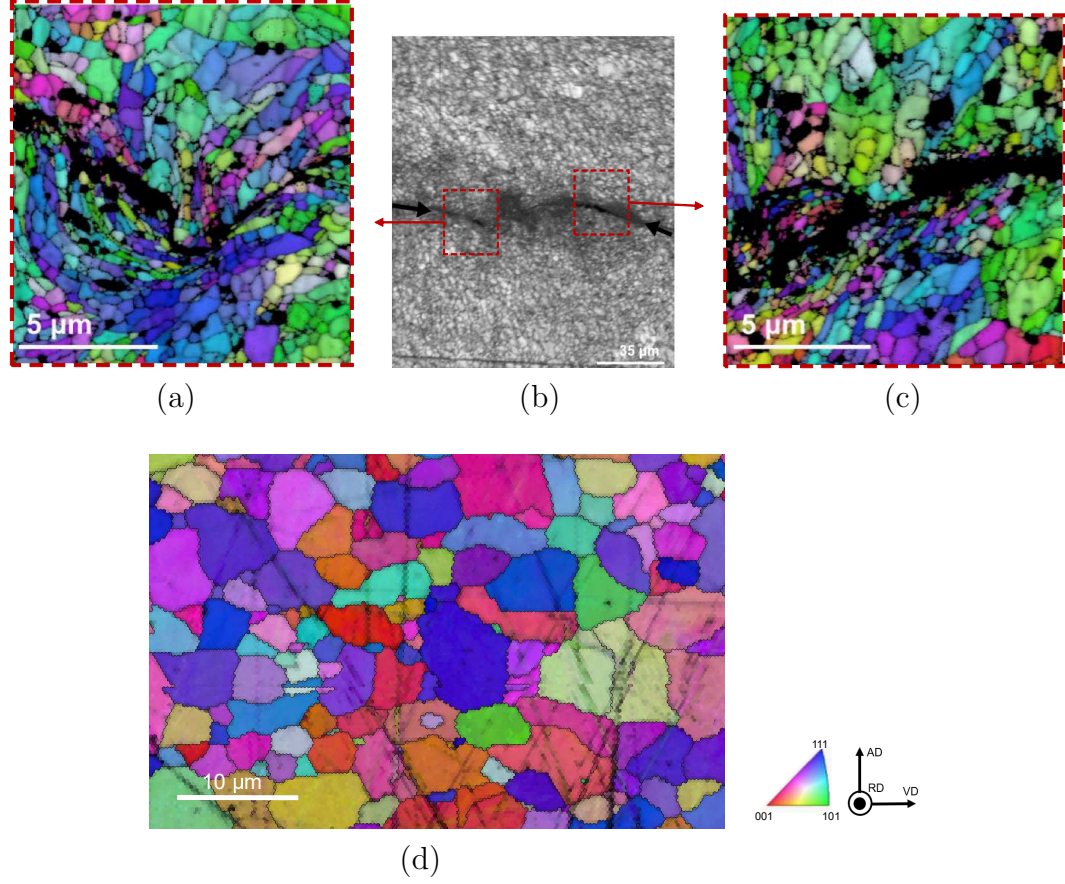
Figure 2.14: EBSD micrographs of (a) bonded area, (b) UAM interface, (c) unbonded area, and (d) as-received SS 410 foil. The bonded areas are distinguished from unbonded areas by using SEM micrographs which are not shown here. Note that small black dots in (a) and (c) are not resolved due to small grains or distorted grains. The black distorted regions in the center part of (a) are black due to the significant plastic deformation resulting in the formation of zones with low image quality, while the black zones in the center part of (c) are voids.

formation of pearlite. However, the interfaces of UAM SS 410 samples with HIP are composed of pearlite, as shown in Figure 2.13(b) and 2.13(d). Additionally, the significant grain growth at the interface indicates that the pinning due to the oxides is a concern for Al but not for steel [64]. Due to the long exposure time and the slow cooling rates used in this study, the foil-to-foil interface is predominantly composed
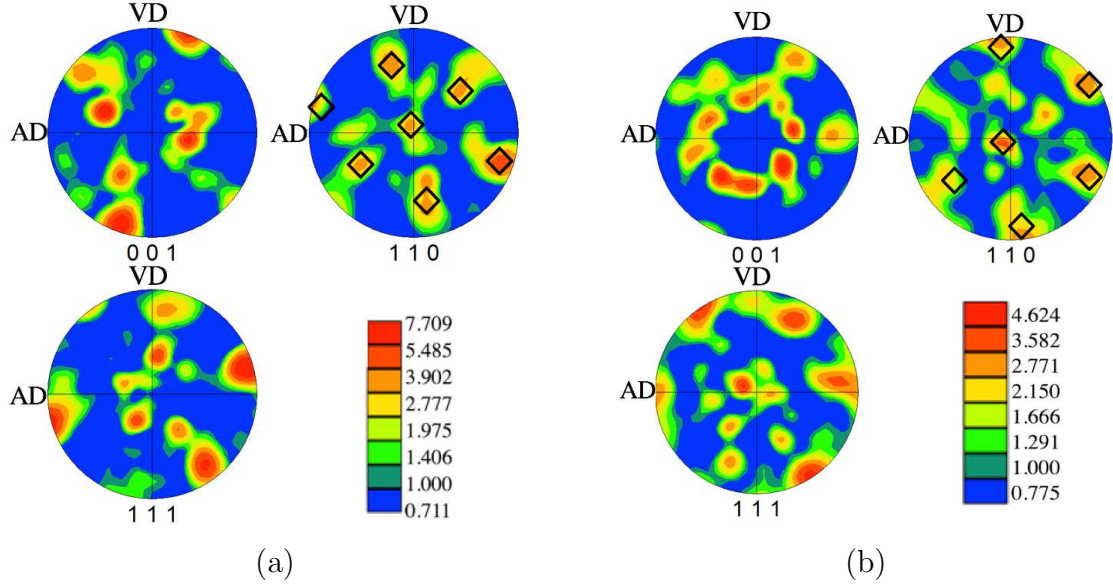
Figure 2.15: Pole figures show identical alpha fiber texture indicating that BCC to FCC transformation did not occur during the UAM process; (a) micro texture of the unbonded area, and (b) micro texture of the bonded area.

of pearlite as shown in Figure 2.13(b) with some local pockets of martensite, which is determined by plate-like grains as shown in Figure 2.17. The IPF is overlaid on the image quality mapping and the interface is marked with a yellow dotted line. The baseplate-to-foil interface is mostly composed of pearlite. Microhardness tests were conducted in a grid pattern spanning across the sample thickness for cross sections of as-welded and HIP samples. The results show that due to the formation of the martensite, the overall hardness of the samples increased from 204±7 HV in the as-welded condition to 240±16 HV in the UAM with HIP condition. The entire cross section did not transform to martensite primarily due to the slow cooling rates of 2 to 4 °C/min in the HIP process.
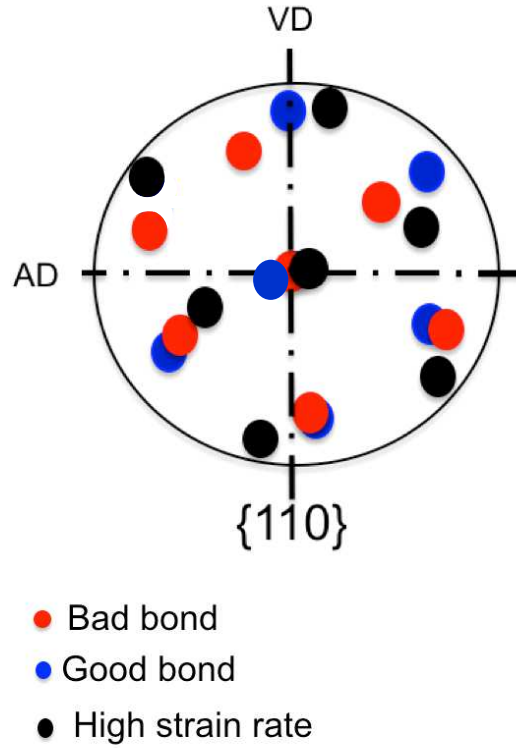
Figure 2.16: Comparisons of the micro texture of the UAM bonded area, UAM unbonded area and high strain rate deformed interstitial-free steel [45].

To further investigate the microstructure changes during the UAM process, nanoindentation tests were performed to characterize the local hardness across the interface. As shown in Figure 2.18, the top of layer n is harder than the bottom of layer n+1 for the as-welded UAM steel samples. The hardness of the top of layer n is increased because of severe plastic deformation which is due to the direct contact with the textured sonotrode. During the welding of layer n+1, the increased hardness in layer n is believed to limit the amount of plastic deformation and make it hard to

collapse asperities, which may contribute to the formation of voids at the welding interface. The nanoindentation results also indicate that hardening is more pronounced at the interface. Since detailed microstructure characterization shows no evidence of a martensitic transformation, the increase in hardness at the interface is primarily due to grain boundary strengthening as reported previously [65].

The effect of HIP on the interfacial hardness is also investigated. The hardness around the post-HIP foil-to-foil interface is about 3.68 GPa, while the hardness around the as-welded foil-to-foil interface is about 3.55 GPa. The load versus displacement curves of as-welded and post-HIP samples show a similar trend in that the top of layer n is harder than the bottom of layer n+1. It is worth mentioning that the increase in hardness above the interface of some post-HIP regions is likely due to the indentation
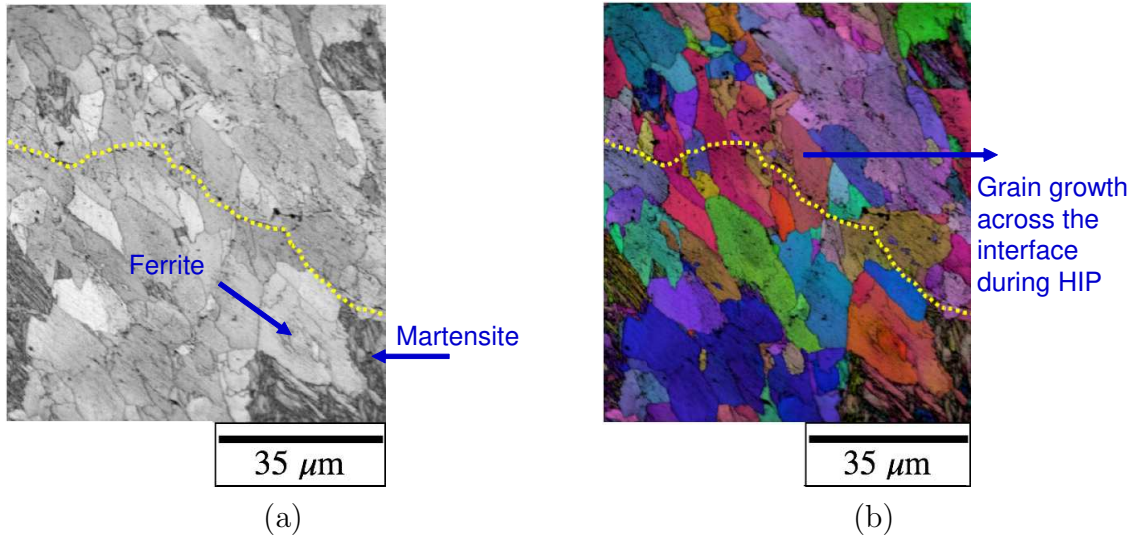
Figure 2.17: EBSD micrographs of the UAM interfaces after HIP show a grain boundary migration across the interface. The IPF shows the presence of ferrite and local islands of martensite after HIP treatment; (a) image quality mapping, (b) image quality mapping overlapped with IPF.
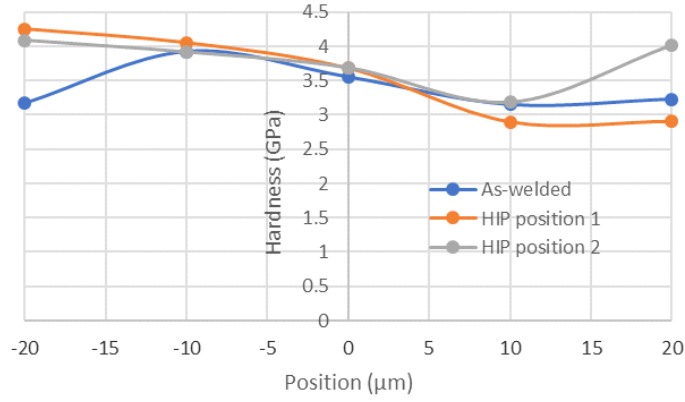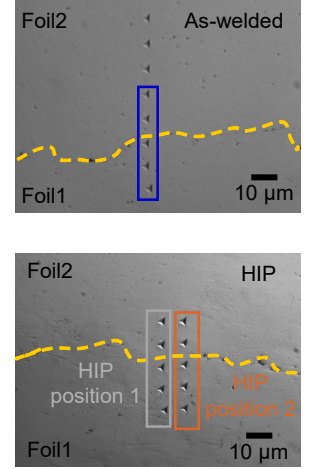
Figure 2.18: (a) Nanoindentation hardness maps across the foil-foil interface (at zero μm) of the as-welded and post-HIP UAM samples, (b) corresponding indentation positions.

of a pocket of martensite, such as those shown in Figure 2.17(a). The nanoindentation results of the selected regions are consistent with the microhardness results, which show that the post-HIP samples are harder than the as-welded samples.

2.2.3 Discussion

The present work shows that increasing the baseplate temperature improves the interfacial strength of UAM SS 410. One possible explanation is that the improvement is caused by a body centered cubic (BCC) ferrite to face centered cubic (FCC) austenite phase transformation during the UAM welding process. With higher baseplate temperatures and local temperature rise due to high strain rate deformation, the UAM interface temperature may exceed the critical temperature of BCC ferrite to FCC austenite phase transformation [32, 17, 45, 77, 72]. Since FCC austenite is relatively soft and easier to deform than BCC ferrite, this possible transformation may lead to

an improvement in bond quality. At a high enough cooling rate, as is the case in the UAM process [68], FCC austenite transforms into BCC martensitic grains. However, no martensitic phase is observed in the as-welded sample as shown in Figure 2.13(a) and 2.13(c). The texture analysis results in Figure 2.15 also indicate that the BCC ferrite to FCC austenite transformation did not occur, since no martensitic transformation texture was observed. It is therefore speculated that the improvement of UAM weld quality results from the reduction of yield strength with temperature. As shown in Figure 2.19, SS 410 has a lower yield strength at higher temperatures. Therefore, it becomes easier to deform asperities and to create metallurgical bonding of SS 410 at the interface. However, the amount of the reduction of yield strength is unknown, since the interfacial temperature rise during welding of UAM SS 410 has not been reported in previous research. A future study is planned to measure and quantify the interfacial temperature rise.

HIP further improves the shear strength of UAM SS 410 to be comparable to that of bulk 410 material. This improvement is attributed to the formation of a pearlite layer and the healing of interfacial defects at the interface between the A36 baseplate and the SS 410 foil. To form a fully pearlite layer, the amount of carbon at the interface has to exceed 0.76% (wt), while the starting amount of carbon in SS 410 foil is 0.14% (wt). It is hypothesized that this pearlite layer occurs as a result of carbon diffusion, which is driven by a carbon chemical potential difference. To evaluate the extent of carbon diffusion across the interface, DICTRA calculations have been performed by collaborators from UTK and the results are shown in Figure 2.20(a). A 3.22 mm thick A36 steel and a 0.150 mm thick SS 410 foil are simulated in this 1D model. The black line shows the starting carbon content across the interface between

51
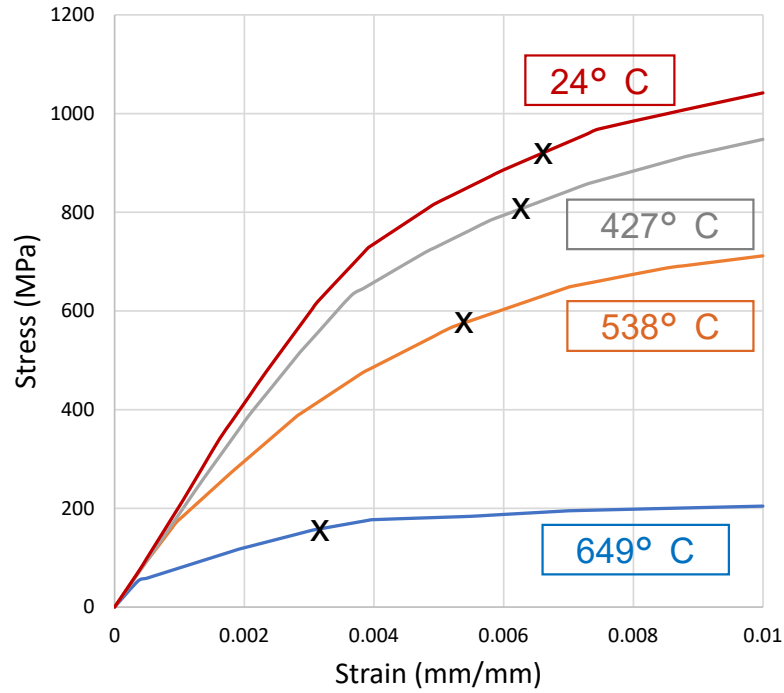
Figure 2.19: Plots are regenerated based on the ASM atlas of stress-strain curves [49]. These stress strain curves are for SS 410 (371°C temper), which has a different heat treatment than the SS 410 used in this study.

the A36 steel baseplate and SS 410, while the red line shows the ending carbon content. The interface position is marked with a blue dotted line. The results show that the carbon content of the A36 steel baseplate side reduces from 0.25% to 0.21% (wt). The amount of carbon in the SS 410 side of the interface increases from 0.14% to 0.51% (wt). This uphill diffusion of carbon is caused by the high Cr concentration of SS 410 [7, 81]. The calculated amount of carbon does not reach 0.76% (wt), but it is should be pointed out that the heating and cooling periods of the HIP process were not included in the simulation for simplicity. In this DICTRA simulation, only the 4-hour holding period of the HIP process is included in the model. To validate the DICTRA simulation, an optical micrograph of a UAM SS 410 sample with HIP was

analyzed using ImageJ software. As shown in Figure 2.20(b), dark areas are pearlite and light areas are ferrite. With the aid of ImageJ, the area fraction of pearlite is calculated as 29.3% of the region highlighted with blue lines compared with an area fraction of 42.0% of the region highlighted with red lines. This shows a similar trend as the carbon content predicted by DICTRA.
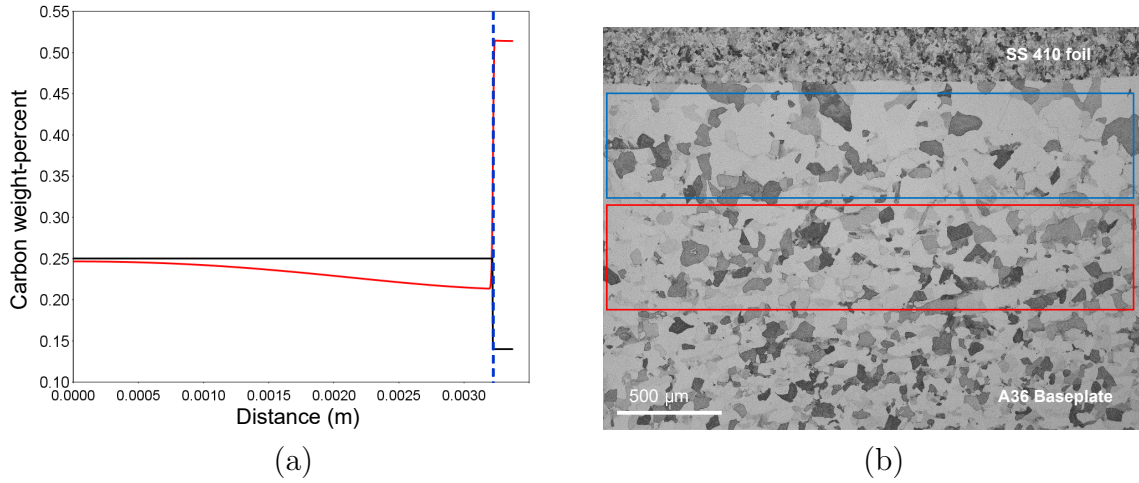
Figure 2.20: (a) DICTRA simulation results: the black line represents the starting carbon content across the interface between the A36 steel baseplate and the SS 410, while the red line shows the ending carbon content. The blue dotted line represents the original interface. The left side is A36 baseplate and the right side is SS 410. (b) Optical image of the corresponding interface between the A36 baseplate and the SS 410 foil: dark areas are pearlite and light areas are ferrite. Area fraction of pearlite of two highlighted areas is calculated using ImageJ. Each highlighted area is 500 μm x 2519 μm.

2.2.4 Summary

Stainless steel 410 builds were fabricated using UAM. The shear strength properties of UAM SS 410 with HIP are comparable with those of bulk material. The study shows that increasing the baseplate temperature from 38°C to 204°C improves weld

quality. HIP treatment improves the shear strength of UAM SS 410 samples by a factor of 2 as compared to as-welded UAM SS 410 samples. Post-shear fracture surface examinations reveal that as-welded/204°C samples have larger ductile failure areas than as-welded/38°C samples, which indicates that higher baseplate temperature promotes metallurgical bonding. Similarly, post-HIP samples have larger ductile failure areas than as-welded samples, which means that HIP further promotes metallurgical bonding. These analyses are consistent with shear test results. Further microstructural analyses of as-welded samples with SEM and EBSD show no evidence of BCC to FCC transformation taking place during the UAM process. The reduction of the yield strength of SS 410 at elevated temperature is believed to be the cause of weld quality improvement at higher baseplate temperature. A pearlite layer is found between the A36 baseplate and the first layer of SS 410 foil after HIP treatment. DICTRA simulations show that the pearlite layer occurs as a result of uphill carbon diffusion at the interface. HIP treatment is shown to increase the overall hardness of UAM SS 410 from 204 ± 7 HV to 240 ± 16 HV due to the formation of local pockets of martensite. Nanohardness tests show that the top of layer n is harder than the bottom of layer n+1. The increase in hardness at the interface is primarily due to grain boundary strengthening.

2.3 Effect of Weld Power and Interfacial Temperature on the Microstructure and Mechanical Properties of UAM 4130

As indicated in the previous study, increased baseplate temperature has been shown to improve the UAM steel weld quality. However, a baseplate temperature at the

current 204 °C equipment limit is not sufficient to achieve a weld with shear strength comparable to that of bulk steel. Therefore, post heat treatment methods such as hot isostatic pressing (HIP) have been applied to further improve the weld strength. Considering the extra cost and time associated with HIP, methods to avoid HIP and achieve UAM welds with sufficient strength are desired.

The premise of this study is that increasing weld power improves the shear strength of as-welded UAM 4130 steel. A cobalt-based hard-facing alloy (Stellite) coated sonotrode [62, 61] is used to increase the galling threshold and allow a higher power input. Previous research [60] has shown that cobalt-based alloys can effectively suppress galling by preventing strain localization at the contact surface. The high galling resistance of cobalt is attributed to its high strain hardening ability, which allows significant plastic deformation to be imposed on the steel foils.

Since the mechanical power during plastic deformation can be divided into stored strain energy that is spent on actual deformation and heat that is dissipated to the surroundings by a constant fraction for a certain metal, both the strain energy and heat increase as the power input increases [52, 36]. As the thermal conductivity of the coated sonotrode is only half that of the uncoated sonotrode, the heat loss through the sonotrode during welding should be lower. With higher heat inputs and lower heat losses, a higher interfacial temperature is anticipated. As the interfacial temperature increases, the yield strength of 4130 steel will decrease [19]. It becomes easier to plastically deform asperities and form metallurgical bonding at the welding interface. Therefore, with increased plastic work and decreased yield strength at the welding interface during welding, the resulting weld strength of UAM 4130 is expected to increase.

55

2.3.1 Experimental Methods

In this study, all UAM samples were manufactured using a 9 kW Fabrisonic Soni-cLayer 4000 UAM system. Two control specimens were fabricated using an uncoated tool steel (18Ni grade 350) sonotrode (UCS), while another specimen was made using a cobalt-chromium coated tool steel sonotrode (CS). Each sample was made from nine layers of 0.127 mm (0.005 in) thick, 25.4 mm (1 in) wide annealed 4130 steel foils and low carbon steel baseplates (ASTM A36 or AISI 4130). The welding parameters are summarized in Table 2.11. The HIP process was conducted on a control sample made with an uncoated steel sonotrode (UCS-HIP). The HIP treatment was carried out with a temperature of 1000 °C, an argon pressure of 200 MPa, and a duration of 4 hours.

Table 2.11: Process parameters used to weld UAM 4130.

Parameters	UCS/UCS-HIP	CS
Normal force (N)	6500	6500
Vibration amplitude (μm)	32.4	38.8
Weld speed (mm/s)	17	21
Baseplate temperature (°C)	204	204
Sonotrode	uncoated	coated

An OMEGA Type K AWG 40 thermocouple (0.080 mm tip diameter) was used to measure the temperature at the interface of the baseplate and the first foil. A thermocouple amplifier SEN30101 produced by Playing With Fusion, Inc. was used to

amplify the voltage signal generated by the thermocouple. Temperature data was collected at 50 kHz. The experimental setup is shown in Figure 2.21(a). A thermocouple was placed through a 1.5 mm hole in the baseplate and the tip was bent onto the top surface. Temperature was measured while the first layer of foil was welded onto the baseplate using the coated sonotrode. To help understand the effect of temperature on microstructural changes, the continuous cooling transformation (CCT) diagram, equilibrium lower critical temperature (Ac1), and upper critical temperature (Ac3) were calculated using JMatPro.

A customized shear test method was used to characterize the mechanical strength of the baseplate and first foil interface of UAM builds. Five shear test samples for UCS and UCS-HIP and three shear test samples for CS treatment conditions were cut out from specimens, prepared following the procedure described in Chapter 2.2, and then tested on an MTS C43.504 50 kN load frame. In addition to mechanical testing, microstructural analyses were performed with scanning electron microscopy (SEM). The UAM sample that was made with the coated sonotrode was prepared according to standard metallographic procedures and then etched with 2% Nital. A micrograph of the weld interface was taken on a JEOL 6500 FEG SEM with an accelerating voltage of 10 keV and a working distance of 8 mm. Post-shear micrographs of the fracture surface were taken on a Zeiss EVO MA15 SEM with an accelerating voltage of 20 keV and a working distance of 8 mm.

2.3.2   Results and Discussion

The interfacial temperature profile was measured during welding of the first foil layer onto the baseplate. The total weld length is 76.2 mm and the thermocouple was

Top view of experiment setup

Side view of experiment setup

(a)

(b)

(c)
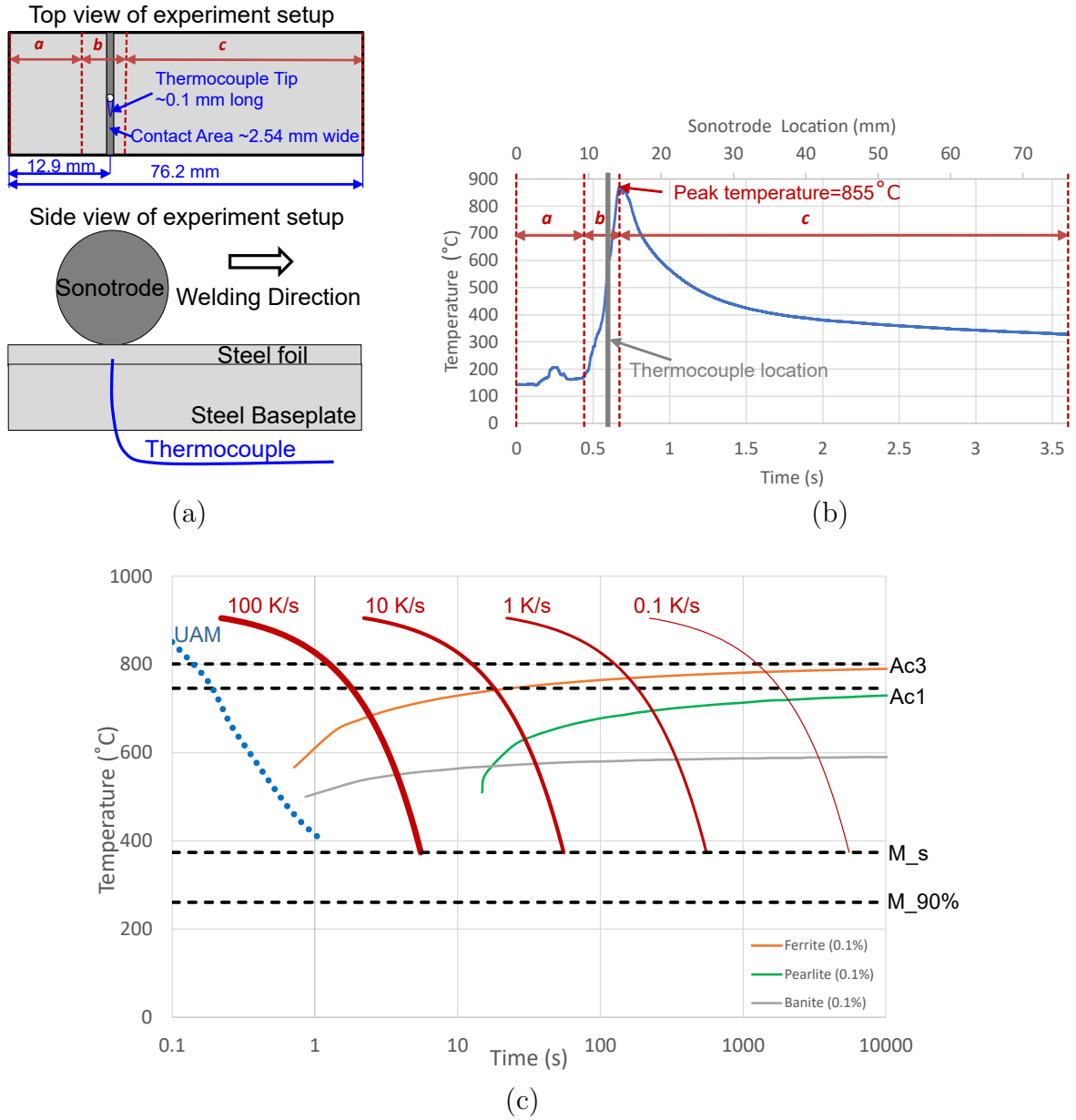
Figure 2.21: (a) Temperature measurement setup showing the embedded thermocouple, (b) interfacial temperature measurement profile while the first layer of steel foil was welded onto the baseplate using the coated sonotrode, and (c) continuous cooling transformation (CCT) diagram of 4130 steel including the UAM cooling rate for comparison.

placed 12.9 mm away from the starting point. The contact area width of the sonotrode pressing on the foil is estimated to be about 2.54 mm based on empirical evidence [30]. During time period $\boldsymbol{a}$ (0 s to 0.44 s), as shown in Figure 2.21(b), the coated sonotrode pressed the foil against the baseplate, started to weld, and approached the thermocouple location. A slight drop of the temperature from the preset point of about 200 °C was recorded as the cooler foil (at room temperature) absorbed heat from the baseplate. Then, when the sonotrode reached a location that is about 3.6 mm before the thermocouple and formed a weld, temperature began to rise. The peak temperature was reached at the end of period $\boldsymbol{b}$ (0.44 s to 0.67 s), when the sonotrode had moved across the thermocouple and the trailing edge of the sonotrode-foil contact patch reached the thermocouple. The sharp increase in temperature is believed to be caused by the frictional heat and plastic deformation during welding [70]. During time period $\boldsymbol{c}$ (0.67 s to 3.6 s), when the sonotrode moved further away from the thermocouple location after the weld, the weld area cooled down through conductive and convective heat loss. According to the measurement, the peak interfacial temperature is 855 °C[3] for this CS sample, while the typical peak temperature range for welding different UCS samples is from 522 °C to 563 °C. Since the peak interfacial temperature for the CS sample is above the 4130 steel equilibrium Ac3 of 801 °C, a body centered cubic (BCC) ferrite to face centered cubic (FCC) austenite phase transformation is expected. As shown in the CCT diagram in Figure 2.21(c), if the cooling rate is higher than 100 °C/s, as is the case during the UAM process (about 900 °C/s for the first 0.5 s), an austenite to martensite phase

---

[3]With nonlinearity correction applied per the thermocouple amplifier's manufacturer specification.

transformation is expected to occur. We thus search for evidence of BCC martensite in the UAM 4130 that is made using the coated sonotrode.
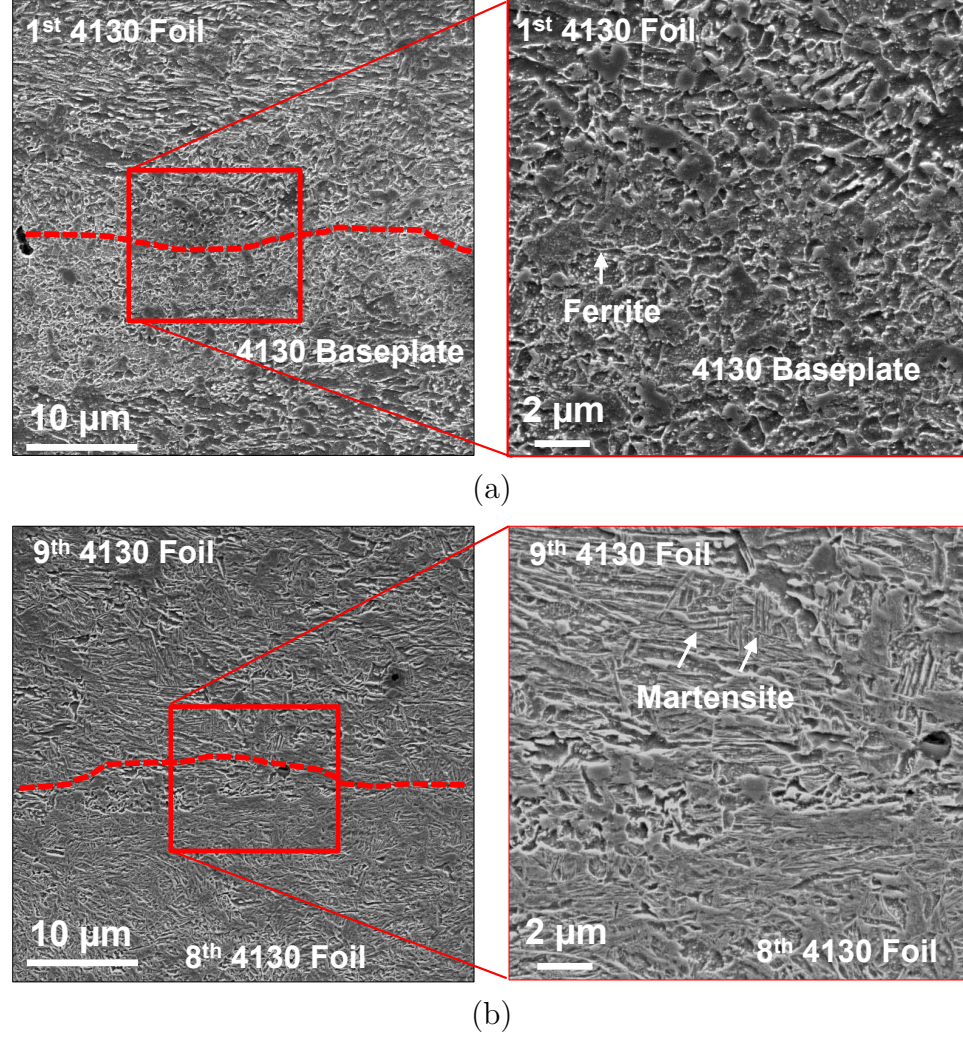
Figure 2.22:   Representative SEM images of (a) UAM interface region between the baseplate and first layer of foil and (b) UAM interface region between the eighth and ninth layer of foil. As shown in the inserts on the right, only carbides and ferrite are found for interface region in (a) and martensite is found for the interface region in (b). It should be recognized that the interface location is determined from the contrast of surrounding area at lower magnification (not shown). The approximate interface location is marked with red dotted line in the images.

However, as shown in Figure 2.22(a), an SEM image of the interface between the baseplate and first foil, where the temperature is measured, shows only carbides and ferrite at $1 \, \mu m$ scale. The fact that the microstructure of the interface is not fully martensitic could be explained by the increase of Ac1 and Ac3 due to the high heating rate. As reported in a study by Lolla et al. [46], the rapid heating rate ($>400 \, °C/s$) during flash processing of AISI 8620 steel increases Ac1 from $702 \, °C$ to $930 \, °C$ and Ac3 from $806 \, °C$ to $1050 \, °C$. Since the UAM process has a similar heating rate, ferrite and carbides are expected at the interface. Due to the limited spatial resolution of SEM, a submicron size martensitic structure could not be observed. It is noted that martensite is found at the interface between the eighth and ninth layers of foil as shown in Figure 2.22(b). This phenomenon may be caused by the high temperature that the sonotrode reaches after continuous welding and heating.

As summarized in Table 2.12, the average power input per unit area is $2695 \, W/m^2$ for CS samples compared with $2066 \, W/m^2$ for UCS samples. The average shear strength of CS samples is $549 \, MPa$, while the shear strength is $186 \, MPa$ for UCS samples and $456 \, MPa$ for UCS-HIP samples. Both CS and UCS-HIP samples give an average shear strength comparable to that of bulk 4130 steel. The average shear strength of CS samples is 195% greater than that of UCS samples and 20% greater than that of UCS-HIP samples. The standard deviation of the CS builds is between that of UCS and UCS-HIP builds. Compared to HIP, fabrication using the coated sonotrode offers the advantage of avoiding an extra post-processing step. The variations in CS shear samples cut from the same CS specimen may be caused by non-uniform heat input. Improvement of local welding variation may be achieved by optimizing the heating and cooling rate during the welding process. It is proposed

61

that the higher strength of CS samples fabricated with a higher power input is attributed to increased plastic deformation, which is caused by the reduction of the yield strength of 4130 at elevated process temperatures (still below melting temperature) and the increase of shear strain at the interface.

Table 2.12: Average ultimate shear strength of UAM 4130 steel.

Condition	UCS 4130	UCS-HIP 4130	CS 4130	Bulk 4130
Shear strength (MPa)	186	456	549	340~640 [1]
Standard dev. (MPa)	61	10	26	N/A
Sonotrode	uncoated	uncoated	coated	N/A
Average power per unit area[4] (W/m^2)	2066	2066	2695	N/A

To characterize the fracture surface failure types, a point count method [26] was used. Ten randomly located SEM images were taken for each condition and each SEM image was then evenly divided into 117 grids. Each grid was attributed as one of four failure features including machined surface, flow, brittle failure, and ductile failure based on surface morphology. The area fraction of each failure feature for different treatment conditions is presented in Table 2.13. The definition for each failure feature is defined in Chapter 2.2. Generally, a larger ductile area fraction indicates a better weld. As expected, compared with UCS samples, CS 4130 samples have much larger ductile areas and smaller brittle, flow, and machined areas, which indicates that stronger metallurgical bonding is achieved. Compared with UCS-HIP

[4]The average power per unit area is calculated by dividing the total energy input by the product of the welding time and the welding area.
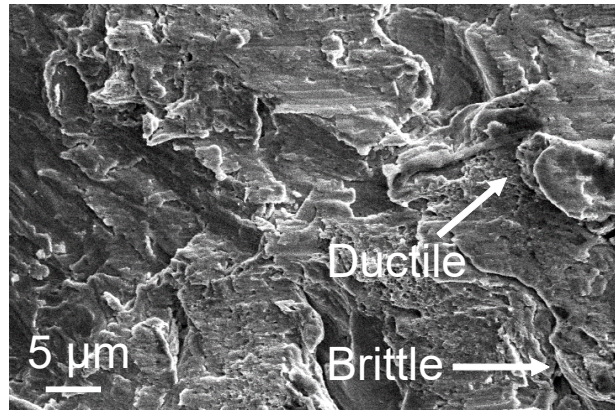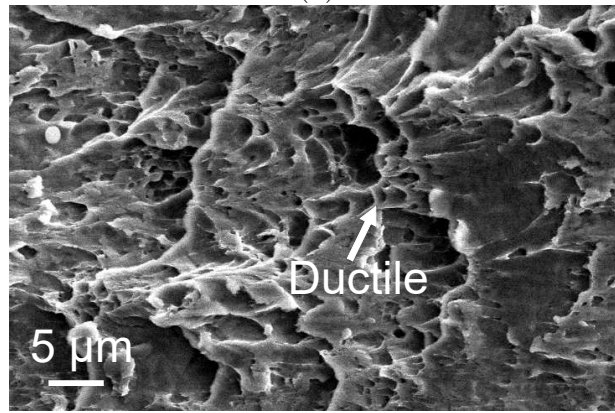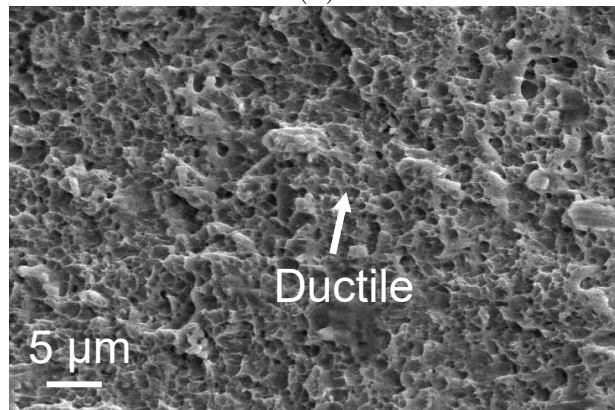
Figure 2.23: SEM images of the post-shear fractured surface of samples (a) UCS 4130, (b) UCS-HIP 4130, and (c) CS 4130.

samples, CS 4130 samples have slightly smaller ductile areas and larger brittle and machined areas, which explains the variation between the shear samples. The results are consistent with the shear test results.

Table 2.13: Area fraction of the failure features presented on the fracture surface.

Failure feature	UCS 4130	UCS-HIP 4130	CS 4130
Brittle failure	36.7%	1.5%	17.8%
Machined surface	28.3%	7.6%	16.3%
Flow	31.2%	26.4%	7.2%
Ductile failure	3.8%	64.5%	58.7%

Overall these results demonstrate that increasing weld power improves the shear strength of as-welded UAM 4130. However, similar to ultrasonic metal welding [41, 83], an upper weld power threshold is expected for UAM, beyond which the weld strength decreases as the weld power increases. Several factors may contribute to this weld strength decrease. First, excessive plastic deformation at the weld interface may lead to increased void density and decreased strength [41]. Second, interfacial temperature increases as weld power increases. Beyond a certain weld power, residual stress formed due to thermal expansion and contraction of material during welding may exceed the yield strength of the material and cause localized delamination. Third, fatigue due to cyclic shear force at the weld interface, which is produced by the ultrasonic vibrations, is expected to become significant at high weld power and may cause cracking or delamination. Investigating these factors in detail and identifying upper power thresholds for each will be the focus of future work.

64

2.3.3 Summary

In this study, the effect of increased weld power on the mechanical strength of as-welded UAM steel has been investigated. Applying 2695 W/m^2 with a cobalt-chromium coated sonotrode achieves an average shear strength of 549 MPa, which is comparable to that of bulk 4130 material. This represents a 195% improvement over the shear strength of 186 MPa for samples fabricated using 2066 W/m^2 with an uncoated steel sonotrode without post-processing and a 20% improvement over the shear strength of 456 MPa for HIP-treated samples. A point count analysis method with SEM was used to quantify post shear fracture surface features and the measurements are consistent with the shear test results. An in situ thermocouple temperature measurement method was used to monitor the interfacial temperature changes and a peak temperature of 855 °C was recorded, which indicates significant softening of the 4130 steel. This softening and increased plastic deformation caused by higher power input lead to the weld quality improvement of UAM 4130. Even though the peak interfacial temperature is beyond the upper critical temperature (Ac3) of 801 °C for 4130 steel, a fully martensitic structure is not observed at the interface between the baseplate and the first layer of foil. This is attributed to an increase in lower critical temperature (Ac1) and upper critical temperature (Ac3) due to the high heating rate (>400 °C/s) during UAM welding of steels.

Chapter 3

Design of Experiments Determination of Optimum Parameters for UAM Steel 4130

Overview

This chapter examines the effect of weld parameters on the weld quality of UAM steel. A design of experiments study based on a Taguchi L16 design array was conducted to investigate the influence of parameters including baseplate temperature, amplitude, welding speed, and normal force on the interfacial temperature and shear strength of UAM welding of carbon steel 4130. Analysis of variance (ANOVA) and main effects analysis were performed to determine optimal weld parameters within the current process window. A Pearson correlation test was conducted to find the relationship between interfacial temperature and shear strength. Optimal parameters, which generate the highest shear strength over the range tested, were also obtained.

3.1 Experimental Methods

3.1.1 Sample Fabrication

The materials used in this study are 0.127 mm (0.005 in) thick, 25.4 mm (1.0 in) wide annealed AISI 4130 steel foils and low carbon ASTM A36 steel baseplates. AISI 4130 steel was selected because of its heat treatability and frequent use in industry. All UAM samples were manufactured using a 9 kW Fabrisonic SonicLayer 4000 UAM system with a cobalt-chromium coated tool steel sonotrode.Three shear test samples were prepared for each treatment condition. Each shear test sample was made from twelve layers of annealed 4130 steel foil and an A36 steel baseplate, while each temperature measurement sample was made from three layers of annealed 4130 steel foil and an A36 baseplate.
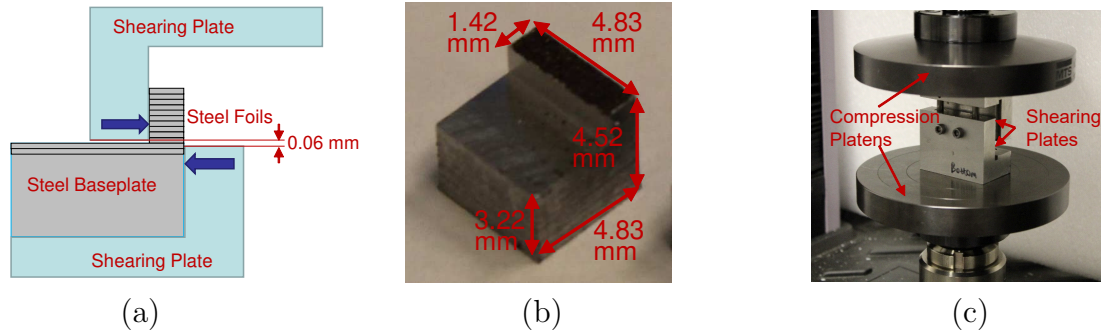
Figure 3.1: Shear test design includes (a) conceptual schematic of shear test loading condition, (b) image of shear test sample with nominal dimensions, and (c) image of experimental setup of the shear test with loaded sample on load frame.

The weld parameters for this DOE study follow a Taguchi L16 matrix design with four parameters: normal force, vibration amplitude, baseplate temperature, and welding speed. The Taguchi L16 matrix design is an economic design method that

67

Table 3.1: Taguchi L16 design array used for DOE where 1 indicates the lowest and 4 indicates the highest level for each parameter.

Parameter set (PS)	Baseplate temperature	Amplitude	Welding speed	Normal force
PS1	1	1	1	1
PS2	1	2	2	2
PS3	1	3	3	3
PS4	1	4	4	4
PS5	2	1	2	3
PS6	2	2	1	4
PS7	2	3	4	1
PS8	2	4	3	2
PS9	3	1	3	4
PS10	3	2	4	3
PS11	3	3	1	2
PS12	3	4	2	1
PS13	4	1	4	2
PS14	4	2	3	1
PS15	4	3	2	4
PS16	4	4	1	3

reduces the total number of treatment combinations from 256 to 16 for a design including four parameters at four levels each. The matrix design is presented in Table 3.1, where 1 indicates the lowest level and 4 indicates the highest level for each parameter. The exact value for each level of each parameter was determined from a pilot study. The lower limit of weld parameters is the value below which the welds could not be achieved, and the upper limit of weld parameters is the value above

which the top of the steel foil becomes welded to the sonotrode instead of the layer of steel foil below it. The values selected for each parameter and level are showed in Table 3.2.

Table 3.2: Weld parameter values for each DOE level.

Parameter	Level 1	Level 2	Level 3	Level 4
Baseplate temperature	100 °F (37.8 °C)	200 °F (93.3 °C)	300 °F (148.9 °C)	400 °F (204.4 °C)
Amplitude	27.1 μm	28.57 μm	30.03 μm	31.5 μm
Welding speed	40 in/min (16.93 mm/s)	60 in/min (25.40 mm/s)	80 in/min (33.87 mm/s)	100 in/min (42.33 mm/s)
Normal force	4000 N	5000 N	6000 N	7000 N

Pilot studies showed that 4130 steel foils would not weld to the A36 baseplate using certain sets of weld parameters. Consequently, all first layers were welded using the same set of parameters (Table 3.3) to provide a consistent base for the foil-to-foil welds being investigated. All of the subsequent foil layers were welded using the DOE study parameters presented in Table 3.2. The shear test is designed to shear the interface between the second and third layers of steel foil and the temperature is measured at the same interface during welding.

3.1.2 Temperature Measurements

OMEGA Type K AWG 40 thermocouple (0.080 mm tip diameter) was used to measure the temperature at the interface between the second and third layers of steel foil during welding. Before measurement, a 1.5 mm hole was drilled through the

Table 3.3: Weld parameter used for welding first layer.

Parameter	Level
Baseplate temperature	400 °F (204.4 °C)
Amplitude	28.57 μm
Welding speed	80 in/min (33.87 mm/s)
Normal force	5000 N

baseplate. Next, two layers of steel foil were welded onto the baseplate and a 1.5 mm hole was pierced through the foils at the location of the original hole. Finally, a thermocouple was placed through the hole and bent on the top surface of the foil. A schematic of the experimental setup is shown in Figure 3.2. Images of a typical thermocouple embedding process are shown in Figure 3.3. Interfacial temperature was measured at 10 kHz while the third layer of foil was welded onto the preceding foil layer. Temperature was measured twice for each treatment.

3.1.3 Mechanical Testing

A custom shear test method was used to characterize the mechanical strength of the interface between the second and third layers of UAM steel builds. This interface is selected to represent the foil-foil welding strength. The interface between the first and second layers is too close to the baseplate and not selected to prevent any undesired failure at the baseplate-foil interface. A stepped sample geometry is used in this study to ensure that shearing occurs at the desired interface. The sample geometry and loading conditions are shown in Figure 3.1(a) and 3.1(b). The shear test was performed on an MTS C43.504 50 kN load frame and fixed between two compression
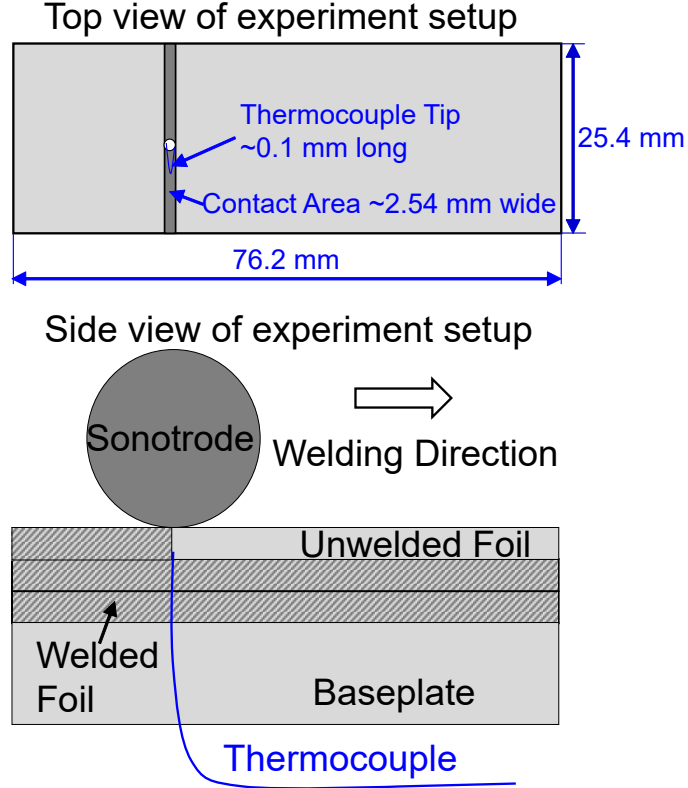
Figure 3.2: Schematic of temperature measurement setup with the embedded thermocouple.

platens as shown in Figure 3.1(c). The tests are conducted using displacement control with a loading speed of 0.02 mm/s.

3.1.4 Statistical Procedure

The statistic model used in this study was a generalized linear model (GLM) with four main effects. The linear model is given by

$$Y_{ijklt} = \mu + \alpha_i + \beta_j + \gamma_k + \delta_l + \epsilon_{ijklt}. \tag{3.1}$$

Before welding
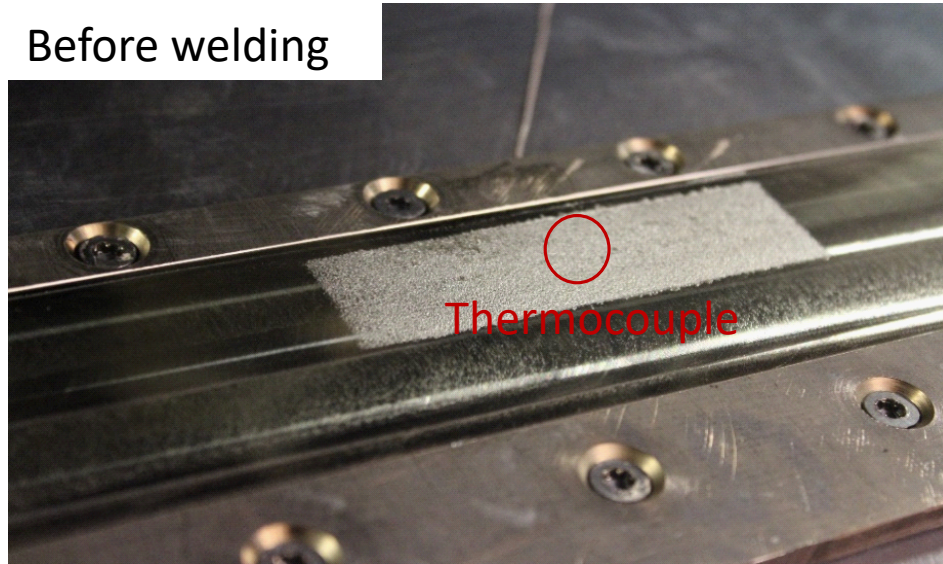
Thermocouple

(a)
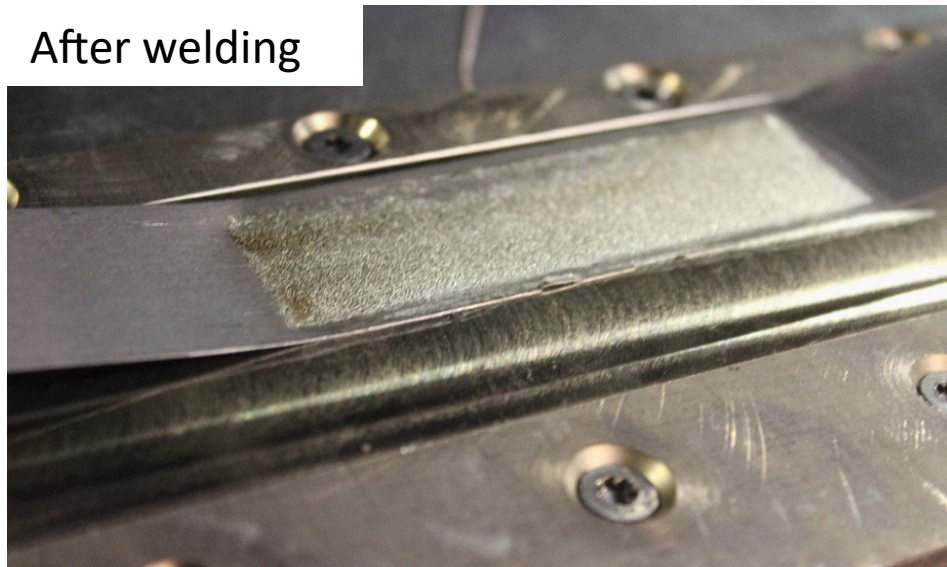
After welding

(b)

Figure 3.3: Images showing a typical thermocouple embedding process (a) before welding and (b) after welding.

This equation describes the dependence of the response variable (shear strength or interfacial temperature), Y_{ijklt}, on the levels of the treatment factors. In this equation, μ is the overall mean of the response variable (shear strength or interfacial temperature). The effects of the weld parameters are represented by α_i, β_j, γ_k, and δ_l, where α_i denotes the effect of baseplate temperature at the ith level when the other parameters are fixed. Similarly, β_j, γ_k, and δ_l represent the effects of amplitude, weld speed, and normal force at the jth, k^{th}, and l^{th} levels, while the other parameters are fixed. The error variable, ϵ_{ijklt}, is a variable with normal distribution and zero mean which denotes any nuisance variation in the response. All ϵ_{ijklt} are mutually independent with respect to i, j, k, l, and t.

After shear tests and temperature measurements were completed, analysis of variance (ANOVA) was first performed to determine the statistical significance of each parameter with respect to the response variables. Then, main effects plots were used to further analyze the effect of each parameter and to indicate the optimal levels of the parameters for shear strength within the current process window.

3.2   Results

3.2.1   Temperature Measurement and Shear Test

Representative temperature measurement plots for a low peak temperature and a high peak temperature are shown in Table 3.4 and Figure 3.4, where PS16 produces a high peak temperature and PS5 gives a low peak temperature.

Similarly, representative shear test results for a poor weld and a good weld are shown in Table 3.5 and Figure 3.5. In this study, a poor weld is defined as a weld that possesses a shear strength less than 60% of the bulk 4130 material [1]. A good

weld is defined as a weld that possesses a shear strength greater than 60% of the bulk 4130 material. PS9 generates a poor weld and PS11 yields a good weld. It should be pointed out that three samples were intended to be tested for each condition. Forty-eight shear samples were intended to be made, however twelve of them for different treatment combinations failed during machining and preparation. For the data presented in Table 3.5 and Figure 3.5, one shear sample for PS11 failed before testing. Thus, no data was obtained for that sample.

Table 3.4: Interfacial temperature measurements for representative low peak temperature (PS9) and high peak temperature (PS16) samples.

Sample	PS9	PS16
1	548 °C	921 °C
2	547 °C	878 °C
Mean	548 °C	900 °C

Table 3.5: Shear test results for representative bad weld (PS9) and good weld (PS11) samples.

Sample	PS9		PS11	
	Max force (N)	Max shear strength (MPa)	Max force (N)	Max shear strength (MPa)
1	958.1	138.5	2583.0	366.6
2	759.4	111.8	2754.4	382.1
3	891.2	131.2	N/A	N/A
Mean	869.6	127.1	2668.7	374.4
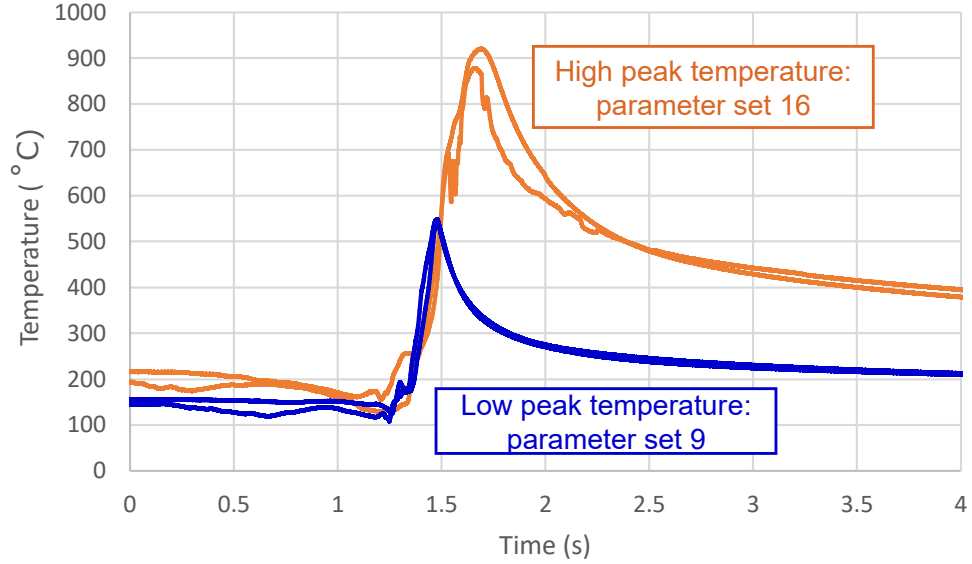
Figure 3.4: Representative interfacial temperature measurement plots.

3.2.2   Statistical Analysis of Interfacial Temperature

An ANOVA with interfacial peak temperature as the response variable was first studied. The variability in the shear test results was partitioned into model effects and random error. The adjusted type I error probability, alpha, selected for this experiment was 0.05 to test each of the weld parameters. This alpha level is the threshold probability that the null hypothesis is rejected due to a false positive error (type I error). The p-value is the probability of obtaining a test at least as extreme as the observation, assuming that the null hypothesis of no effect is true. Lower p-values indicate stronger evidence against the null hypothesis. When the p-value is less than alpha, the null hypothesis is rejected in favor of the alternative hypothesis. In this study, the ANOVA was performed using Minitab statistical software (Minitab Inc., State College, PA). As shown in Table 3.6, amplitude, welding speed, and normal
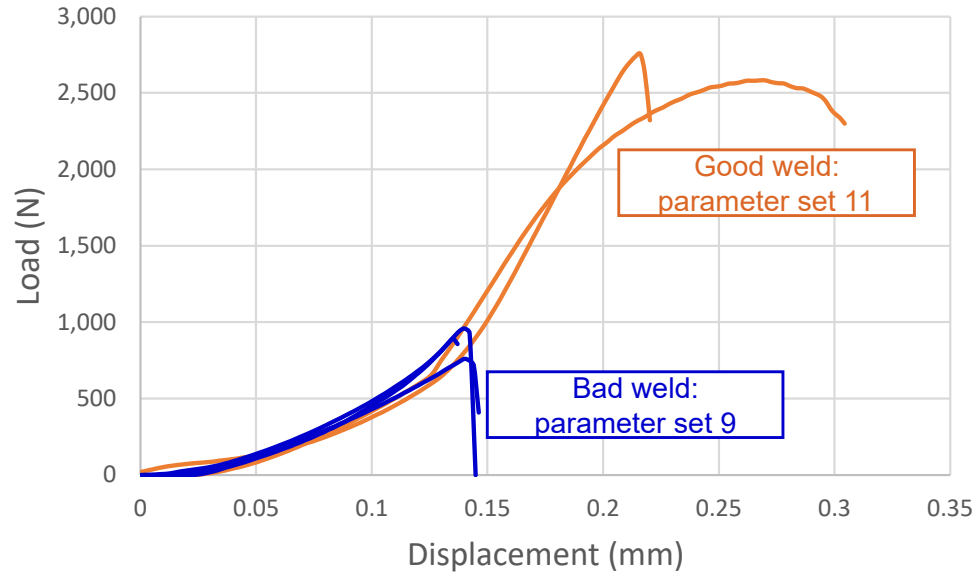
Figure 3.5: Representative shear test load-displacement curves.

force are considered statistically significant with p-values less than 0.05. The base-plate temperature is the only parameter that is considered insignificant with a p-value above 0.05.

The main effect plots agree with the ANOVA as shown in Figure 3.6. The base-plate temperature plot shows that interfacial temperature stays nearly the same for levels 1, 2, and 3. The interfacial temperature increases as baseplate temperature increases from level 3 to 4. Increasing the amplitude increases the interfacial temperature in general, despite a slight decrease when increasing from level 2 to 3. In contrast, the interfacial temperature increases as the welding speed decreases. The normal force exhibits a mixed impact on the interfacial temperature. The interfacial temperature is higher at levels 1 and 4 than at levels 2 and 3 for normal force.

Table 3.6: ANOVA using interfacial temperature as response variable.

Source	DF	Adj SS	Adj MS	F-Value	P-Value
Baseplate temperature	3	23244	7748	3.05	0.054
Amplitude	3	198181	66060	26.02	0.000
Welding speed	3	277357	92452	36.41	0.000
Normal force	3	73427	24476	9.64	0.000
Error	16	48245	2539	•	•
Total	31	620454	•	•	•

3.2.3 Statistical Analysis of Shear Test

The dependence of shear strength on the weld parameters was also analyzed by ANOVA. As shown in Table 3.7, amplitude and normal force have a statistically significant effect on shear strength, with p-values less than 0.05. Baseplate temperature and welding speed are considered insignificant with p-values greater than 0.05.

Table 3.7: ANOVA using shear strength as response variable.

Source	DF	Adj SS	Adj MS	F-Value	P-Value
Baseplate temperature	3	9591	3197	0.94	0.44
Amplitude	3	34001	11334	3.32	0.04
Welding speed	3	23351	7784	2.28	0.109
Normal force	3	31653	10551	3.09	0.049
Error	21	71655	3412	•	•
Total	33	229496	•	•	•

Main Effects Plot for Means
Data Means
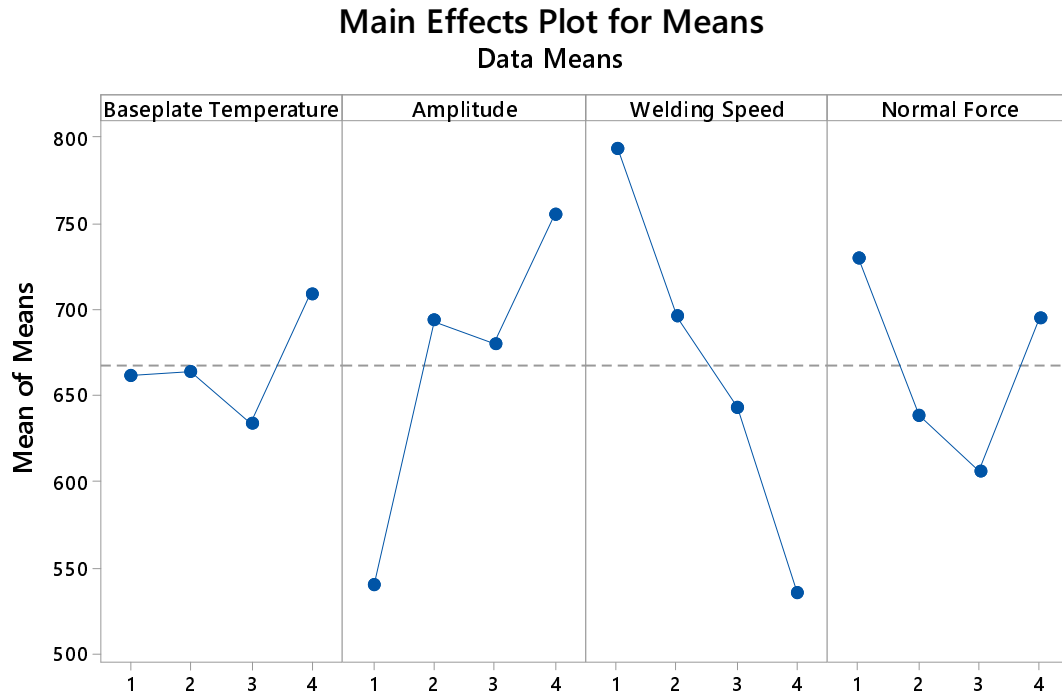
Figure 3.6: Main effect plots for interfacial temperature.

To further investigate the effect of weld parameters, main effect plots are analyzed and provided in Figure 3.7. The baseplate temperature plot shows that the lowest level 1 exhibits the smallest shear strength. Increasing baseplate temperature from level 1 to level 2 increases the shear strength. However, further increasing the baseplate temperature generates very little change in response. The flat pattern for levels 2, 3, and 4 explains why baseplate temperature is not statistically significant with a p-value greater than 0.05. The amplitude plot shows a continuous increase in shear strength with increasing amplitude, which agrees with the ANOVA results. The increase in response is minimal when increasing from level 1 to 2 or from level 3 to 4. The increase is more significant when increasing from level 2 to 3. The shear

strength decreases significantly when the welding speed increases from level 1 to level 2. The shear strength stays nearly the same when the welding speed further increases from level 2 to level 4. The normal force reaches a peak at level 3 and the plot trend is different than those for other parameters.

Main Effects Plot for Means
Data Means
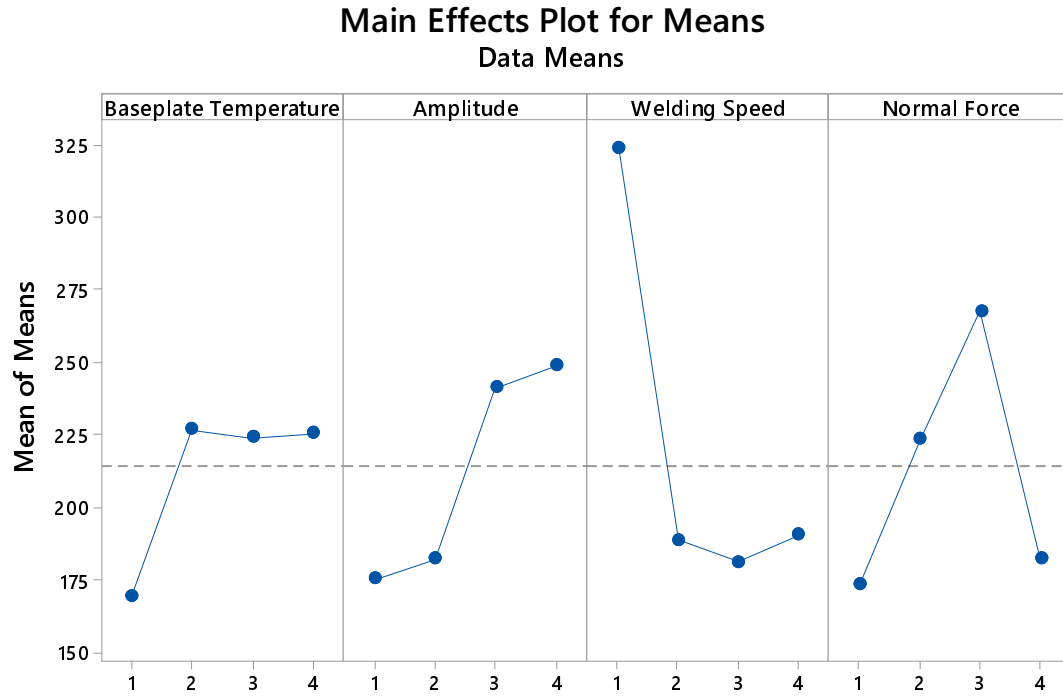
Figure 3.7: Main effect plots for shear strength.

3.3   Discussion

As the ANOVA and the main effects plots show, amplitude was found to be one of the most influential parameters for both interfacial temperature and shear strength. Increasing amplitude enhances the scrubbing action which collapses asperities and

disperses oxides and contaminants at the interface. These actions lead to localized plastic deformation, which are favorable for the formation of strong metal welds. The heat generated from the scrubbing actions and local plastic deformation increases interfacial temperature. However, it is expected that as amplitude increases beyond a certain upper threshold, excessive plastic deformation may occur at the interface and lead to increased void density, which causes a decrease in shear strength.

Normal force was also found to have a significant effect on both interfacial temperature and shear strength. This result is different from the findings for UAM Al 6061 [80], which may be due to the hardness difference between Al alloys and high strength steel. The steel requires higher normal force to reach a maximum compression point at which no more asperities can collapse. The difference in material properties and normal force ranges may contribute to the different effect on interfacial temperature and shear strength.

Welding speed was found to be statistically significant for interfacial temperature, but insignificant for shear strength. With other parameters set the same, a slower welding speed allows higher energy input at the interface, which generates more heat during the welding process. It is found that increasing the welding speed from 40 in/min (16.93 mm/s) to 60 in/min (25.40 mm/s) has a significant negative effect on shear strength. However, the shear strength stays nearly the same when changing the welding speed from 60 in/min (25.40 mm/s) to 80 in/min (33.87 mm/s) or 100 in/min (42.33 mm/s). This indicates that the upper threshold for making a strong UAM 4130 steel weld within the process window investigated is between 40 in/min (16.93 mm/s) and 60 in/min (25.40 mm/s). Beyond that point, the shear strength would decrease

significantly and then stay nearly the same when continuing to increase the welding speed.

The baseplate temperature was found to be an insignificant factor for interfacial temperature and shear strength. The interfacial temperature is caused by the heat input from the baseplate and the heat generated during welding. Since the heat input to the welding interface from the baseplate is much lower than the heat generated from friction and plastic deformation during welding, the baseplate temperature is expected to have a smaller effect on the interfacial temperature. In a recent study [27], the baseplate temperature is found to be critical for achieving a high strength baseplate-foil weld. However, that statement may not hold for foil-foil welding, which is investigated in this study. In the pilot study for finding viable parameters, the parameter combinations listed in the DOE table were used for welding the first layer of foil to the baseplate. However, all the treatment combinations with lower baseplate temperatures 100 °F (37.8 °C) or 200 °F (93.3 °C) generated no welds or weak welds that could be easily peeled off by hand.

The relationship between interfacial temperature and shear strength is studied. The Pearson correlation coefficient is found to be 0.227, which means that the two response variables are positively correlated. However, since the coefficient is less than 0.3, the correlation is not strong. This analysis indicates that interfacial temperature may affect the shear strength of foil-foil a weld interface. However, other factors may play a more influential role in achieving a high shear strength weld [2].

3.4 Summary

A design of experiments study using a Taguchi L16 design array was carried out on carbon steel 4130 to investigate the effect of weld parameters including baseplate temperature, amplitude, welding speed, and normal force on the interfacial temperature and shear strength. Analysis of variance and main effect plots show that normal force and amplitude have a statistically significant effect on shear strength, while similar analyses show that normal force, amplitude, and welding speed are significant for interfacial temperature. The Pearson correlation coefficient is found to be 0.227, which indicates a weak positive correlation between interfacial temperature and shear strength. While the shear strength can be treated as a strong indicator of the weld quality, the interfacial temperature is a relatively weak indicator. Within the selected process window, the following combination of process parameters tested in this DOE study generates the highest shear strength: baseplate temperature of 400 °F (204.4 °C), amplitude of 31.5 μm, welding speed of 40 in/min (16.93 mm/s), and normal force of 6000 N.

Chapter 4

Analysis of Residual Stress and Modeling of Fatigue Behavior during UAM Welding of Steel

Overview

This chapter discusses potential causes of the fatigue cracking observed at the interface between the baseplate and the first layer of foil during UAM welding of steels. Strategies to mitigate this cracking are also proposed. The first study uses neutron diffraction to measure the residual stress formed in the UAM steel 4130. The second study proposes a numerical modeling approach for describing the stress distribution and predicting the fatigue performance of UAM steel builds.

4.1 Neutron Diffraction Residual Stress Measurement in Carbon Steel 4130 Fabricated by Ultrasonic Additive Manufacturing

Additive manufacturing (AM), which is also know as 3D printing, has grown and evolved significantly in recent years. Different from conventional subtractive manufacturing where excess material is removed from the feedstock to achieve particular shapes and dimensions, AM builds near-net shape parts directly through layer-by-layer deposition. This enables AM to produce complex geometries and arbitrary internal features, which are difficult to create using traditional methods [31]. However, one common concern in fusion-based metal AM, such as selective laser melting (SLM), directed energy deposition (DED) or direct metal laser sintering (DMLS), is the relatively high residual stress caused by steep thermal gradients during the process. Particularly, if the residual stress is higher than the local yield strength of the material, premature fracture, such as cracking and delamination, may occur during the deposition [15, 6, 8, 20]. In general, surface tensile residual stress, which is commonly found in as-printed fusion-based AM material, can be detrimental to mechanical and fatigue properties of the material. Surface compressive residual stress is desired and improves fatigue performance of the material, which can be introduced by using surface preparation techniques such as shot peening [18].

Various destructive and non-destructive methods have been utilized to measure residual stresses in AM material. One common destructive method is the hole drilling method, where strain changes around a hole during the drilling process is measured to determine stress [9]. However, the destructive character of this method prevents sequential measurements in the same component after the hole drilling procedure. The

low penetration depth and limited resolution are of concern as well. X-ray diffraction (XRD) and neutron diffraction are two most widely used non-destructive methods for measuring residual stress in metals [5, 21]. They both measure interplanar spacing to calculate residual stress. XRD has relatively low penetration depth (about 5 μm for steels). Neutron diffraction has a deep penetration depth (about 50 mm for steels), which is more favorable for measuring residual stress at depth [21, 20]. Thus, neutron diffraction is selected to measure residual stresses in UAM 4130 steels for the first time. Residual stresses in various locations of UAM 4130 steel components have been mapped to determine the aggregating and distribution of residual stresses in UAM samples.

4.1.1 Experimental Methods

Residual stress in UAM steel samples with different height was measured to understand how welding more layers affect the formation of residual stress. In this study, 5-layer, 10-layer and 15-layer UAM 4130 samples without delamination were made using a 9 kW Fabrisonic SonicLayer 4000 UAM system. Each sample was made from 0.127 mm (0.005 in) thick, 25.4 mm (1 in) wide annealed AISI 4130 steel foils and 12.7 mm (0.5 in) thick ASTM A36 carbon steel baseplates. The thickness of the baseplate was reduced to 6.35 mm (0.25 in) to satisfy the neutron penetration requirement. The welding parameters are shown in Table 4.1.

Residual stress measurements using neutron diffraction were conducted by collaborators from the NIST Center for Neutron Research. The neutrons used for this work was generated from a high flux reactor. The lattice interplanar spacing d_{hkl} for

Table 4.1: Process parameters used to weld UAM 4130.

Parameters	Levels
Normal force (N)	6500
Vibration amplitude (μm)	28.0
Weld speed (mm/s)	21
Baseplate temperature (°C)	204

specific lattice planes {hkl} was measured. Then the following equation was used to calculate the elastic lattice stain in the selected gauge volume [51]:

$$\epsilon_{hkl} = \frac{d_{hkl} - d_{0,hkl}}{d_{0,hkl}} \tag{4.1}$$

where $d_{0,hkl}$ is the strain-free lattice spacing. There are multiple methods to determine this variable [76]. The method selected in this study is to use the plane stress condition $\sigma_{zz} = 0$, because the UAM samples are thin slices. Residual stresses in the principal directions can be calculated using Hooke's law:

$$\sigma_{ii} = \frac{E_{hkl}}{(1 + \nu_{hkl})(1 - 2\nu_{hkl})}[(1 - \nu_{hkl})\epsilon_{ii} + \nu_{hkl}(\epsilon_{jj} + \epsilon_{kk})] \tag{4.2}$$

where E_{hkl} and ν_{hkl} are the elastic modulus and Poisson ratio for a specific {hkl} plane direction. Because of the assumption of plane stress condition $\sigma_{zz} = 0$, σ_{xx}, σ_{yy}, and $d_{0,hkl}$ can be calculated from three measured interplanar spacings d_{hkl} along principal directions.

A gauge volume of $0.5\,\text{mm} \times 0.5\,\text{mm} \times 2\,\text{mm}$ is used. Crystal planes {211} are selected for the diffraction measurements from body centered cubic material AISI

Table 4.2: Residual stress measurement locations and dimensions of UAM 4130.

Sample	Dimension (mm)	Coordinates of center (y,z) @ x=-28 mm, 0 mm, and 28 mm
5-layer	63.5 ×15.24 × 0.635	A(0, 0.3) B(7, 0.3)
10-layer	63.5 ×15.24 × 1.27	A(0, 0.3) B(7, 0.3) C (0, 0.935) D(7, 0.935)
15-layer	63.5 ×15.24 × 1.905	A(0, 0.3) B(7, 0.3) C (0, 0.935) D(7, 0.935) E(0, 1.57) F(7, 1.57)

4130. Measurement locations are shown in Figure 4.1. Corresponding coordinates and dimensions are shown in Table 4.2. Residual stress at different y and z locations at three different x planes was measured for each sample. In total, 6 locations of the 5-layer sample, 12 locations of the 10-layer sample, and 18 locations of the 15-layer sample were measured. The coordinate system of the samples is defined as the accumulating direction (z), the vibration direction (y), and the rolling direction (x).

4.1.2   Results and Discussion

Residual stress components σ_{xx} and σ_{yy} along the rolling direction x for every sample are shown in Figure 4.2. For the 5-layer sample, the changes in σ_{xx} and σ_{yy} show a similar pattern, where the stress near the end (x=28 mm) is higher than stress at the start and middle of the sample. As more layers are deposited, the residual stress changes along the x direction become random. It can also be seen that the maximum tensile residual stress stays nearly the same as 176.5 MPa for 15-layer sample compared to 163.3 MPa for 5-layer sample, which indicates that the fatigue property of UAM steel sample does not change much in terms of residual stress as more layers are being deposited.
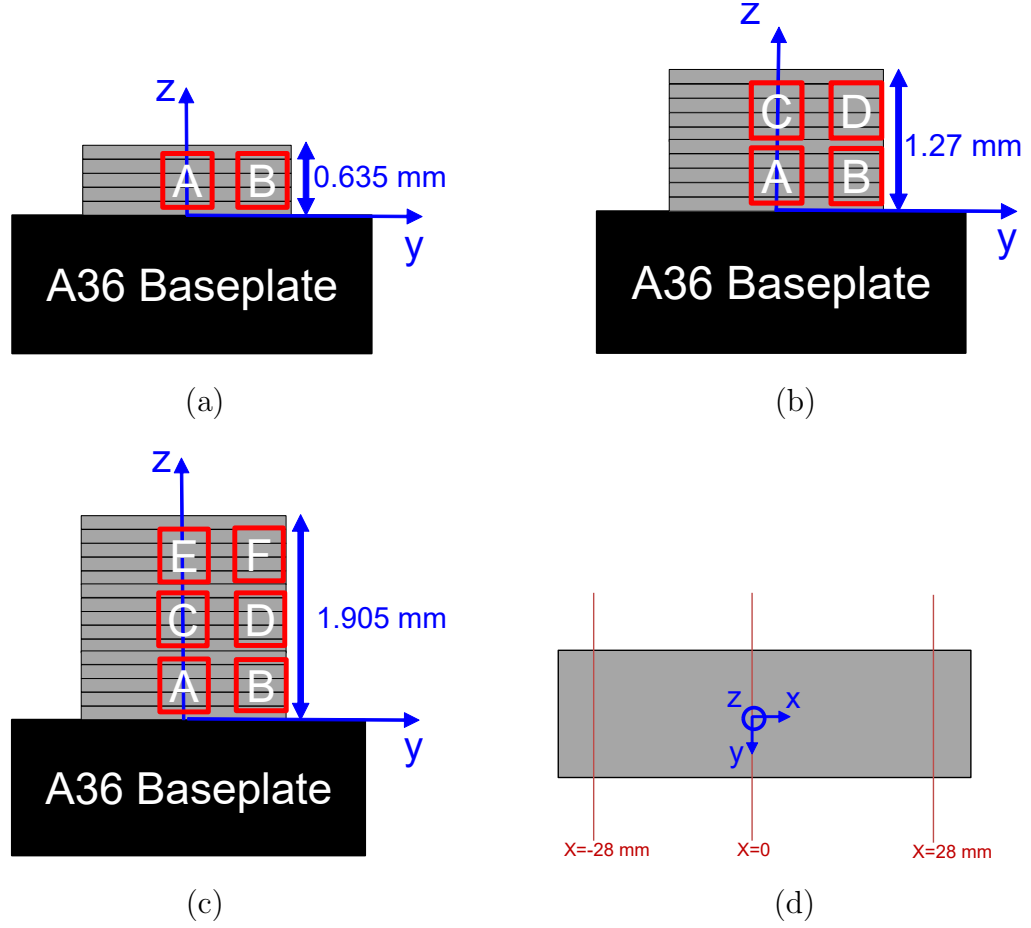
Figure 4.1: Cross-section views of measurement locations of (a) 5-layer, (b) 10-layer, and (c) 15-layer UAM 4130. Top view of measurement locations for each sample is shown in (d).

Figure 4.3 shows residual stress components σ_{xx} and σ_{yy} along vibration direction y for different x and z locations of different samples. For the same z height and y location, σ_{xx} and σ_{yy} reach maximum tensile value near the end (x=28 mm) of the sample in most of the cases. This may be caused by greater thermal expansion and contraction of material at the end, where heat aggregates at the welding interface. With the exception of four points found in 5-layer and 10-layer samples exhibiting
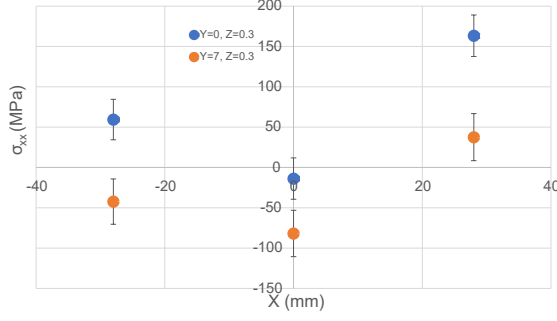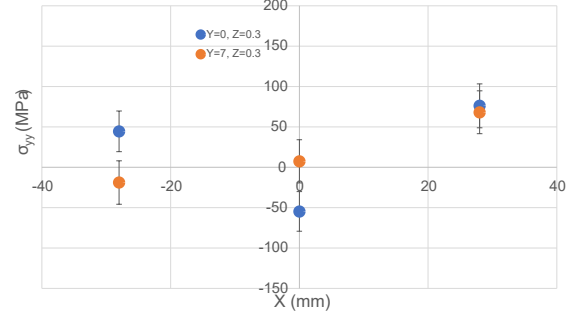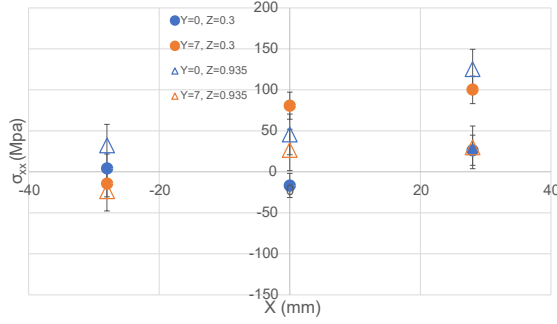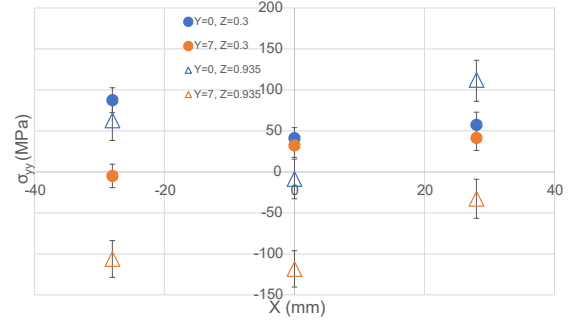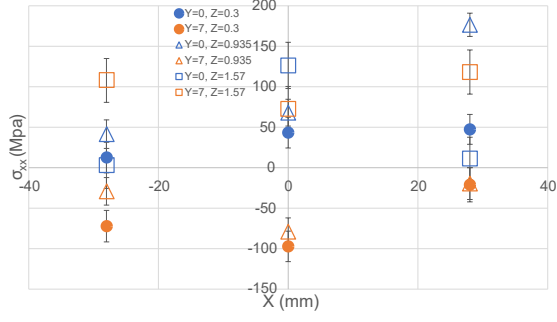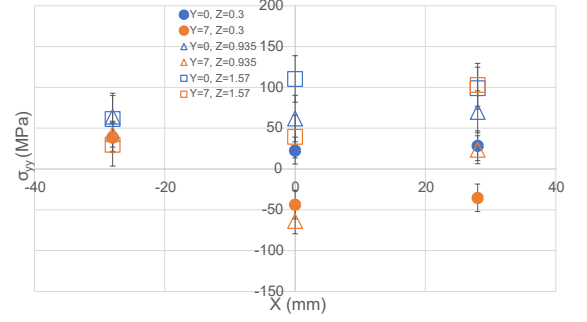
Figure 4.2: Residual stress components σ_{xx} and σ_{yy} along the x direction for (a)(b) 5-layer, (c)(d) 10-layer, and (e)(f) 15-layer UAM 4130.

negative compressive residual stress near the center (y= 0 mm), all other compressive residual stresses are found near the edge (y=7 mm).
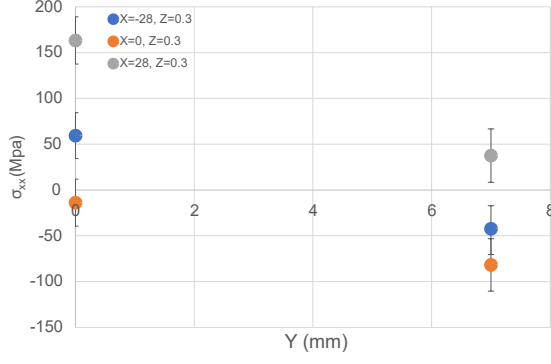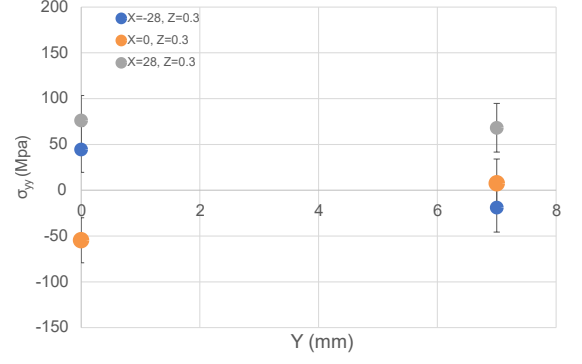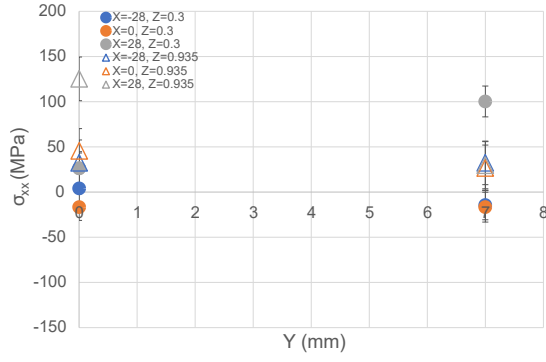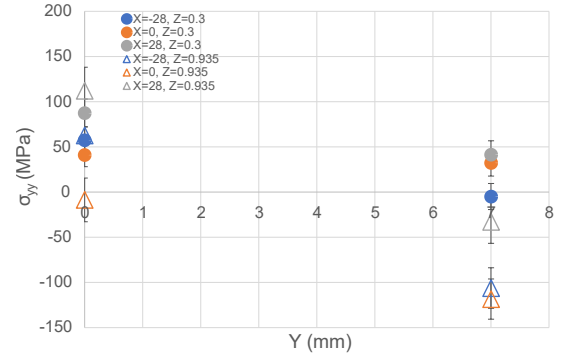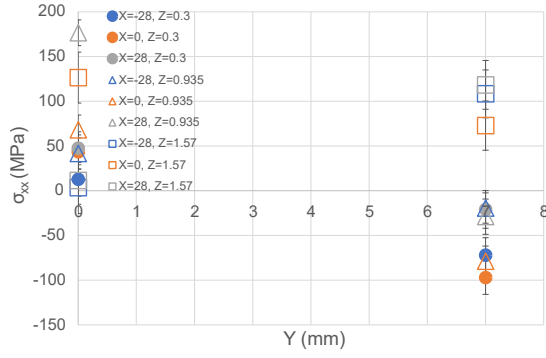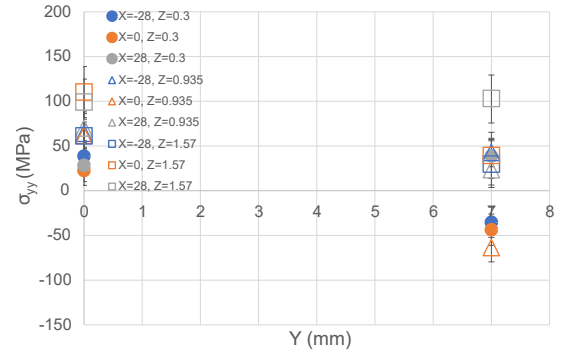
Figure 4.3: Residual stress components σ_{xx} and σ_{yy} along the y direction for (a)(b) 5-layer, (c)(d) 10-layer, and (e)(f) 15-layer UAM 4130.

The max tensile residual stress of UAM 4130 steel is found at 176.5 MPa, which is much lower than the maximum tensile residual stress of steel samples made via other fusion-based additive manufacturing processes, as summarized in Table 4.3. Lower residual stress indicates that UAM samples possess a better fatigue property than other fusion-based AM samples.

Table 4.3: Comparison of residual stress in AM made steels.

AM method	Material	Maximum tensile residual stress (MPa)
SLM [58]	AISI 316L	250
DMLS [8]	17-4 stainless steel	400
DMLS [20]	AISI 316L	400
DED [82]	Mix of AISI 316L and AISI P21	430
UAM	AISI 4130	176.5

4.1.3 Summary

In this study, residual stresses in carbon steel 4130 samples that were made using ultrasonic additive manufacturing (UAM) were measured for the first time using neutron diffraction technique. The aggregating pattern and distribution of residual stress in UAM 4130 were reported. Unlike large tensile residual stress found in fusion-based additive manufactured steels, the maximum tensile residual stress for UAM 4130 is found relatively low as 176.5 MPa. This measurement indicates a potentially better fatigue performance of as-printed UAM material. For the same z height, residual

stresses in UAM 4130 are found to reach maximum near the end of rolling direction in most of the cases.

4.2   UAM Fatigue Model

During UAM steel welding, undesired cracking can occur between the baseplate and the first layer of foil as build height increases, as shown in Figure 1.15. It is speculated that the observed cracking is fatigue cracking caused by high frequency vibration. During the welding, the combined action of a force normal to metal foil feedstock and ultrasonic (20 kHz) transverse vibrations creates localized plastic deformation and generates gapless metallurgical bonds at the interface. However, after this interface is formed, welding of subsequent layers would continue to apply a high frequency cyclic shear force and aggregate fatigue damage at that interface. Among all the interfaces, the interface between the baseplate and the first foil (0th interface) experiences more cycles of shear forces than any other interface. Thus, the research in this work focuses on the fatigue behavior of that specific interface. There is no work in the literature on characterization and prediction of UAM cracking phenomena. A comprehensive modeling approach is developed in this study to predict the crack initiation at that interface. The expectation is that less aggressive welding parameters, especially lower welding amplitude and faster welding speed, will improve the fatigue performance. However, the weld process needs to maintain interfacial strength while reducing fatigue stress and cycles.

4.2.1 Model Solid Material under UAM-type Stress Cycles

A finite element (FE) model is developed in Abaqus to analyze the quasi-static stress distribution of a bulk steel part under UAM welding conditions at different build heights. The stress distribution data is then used as an input to an FE fatigue model built in FE-SAFE. The fatigue damage of the part is calculated. If the simulation shows that the solid part does not have fatigue cracking under UAM welding conditions, it suggests that the loading on the formed UAM interface is what causes the cracking.

Table 4.4: Process parameters used to define the FE model.

Parameters	Levels
Normal force (N)	6500
Vibration amplitude (μm)	29.0
Weld speed (mm/s)	21
Baseplate temperature (°C)	204

The UAM welding parameters used to define the FE model are shown in Table 4.4. Using this set of parameters to weld 0.127 mm (0.005 in) thick, 25.4 mm (1 in) wide annealed 4130 steel foils onto AISI 4130 steel baseplate results in cracking initiation at the 0th interface after welding layer 10. Because the normal force is not cyclic loading, it is not modeled; only cyclic shear force is simulated. Since FE simulation show that only shear force does not cause plastic deformation, plasticity of the material is not considered. The three-dimensional FE stress model is defined using elastic
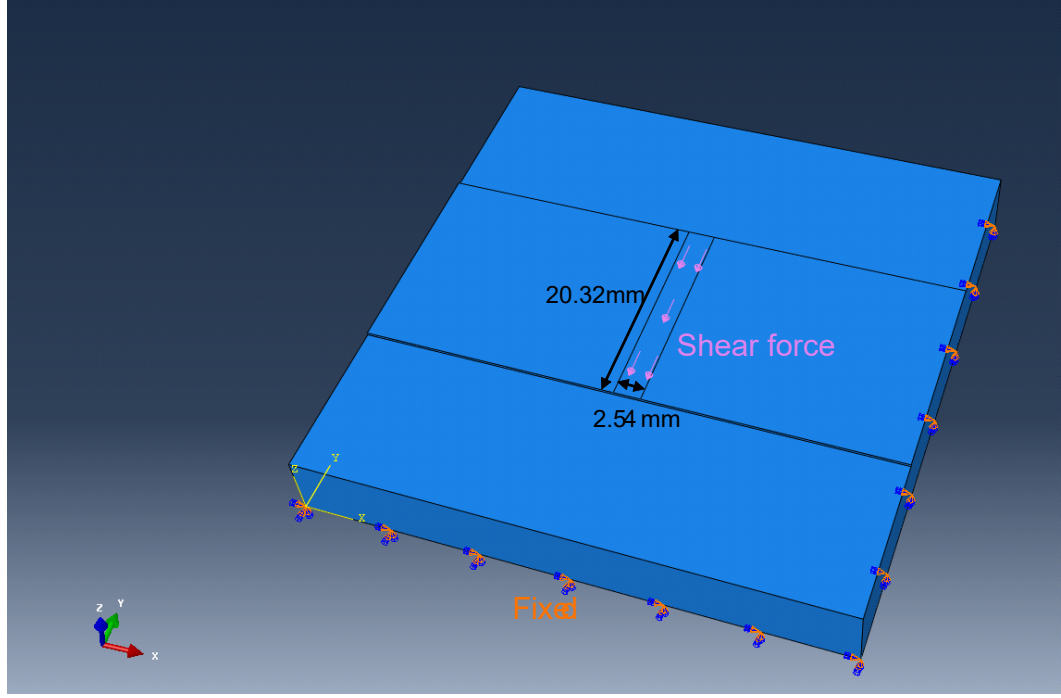
Figure 4.4: Model configuration, boundary conditions and critical dimensions of the 2-layer high solid sample.

material properties of 4130 steel. Model configuration, boundary conditions, and critical dimensions of the 2-layer high solid sample are shown in Figure 4.4. It is presumed that the welding of the first layer of foil onto the baseplate would not introduce any fatigue damage to the 0th interface; instead it forms the 0th interface. The welding of the second layer of foil onto the build is expected to be the first welding that introduces fatigue stresses onto the 0th interface. The width of the contact surface is estimated to be 2.54 mm (0.1 inch), which is based on empirical evidence [30]. The width of the welding area is 20.32 mm and the thickness of the 2-layer high solid sample is 0.254 mm. Both of these values are from the experimental setup. The shear load applied on the contact surface is estimated at 3266 N using a

linear time invariant (LTI) model from a previous study [29]. The bottom surface of the baseplate is fixed to simulate the constraint from the vacuum chuck used in the experiment. The stress distribution map is calculated and shown in Figure 4.5. A maximum stress of 121 MPa is reached in the build.
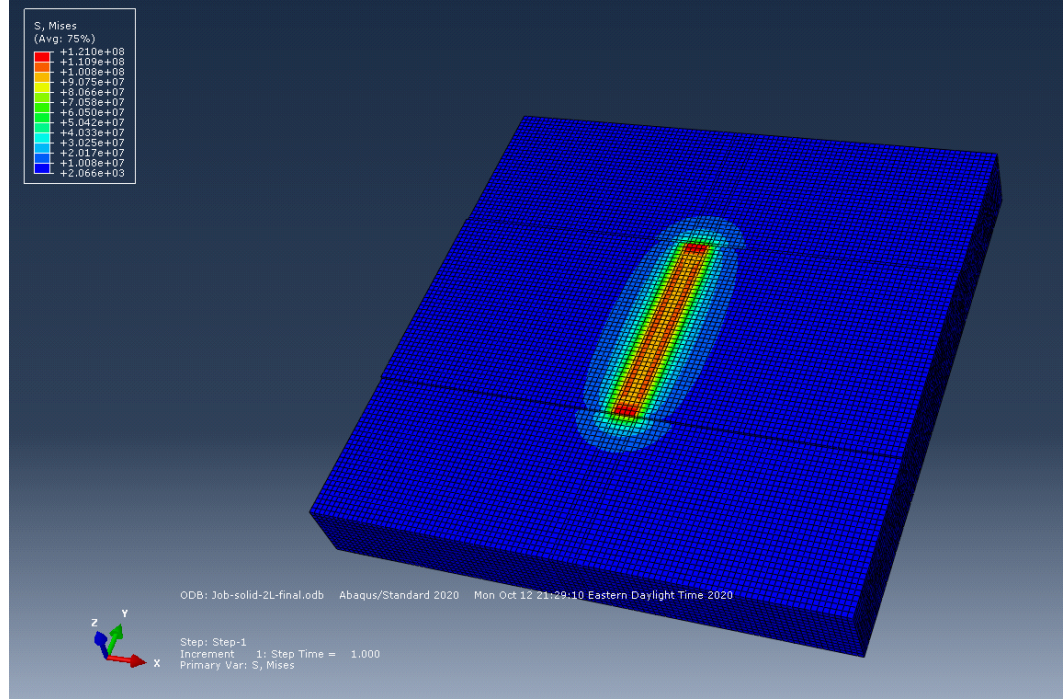
Figure 4.5: Stress distribution map of the 2-layer high solid sample.

The fatigue model is then built on top of the stress model. The stress state shown in Figure 4.5 is presumed to follow sine waves. The fatigue properties of carbon steel 4130 (S-N curve) are defined and approximated by using ultimate tensile strength (UTS) and elastic modulus (E), where the UTS is measured by tensile testing of 4130 steel foils used in the experiment and the E is obtained from reference. The tensile testing was repeated three times. The properties used in this model are shown

in Table 4.5. The fatigue damage map is calculated and shown in Figure 4.6. The damage is defined as 1/life. In other words, when $damage = 1$, the fatigue cracking initiates. As shown in Figure 4.6, the damage per loading cycle is estimated at zero, which indicates no aggregated damage on the solid part. The same modeling procedures and calculations were repeated on 3-layer, 5-layer, and 7-layer high solid samples. The results show that the maximum stress in the part becomes lower as the sample height increases. The lower stresses also lead to zero fatigue damage. In conclusion, premature fatigue cracking would not occur in the solid 4130 steel samples under UAM-type stress cycles.

Table 4.5: Material properties of carbon steel 4130 used to define the model.

Properties	Levels
UTS	576 MPa
E	190 GPa [1]

4.2.2   Model UAM Welding of Steel

Model the 0th Interface

As indicated from the analysis of the solid steel 4130, the cyclic loading applied on the formed UAM steel welding interface is proved what causes the cracking initiation. Thus, it is critical to characterize and define the interface. Since previous studies have demonstrated that the UAM interface possesses a weaker mechanical strength compared to the bulk material, it is inappropriate to model the interface with the same material properties as the bulk material. Thus, this study defines the interface as a "new" material that has the same elastic modulus and a portion of the strength
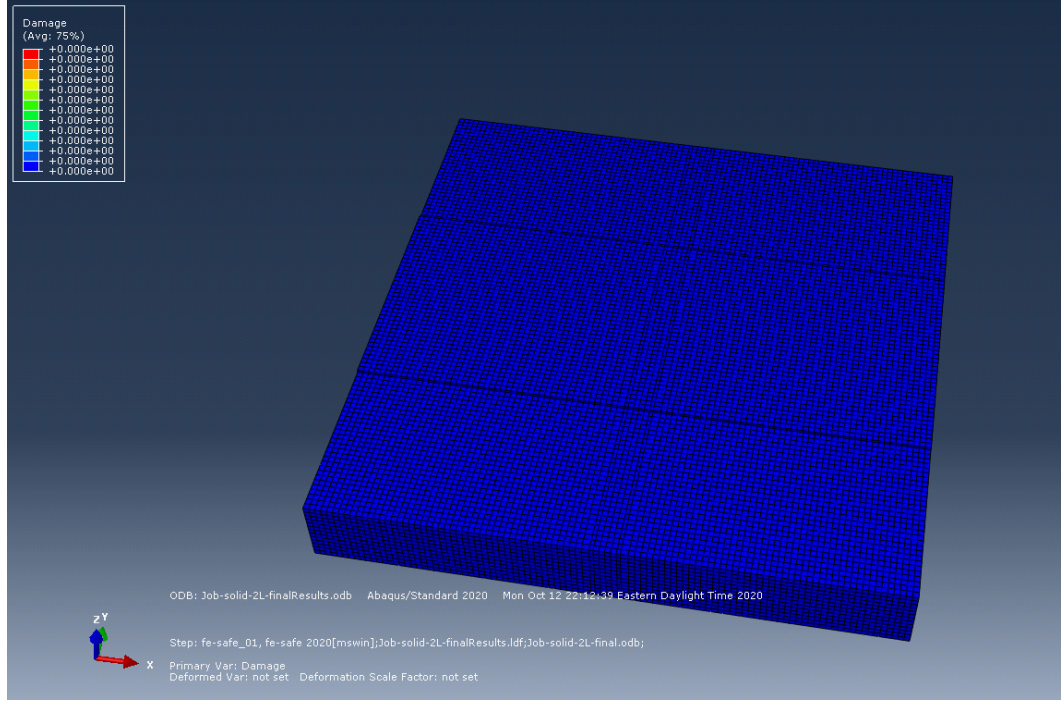
Figure 4.6: Fatigue damage map of the 2-layer high solid sample.

of the bulk material. The elastic modulus and ultimate tensile strength are needed to model and simulate the fatigue performance of a certain material. However, the ultimate tensile strength of the interface is nearly impossible to be obtained directly. Since the ultimate tensile strength (UTS) is found to have a linear relation with the ultimate shear strength (USS) of a certain material [55], the shear test presented in Chapter 2 are used to characterize the interface. Then, an effective strength coefficient α is defined as follow:

$$\alpha = \frac{\tau_{USSI}}{\tau_{USS}} = \frac{\sigma_{UTSI}}{\sigma_{UTS}} \tag{4.3}$$

where τ_{USSI} is the USS of the interface that is measured from shear testing, τ_{USS} is the known USS of the carbon steel 4130 [1], and σ_{UTS} is the known UTS of carbon steel 4130 obtained from tensile testing. The UTS of the interface σ_{UTSI} can then be calculated using this equation.

In this study, nine layers of 0.127 mm (0.005 in) thick, 25.4 mm (1 in) wide annealed 4130 steel foils were welded onto AISI 4130 steel baseplate using a Fabrisonic SonicLayer 4000 9 kW UAM system. The welding parameters are listed in Table 4.4. Three shear stepped samples were made and tested on an MTS C43.504 50 kN load frame following the procedure introduced in Chapter 2. An average shear strength of 118 MPa is obtained. Thus, using equation 4.3, the α is calculated as 0.347 and the UTS of the interface is calculated as 200 MPa. All the strengths mentioned here are under room temperature (RT) and are listed in Table 4.6.

Table 4.6: Material properties under room temperature (RT) that are used to define the FE fatigue model.

Properties	Steel 4130	UAM 4130 interface
E	190 GPa	190 GPa
UTS	576 MPa	200 MPa
USS	340 MPa	118 MPa

Another significant factor that affects the mechanical properties of the interface is the interfacial temperature. Previous studies show that the interface can reach a peak temperature of 400 °C to 900 °C depending on process conditions [27]. Such elevated temperatures lead to a reduction in elastic modulus and mechanical strength

of the interface during welding. To incorporate the effect of interfacial temperature into the fatigue model, a two-dimensional FE heat transfer model was built. The model is similar to one presented in a previous study [70]. The heat flux for a certain combination of parameters is back calculated based on the peak temperature measured for welding one layer of foil onto the baseplate. Then, the same calculated heat flux is used on UAM builds with different heights to get the peak temperature of the 0th interface during welding subsequent layers. In this study, a thermocouple measurement was performed following the procedure introduced in Chapter 2. The peak interfacial temperature for welding 4130 steel foils onto a 4130 baseplate using parameters presented in Table 4.4 is measured at 562 °C. The heat flux is then calculated to be 8.55 W/mm using the FE model. The temperature map for the 2-layer UAM 4130 steel is shown in Figure 4.7. Following the same procedure, the interfacial temperatures T_i of the 0th interface while welding the ith layer of foil are simulated and presented in Table 4.7.

Table 4.7: Interfacial temperatures of the 0th interface when welding the ith layer of foil onto the UAM build.

i	T_i (°C)
2	540
3	518
5	482
7	449
9	420
11	396
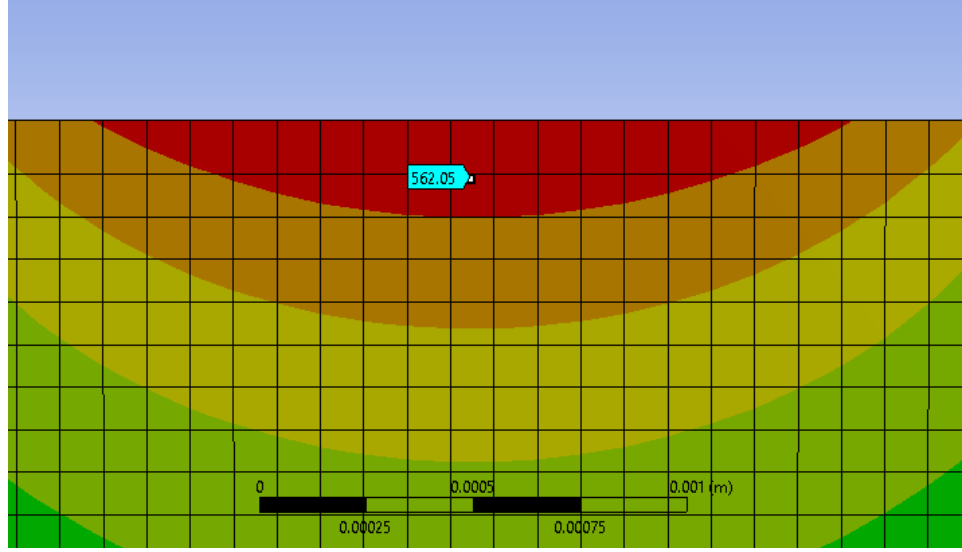
Figure 4.7: Temperature map for the 2-layer UAM 4130 steel sample with the 0th interface position probed.

After interfacial temperatures are obtained from the FE models, the following approximation equations [43] are used to estimate the elastic modulus and ultimate tensile strength at elevated temperatures. First, a modulus reduction coefficient η_E is calculated using:

$$\eta_E = 1 + \frac{T_i}{767 \ln \frac{T_i}{1750}} \tag{4.4}$$

This equation works when T_i is between 0 °C and 600 °C. The elastic modulus at elevated temperature E_{T_i} is calculated as:

$$E_{T_i} = \eta_E \times E \tag{4.5}$$

Then, a strength reduction factor η_S is calculated as follows:

$$\eta_S = a - \frac{(T - b)^n}{c} \tag{4.6}$$

where a, b, c, and n are coefficients with no physical meanings. The values for these coefficients are presented in Table 4.8.

$$\sigma_{T_i,UTSI} = \eta_s \times \sigma_{UTSI} \tag{4.7}$$

Table 4.8: Coefficient values used to calculate the strength reduction factor.

Coefficient	22 °C $< T_i <$ 450 °C	450 °C $< T_i <$ 660 °C
a	0.85	0.85
b	450	450
c	9.6×10^{13}	1.3×10^5
n	5	2

The material properties corresponding to elevated temperatures are shown in Table 4.9. These properties are then used to define the interface material in the FE stress and FE fatigue models. A flow chart to summarize the use of these modeling steps is shown in Figure 4.8.

Model the Stress Distribution in UAM Steel Builds

The model configuration and boundary constraints of the FE stress model of UAM builds are nearly the same as the FE stress model of solid steels. The only difference is that a 10 μm thick layer is defined to represent the 0th interface, as shown in Figure 4.9. As stated in previous sections, the 0th interface is the focus of this study.

Table 4.9: Material properties at corresponding interfacial temperatures.

i	T_i (°C)	$E_{T_i}(GPa)$	$\sigma_{T_i,UTSI}(MPa)$
2	540	90	157.4
3	518	106	162.8
5	482	127	168.3
7	449	142	169.9
9	420	151	169.9
11	396	158	169.9

All subsequent interfaces are presumed not to crack and not modeled in this study. The elastic modulus of the 0th interface at welding the ith layer E_{T_i} is used to define the interface material. The stress distribution map of the 2-layer UAM build is shown in Figure 4.10. A maximum stress of 133 MPa is identified in the UAM build. The same stress modeling calculations were performed on 3-layer, 5-layer, 7-layer, 9-layer, and 11-layer UAM samples.

Model the Fatigue Damage in UAM Steel Builds

The calculated E_{T_i} and $\sigma_{T_i,UTSI}$ from Table 4.9 are used to define the interface. The fatigue damage map of the 2-layer UAM model is shown in Figure 4.11. The damage per cycle of the worst point is calculated as 1.14×10^{-4}. Same fatigue modeling procedure was used to simulate the fatigue damage on 3-layer, 5-layer, 7-layer, 9-layer, and 11-layer UAM samples. Miner's rule is used to calculate the accumulative fatigue damage at the 0th interface, which is caused by welding subsequent layers [71]:

$$\sum_{i=1}^{k} = \frac{n_i \times \sigma_i}{N_i \times \sigma_i} = C \tag{4.8}$$
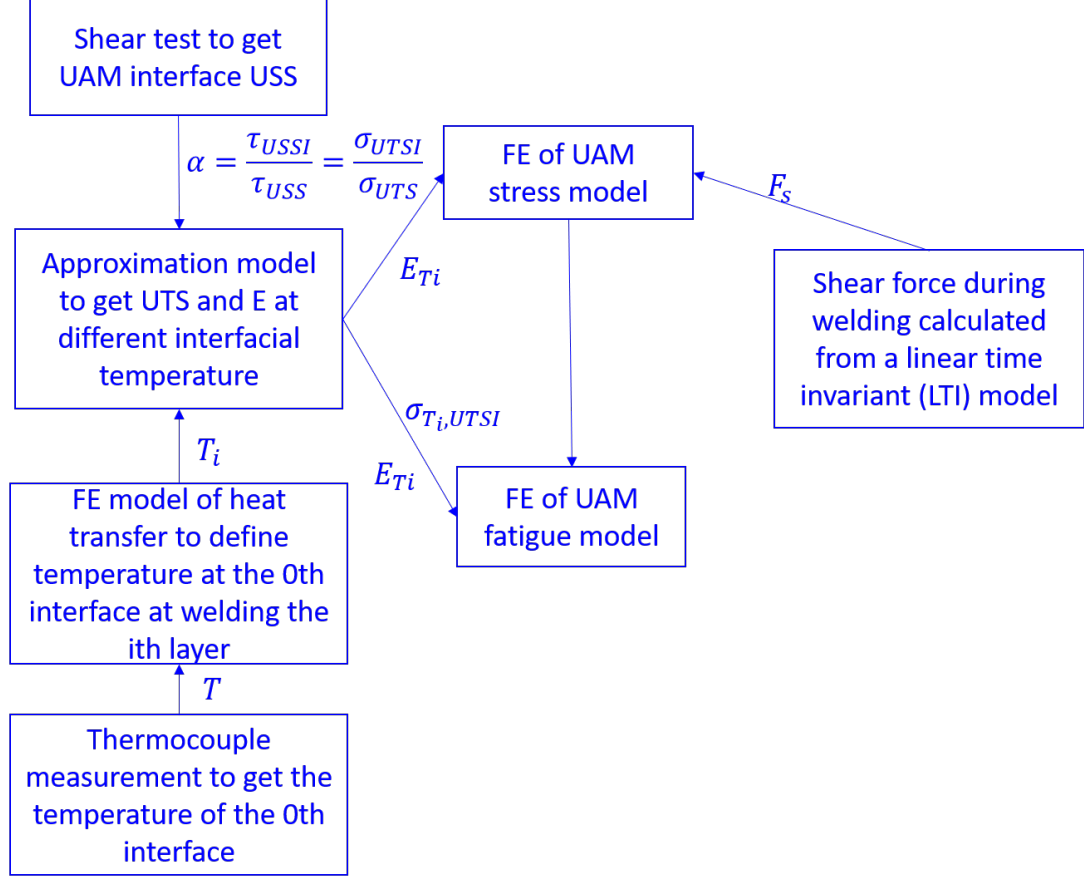
Figure 4.8: Flow chart to illustrate the framework of the model.

where k is the total number of different stress levels, σ_i is the maximum stress caused by welding the ith layer, N_i is the number of cycles needed to fail the 0th interface at the ith stress, n_i is the number of cycles accumulated at stress level σ_i, and C is the fraction of fatigue life consumed by exposure to the cycles at the different stress levels. When the damage fraction C reaches 1, fatigue cracking initiates.

The number of cycles for each stress is calculated using contact width divided by welding speed, which is computed as 2400 for this case. Then, the total damage from welding the ith layer is calculated using that number of cycles times damage per cycle
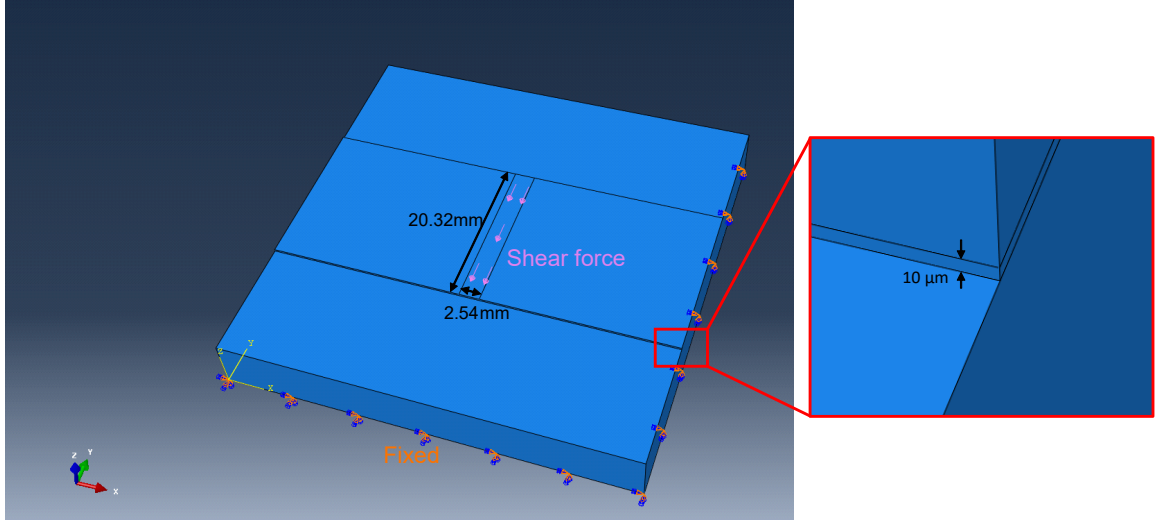
Figure 4.9: Model configuration, boundary conditions and critical dimensions of the 2-layer UAM sample.

of the worst point. It is worth noting that the worst point on the 0th interface may not be the same point for welding different layers. However, to simplify the model, damage per cycle of the worst point from welding different layers was used to estimate the total damage. The fatigue performance of the UAM builds are summarized in Table 4.10 and Figure 4.12. Interpolating from the results, the cracking at the 0th interface is predicted to initiate after welding of layer 10. The simulation predictions are consistent with the experimental observation, which validate the FE models.

4.2.3 Computational Case Studies

To investigate the effect of different factors on the fatigue performance of UAM builds, individual factors including shear strength of the interface, welding speed, and the shear force applied by the sonotrode were varied.
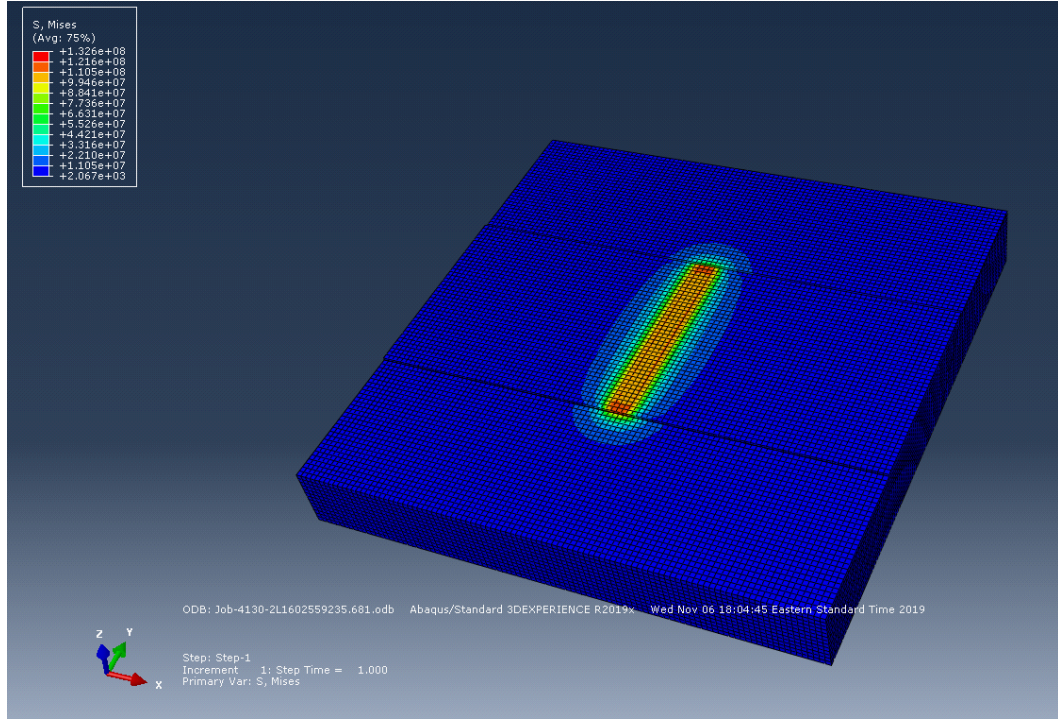
Figure 4.10: Stress distribution map of the 2-layer UAM sample.

Case Study 1 with Varied Shear Strength

The shear strength of the 0th interface is changed from 118 MPa to 170 MPa with other parameters kept the same as those presented in Table 4.4. The feasibility of producing UAM steel builds with such shear strength using these process parameters is not considered. The aim is to investigate the effect of shear strength on the overall fatigue performance of the UAM builds. The simulation results are presented in Table 4.11 and Figure 4.13. The cracking is predicted to occur after welding layer 114. In other words, by improving the shear strength by about 44%, the fatigue cracking is delayed by about 1100% relative to the original cracking initiation time.
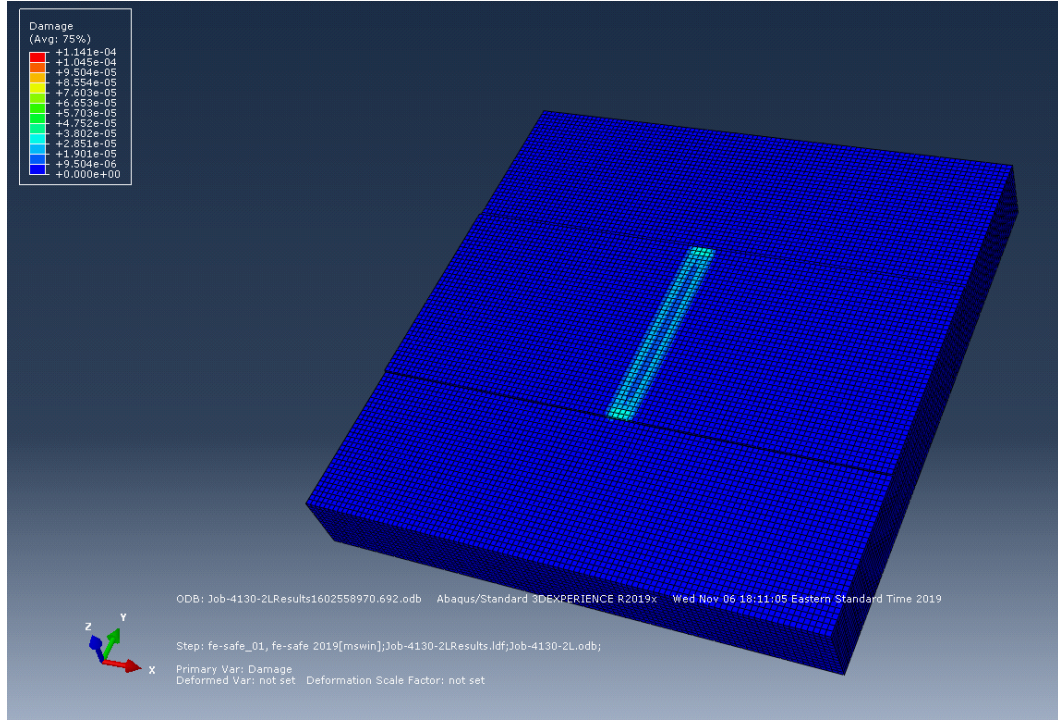
Figure 4.11: Fatigue damage map of the 2-layer UAM sample.

Case Study 2 with Varied Welding Speed

The welding speed is presumed to increase from 21.17 mm/s (50 inch/min) to 33.87 mm/s (80 inch/min) with other parameters unchanged. The number of cycles for each stress level is then changed to 1500. The predicted fatigue damage in UAM parts is summarized in Table 4.12 and Figure 4.14. The cracking of the 0th interface is expected to initiate after welding layer 31 instead of layer 10.

Case Study 3 with Varied Shear Force

In this case, the vibration amplitude is presumed to set higher, which leads to that the ultrasonic power input rises and the shear force applied by the transducers is increased from 3266 N to 4000 N. The maximum stress in the 0th interface while

Table 4.10: Fatigue damage for UAM build under experimental condition.

i	Damage per cycle of the worst point	No. of cycles	Damage from welding the ith layer	Cumulative damage
2	1.14×10^{-4}	2400	0.274	0.274
3	7.12×10^{-5}	2400	0.171	0.445
5	3.75×10^{-5}	2400	0.090	0.665
7	3.42×10^{-5}	2400	0.082	0.833
9	2.42×10^{-5}	2400	0.058	0.961
11	1.69×10^{-5}	2400	0.040	> 1

welding other layers is increased significantly. The FE calculations are summarized in Table 4.13 and Figure 4.15. The cracking of the the 0th interface is expected to initiate while welding layer 4 instead of welding layer 10.

4.2.4 Discussion

Computational analyses indicate that if other factors are kept the same and the weld quality of the 0th interface of UAM steel builds is improved, a taller crack-free build is possible to achieve. However, in practice, a higher weld quality does not necessarily guarantee a taller crack-free build. The reason is that a higher weld quality usually requires more aggressive parameters (higher amplitude and lower weld speed). A higher vibration amplitude setting leads to a higher ultrasonic power input and a higher shear load. Even though the weld is strong, aggressive parameters may lead to premature fatigue damage. The conclusion from the model is the need to achieve a strong enough weld with the least aggressive parameters, which leads to taller crack-free UAM steel builds.
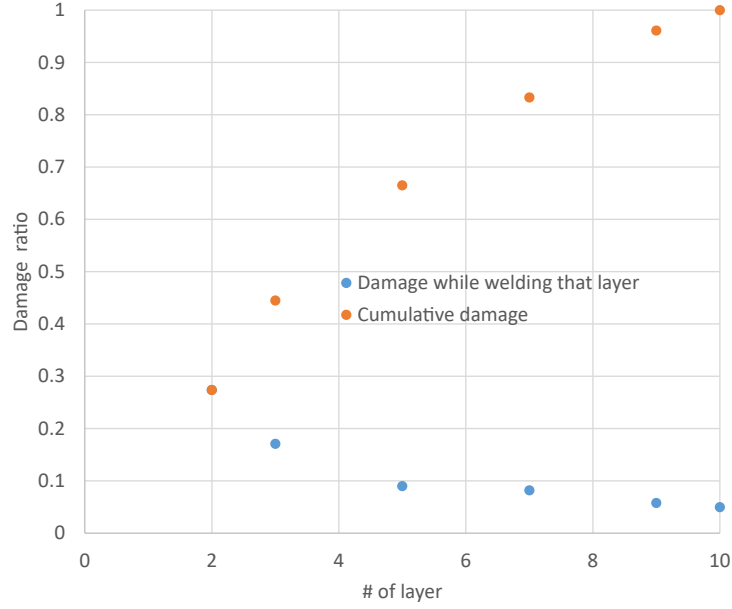
Figure 4.12: Fatigue damage plots for UAM build under experimental condition.

4.2.5   Summary

A numerical modeling approach for describing the stress distribution and predicting the fatigue performance of UAM steel builds has been developed. Using parameters from the experimental setup, the model predicts that the fatigue cracking of the interface between the baseplate and the first layer of foil occurs at welding the 10th layer of 4130 steel foils onto the build. The simulation agrees with the experimental observation, which validates the model. Multiple case studies were performed to explore the influence of different parameters on the fatigue damage in UAM builds. The results suggest that cracking during welding can be mitigated if the interface between the baseplate and the first layer of foil is formed using a relatively higher welding speed and lower power input and is achieved with a higher shear strength.

Table 4.11: Fatigue damage for case study 1 with varied shear strength.

i	Damage per cycle of the worst point	No. of cycles	Damage from welding the ith layer	Cumulative damage
2	3.92×10^{-4}	2400	0.094	0.094
3	2.35×10^{-5}	2400	0.056	0.220
5	1.16×10^{-5}	2400	0.026	0.248
7	1.07×10^{-5}	2400	0.017	0.291
9	7.10×10^{-6}	2400	0.011	0.330
11	4.59×10^{-6}	2400	0.007	0.355
15	3.01×10^{-6}	2400	0.006	0.391
20	2.55×10^{-6}	2400	0.007	0.424
30	2.94×10^{-6}	2400	0.006	0.489
40	2.59×10^{-6}	2400	0.006	0.554
60	2.60×10^{-6}	2400	0.006	0.674
80	2.60×10^{-6}	2400	0.006	0.794
114	2.66×10^{-6}	2400	0.006	> 1
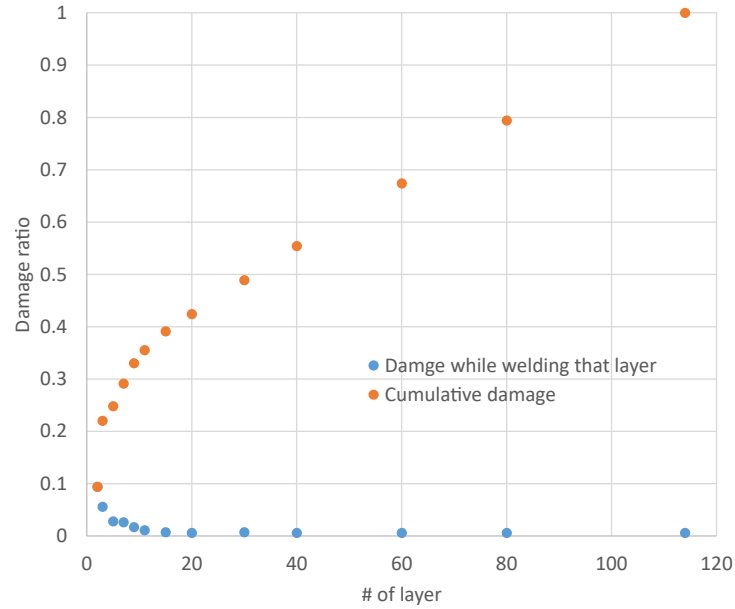
Figure 4.13: Fatigue damage plots for case study 1 with varied shear strength.

Table 4.12: Fatigue damage for case study 2 with varied welding speed.

i	Damage per cycle of the worst point	No. of cycles	Damage from welding the ith layer	Cumulative damage
2	1.14×10^{-4}	1500	0.171	0.171
3	7.12×10^{-5}	1500	0.107	0.278
5	3.75×10^{-5}	1500	0.056	0.415
7	3.42×10^{-5}	1500	0.051	0.519
9	2.42×10^{-5}	1500	0.036	0.599
11	1.69×10^{-5}	1500	0.025	0.655
15	1.21×10^{-5}	1500	0.018	0.742
20	1.07×10^{-5}	1500	0.016	0.827
30	1.18×10^{-5}	1500	0.018	0.997
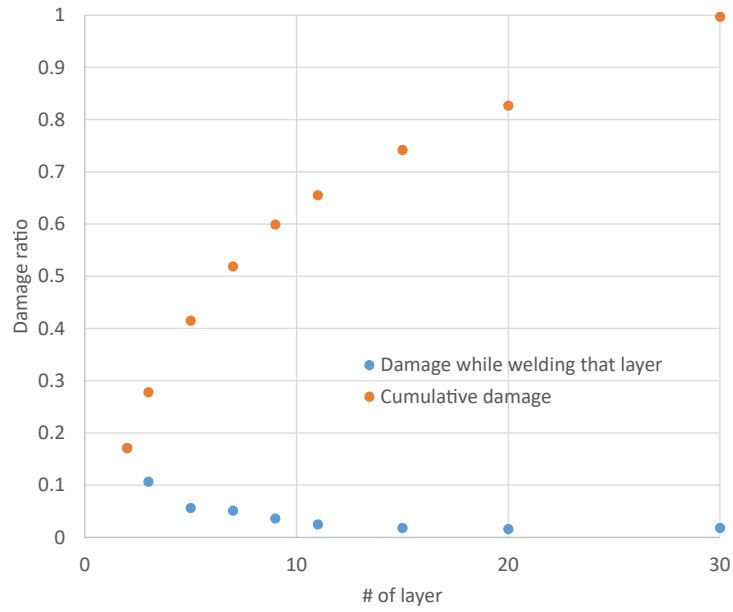
Figure 4.14: Fatigue damage plots for case study 2 with varied welding speed.

Table 4.13: Fatigue damage for case study 3 with varied shear force.

i	Damage per cycle of the worst point	No. of cycles	Damage from welding the ith layer	Cumulative damage
2	2.48×10^{-4}	2400	0.594	0.594
3	1.57×10^{-5}	2400	0.377	0.971
5	8.45×10^{-5}	2400	0.203	> 1
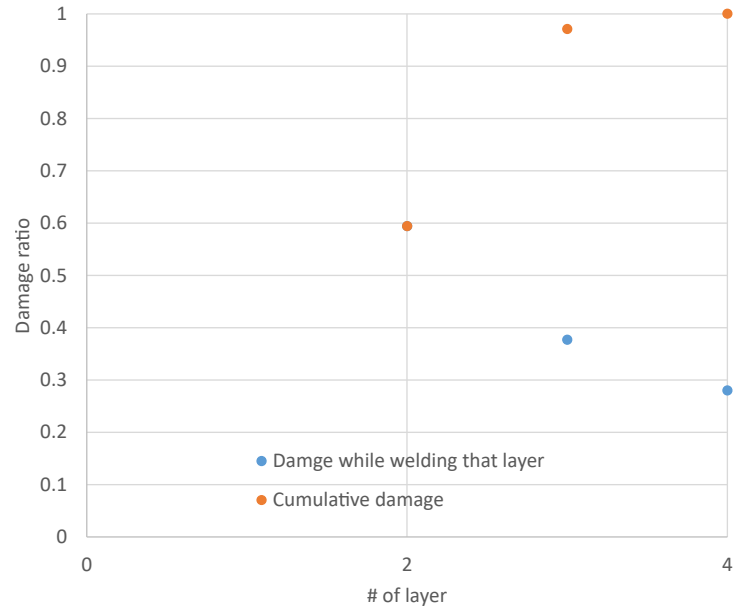
Figure 4.15: Fatigue damage plots for case study 3 with varied shear force.

Chapter 5

UAM Thermal Model

Overview

This chapter focuses on the development of an analytical UAM thermal model to predict the temperature profile during UAM welding of steels based on process parameters including vibration amplitude, welding speed, baseplate temperature, and normal force. Multiple case studies were conducted to investigate the effect of process parameters. The model predictions were then validated with thermocouple measurements.

5.1 Analytical Model Development

Previous chapters have demonstrated the feasibility of using UAM to print high strength steel parts. An increased power input, which leads to a higher interfacial temperature, is proved to produce robust UAM steel welds. Since the peak interfacial temperature is correlated with the weld quality, a UAM thermal model that predicts interfacial temperature based on weld parameters is desired and necessary to facilitate future UAM process design.

There is work in the literature on UAM thermal models for predicting temperature rise. Koellhoffer et al. proposed an analytical model to predict temperature rise and compared the model prediction with measured temperature [37]. However, the model is based purely on sliding friction. This is conflicting the most widely accepted understanding of the weld mechanism for UAM that both frictional sliding and plastic deformation occurs during welding [13, 44]. The ranges of parameters selected in this study are also limited and not representative of the UAM process. Ward et al. also developed an analytical model to predict the temperature profile during UAM that is based purely on frictional sliding [75]. In addition to involving conflicting assumptions, neither of these modeling approaches has been well validated by any experiments. Sriraman et al. used an analytical expression that is built based purely on plastic deformation to predict temperature rise and attempted to validate the predictions with measurements [70, 69]. However, the predictions are in poor agreement with the measurements.

In this study, an analytical model to predict the temperature profile during UAM welding of steels is developed based on the assumption that both frictional sliding and plastic deformation contribute to the temperature rise. The influence of different

process parameters on the peak temperature is calculated and discussed. Sixteen sets of parameters, which are given in Chapter 3, are implemented in the model to produce peak temperature predictions. These predictions are compared with measured temperatures to validate the model.

5.1.1 Sources of Heat

As introduced in previous chapters, during the UAM welding process, a rolling sonotrode is employed to apply ultrasonic (20 kHz) transverse vibrations and a normal force to metal foils. These combined motions lead to localized plastic deformation at the interface and form gapless metallurgical bonds. The normal force provides the intimate contact between foils. The transverse forces at the interface generate heat and form welds. Therefore, to model the heat generated during UAM welding, it is necessary to model the distribution of transverse forces at the UAM interface first. A linear time invariant (LTI) model from a previous study [29] is used to estimate shear force at the welding interface based on power input. As shown in Figure 5.1, sonotrode vibration velocity and transducer voltage are measured and used as inputs to the LTI model. Current is estimated from the measured weld power. For a certain UAM system, the shear force is linearly associated with the vibration amplitude:

$$F_s = c \times A \tag{5.1}$$

where F_s is the shear force, c is the shear force coefficient and calculated as 112.629 for the UAM system, and A is the vibration amplitude. The shear forces corresponding to the amplitudes used in this study are then calculated and shown in Table 5.1.

Table 5.1: Shear forces corresponding to the amplitudes used.

Amplitude A (μm)	Shear force F_s (N)
27	3041
28.5	3210
30	3379
31.5	3548
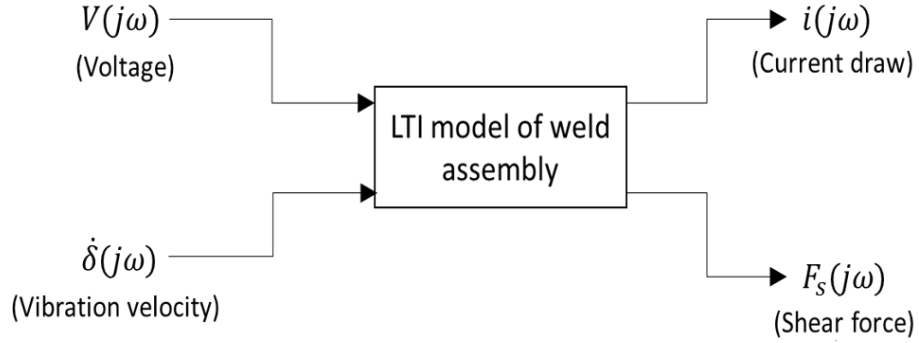
Figure 5.1: Schematic of LTI model framework [29].

5.1.2 Model Heat Generated from Frictional Sliding

After the shear force is obtained, a force partition coefficient γ will be selected based on experience. The friction force F_f is calculated from the following equation:

$$F_f = \gamma \times F_s \tag{5.2}$$

The classic Hertzian contact model is used to describe the frictional stress distribution at the welding interface. As shown in Figure 5.2, a coordinate system that moves with the sonotrode relative to the baseplate is defined such that the x direction is the

115
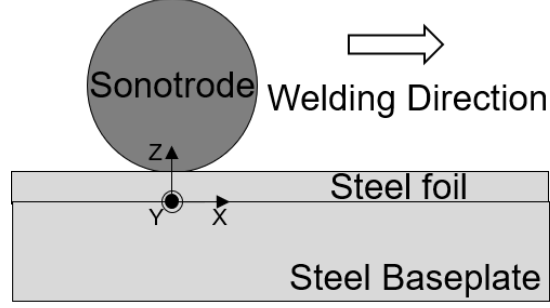
Figure 5.2: Moving coordinate system.

sonotrode rolling direction, y direction is the transducer vibration direction, and z direction is the normal force direction. In the case of UAM, where there is a contact between a cylinder and a flat surface, the stress distribution can be written as a function of x for the z=0 plane:

$$\sigma_f(x) = \begin{cases} 0 & \text{if } x < -b \\ \frac{2F_f}{\pi b w}\sqrt{1 - (\frac{x}{b})^2} & \text{if } -b < x < b \\ 0 & \text{if } x > b \end{cases} \tag{5.3}$$

where w is the width of the weld and b is the half width of contact area, which is defined as:

$$b = \sqrt{\frac{2F_n d}{\pi w E'}} \tag{5.4}$$

where d is the diameter of the sonotrode, and E' is the contact modulus of the two materials. It is defined as:

$$\frac{1}{E'} = \frac{1 - \nu_1^2}{E_1} + \frac{1 - \nu_2^2}{E_2} \tag{5.5}$$

where E_1 and E_2 are the elastic moduli and ν_1 and ν_2 are the Poisson's ratios of the two materials that are in contact.

In the case of UAM welding of steel, since the two materials are the same, the equation can be written as:

$$\frac{1}{E'} = \frac{2(1 - \nu^2)}{E} \tag{5.6}$$

Following the same structure as a recent study [75], the heat generated per unit time per unit area by friction is modeled as:

$$q_f = \sqrt{2} \times \pi \times \sigma_f \times \Omega \times A \tag{5.7}$$

where Ω is the vibration frequency and A is the vibration amplitude.

5.1.3 Model Heat Generation due to Plastic Deformation

Using the force partition coefficient introduced in the previous section, the transverse force that contributes to the plastic deformation is written as:

$$F_p = (1 - \gamma) \times F_s \tag{5.8}$$

Then, combined with normal force F_n applied by the sonotrode, the total force F_t that contributes to the plastic deformation is obtained as:

$$F_t = \sqrt{F_n^2 + F_p^2} \tag{5.9}$$

Assuming that if the stress caused by the total force is higher than the yield stress at a point, then the stress is equal to the yield strength σ_y of the material:

$$\sigma_p(x) = \begin{cases} 0 & \text{if } x < -b' \\ \sigma_y & \text{if } -b' < x < b' \\ 0 & \text{if } x > b' \end{cases} \tag{5.10}$$

The boundary of the plastically deformed region b' is calculated as a function of b using the following equation:
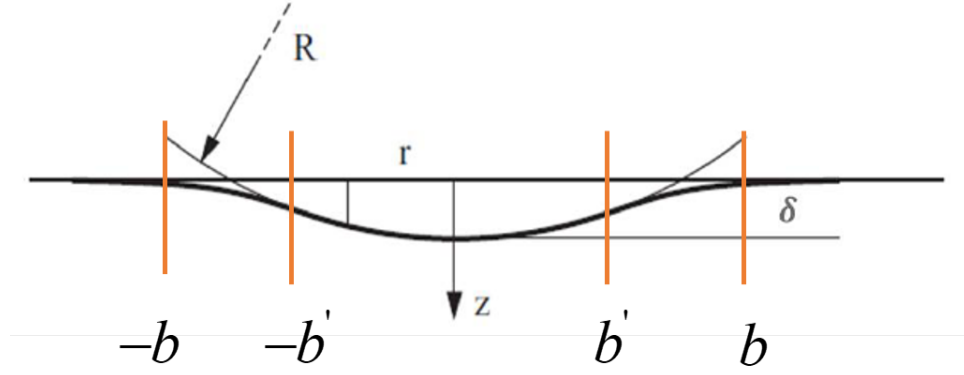
Figure 5.3: Schematic of boundary of the plastic deformed region

$$b' = b \times \sqrt{1 - (\frac{\sigma_y \pi b w}{2 F_t})^2} \tag{5.11}$$

The relationship between the b' and b is shown in the Figure 5.3.

The heat generated per unit time and per unit area by plastic deformation is modeled in a similar form as the heat generated by friction:

$$q_p = \beta \times \sigma_p \times (\epsilon - \epsilon_y) \times t \times \Omega \tag{5.12}$$

where β is the heat conversion coefficient describing the percentage of heat produced by plastic deformation, ϵ is the failure strain, which is characterized using tensile testing, ϵ_y is the yield strain, and t is the thickness of deformed interfaces, which is measured using EBSD and nanoindentation tests.

5.1.4 UAM Thermal Model

The shape of the heat source is recognized as a band, with a width of $2b$ for the heat flux due to friction and $2b'$ for the heat flux due to plastic deformation. A quasi-steady state temperature rise solution obtained by Jaeger [35, 48] in the form of a

dimensionless expression is used to simulate the interface temperature profile:

$$\theta(X, Y, Z) = \int_{X+B}^{X-B} e^{-m} K_0 (Z^2 + m^2)^{\frac{1}{2}} dm \tag{5.13}$$

Here, K_0 is the modified Bessel function of the second kind of order zero and the dimensionless parameters are defined as:

$$\theta = \frac{\pi K v \Delta T}{2q\kappa}, B = \frac{vb}{2\kappa}, X = \frac{vx}{2\kappa}, Y = \frac{vy}{2\kappa}, Z = \frac{vz}{2\kappa} \tag{5.14}$$

where K is the thermal conductivity, κ is the thermal diffusivity, ΔT is the temperature rise, v is the welding speed, and q is the heat flux at the interface.

The convective heat loss to the environment is ignored to simplify the model. However, the heat loss through the sonotrode, as introduced in the work of Ward et al. [75], is included in the model . A heat partition coefficient α is calculated using:

$$\alpha = \frac{K_b}{K_b + \sqrt{\frac{\kappa_b}{\kappa_s}} K_s} \tag{5.15}$$

where K_b is the thermal conductivity and κ_b is the thermal diffusivity of the UAM build material, which is carbon steel 4130, and K_s is the thermal conductivity and κ_s is the thermal diffusivity of the sonotrode material, which is Stellite alloy in this study.

Combining the moving band solution with heat flux equations derived earlier, the temperature rise due to frictional sliding is given as:

$$\Delta T_f = \int_{-b}^{b} \frac{\alpha q_f}{\pi K_b} \times e^{\frac{-v(x_0 - vt - x)}{2\kappa_b}} K_0 \left(\frac{v \sqrt{(x_0 - vt - x)^2 + z^2}}{2\kappa_b} \right) dx' \tag{5.16}$$

The temperature rise due to plastic deformation is given as:

$$\Delta T_p = \int_{-b'}^{b'} \frac{\alpha \beta q_p}{\pi K_b} \times e^{\frac{-v(x_0 - vt - x)}{2\kappa_b}} K_0 \left(\frac{v \sqrt{(x_0 - vt - x)^2 + z^2}}{2\kappa_b} \right) dx' \tag{5.17}$$

119

Combining these two equations, the interfaical temperature profile for UAM welding
is written as:

$$
\begin{aligned}
T = T_0 &+ \int_{-b}^{b} \frac{\alpha q_f}{\pi K_b} \times e^{\frac{-v(x_0 - vt - x)}{2\kappa_b}} K_0\left(\frac{v\sqrt{(x_0 - vt - x)^2 + z^2}}{2\kappa_b}\right) dx' \\
&+ \int_{-b'}^{b'} \frac{\alpha \beta q_p}{\pi K_b} \times e^{\frac{-v(x_0 - vt - x)}{2\kappa_b}} K_0\left(\frac{v\sqrt{(x_0 - vt - x)^2 + z^2}}{2\kappa_b}\right) dx'
\end{aligned}
\tag{5.18}
$$

where T is the interfacial temperature and T_0 is the baseplate temperature. The
processing conditions and material properties of welding UAM 4130 reported in the
prior chapters were used to define the model, as shown in Table 5.2.

Table 5.2: System and material constants used in this study.

Symbol	Meaning	Value
d	Sonotrode diameter	0.0955 m
w	Welding width of the sonotrode	0.01524 m
E	Elastic modulus of the build material (carbon steel 4130)	205 GPa
ν	Poisson's ratio of the build material (carbon steel 4130)	0.29
Ω	Vibration frequency	20000 Hz
β	Heat conversion coefficient	0.83
ϵ	Failure strain of the build material (carbon steel 4130)	0.08
ϵ_y	Yield strain of the build material (carbon steel 4130)	0.004
t	Thickness of the deformed region	2×10^{-5} m
K_b	Thermal conductivity of the build material (carbon steel 4130)	42.7 W/mK
κ_b	Thermal diffusivity of the build material (carbon steel 4130)	1.14×10^{-5} m^2/s
K_s	Thermal conductivity of the sonotrode (Stellite 6)	14.85 W/mK
κ_s	Thermal diffusivity of the sonotrode (Stellite 6)	1.20×10^{-5} m^2/s
α	Heat partition coefficient	0.747

5.2   Computational Studies

In order to develop a fundamental understanding of the effect of different parameters on the temperature rise during UAM steel welding, multiple computational studies were developed and performed. Key model parameters including the force partition coefficient γ and process parameters including vibration amplitude A, welding speed v, normal force F_n, and baseplate temperature T_0 were studied.

121

5.2.1 Temperature Profile and Temperature Field of a Typical UAM 4130 Steel Weld

Force partition coefficient γ is the most important parameter that need to be determined based on experience. The expectation is that certain values of the force partition coefficient would work for most conditions in processing certain material such as carbon steel 4130. Other parameters are selected from PS3 of the design of experiments study introduced in Chapter 3, as shown in Table 5.3. Two extreme cases were first performed. Assuming that the shear force is all used for plastic deformation and $\gamma = 0$, the temperature profile of this pure plastic deformation case is shown in Figure 5.4(a). Assuming that the shear force is all used for friction and $\gamma = 1$, the temperature profile of this pure friction case is shown in Figure 5.4(b). As seen from the plots, the pure friction case gives an estimate of a peak temperature of about 7000 K. By comparison, the pure plastic deformation case generates an estimate of a peak temperature of about 395 K. These results indicate that the value of γ should be smaller than 0.1 to give an reasonable estimate.

Table 5.3: Weld parameter set 3 (PS3) from the DOE study.

Parameter	Level
Baseplate temperature	100 °F (310.93 K)
Amplitude	30.03 μm
Welding speed	80 in/min (33.87 mm/s)
Normal force	6000 N
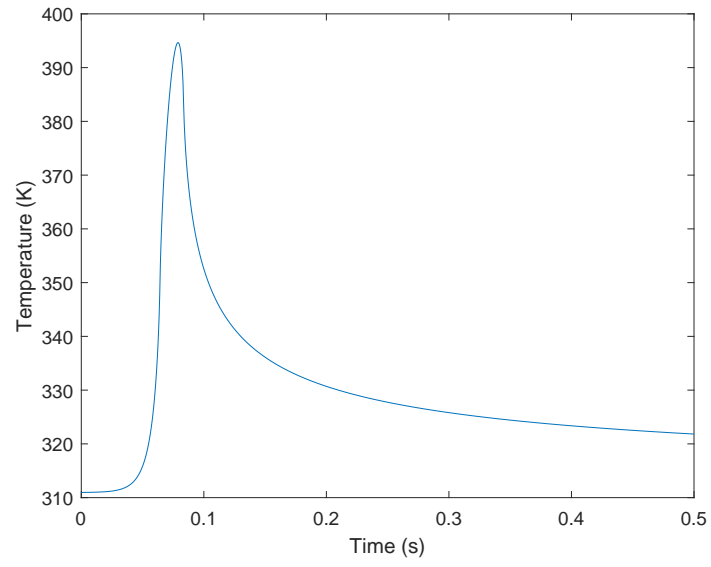
(a)
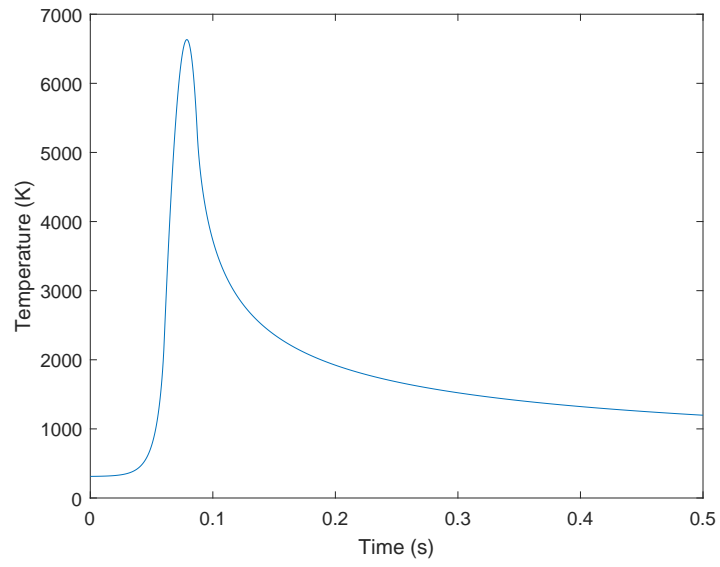
(b)

Figure 5.4: Predicted temperature profile for (a) pure plastic deformation with $\gamma = 0$ and (b) pure friction with $\gamma = 1$ condition.

After a trial and error process, $\gamma = 0.075$ was selected. The predicted temperature profile of this parameter combination is shown in Figure 5.5. Overall, the profile matches the thermocouple measured profile, as shown in Figure. 3.4 of Chapter 3. The temperature gradually increases at the beginning of the measurement, when the heat sources applied by the sonotrode approaches the probed location. After the heat sources reaches right above the probed location, the temperature sharply increases and reaches its peak in milliseconds. Finally, the temperature decreases gradually after the heat sources pass the probed location and the heat is absorbed into the UAM build.

A two dimensional temperature contour plot is also obtained with the same parameter settings. This temperature distribution field in the x-z plane during UAM welding of 4130 steel is shown in Figure 5.6. The thickness of each layer of steel foil is 1.27×10^{-4} m. The approximate interface locations are indicated by dashed lines. As presented in the contour plot, the majority of the heat affected area (reaching 90% of the peak temperature) stays in the foil right beneath the welding interface.

5.2.2 Computational Case Studies

In this section, one of the process parameters was varied and investigated with $\gamma = 0.075$ and other process parameters fixed as PS3 shown in Table 5.3. The levels for each parameter are selected from the DOE study, which is introduced in Chapter 3.

Examining Welding Speeds

The welding speed was varied from 60 in/min to 80 in/min and 100 in/min. The predicted temperature profile is shown in Figure 5.7. The profile and peak temperature are different for varying welding speeds. The temperature increases slower with
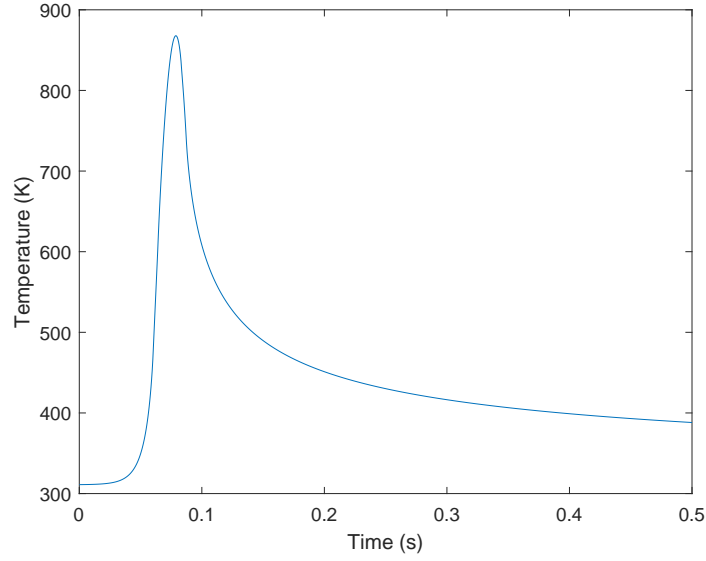
Figure 5.5: Predicted temperature profile with $\gamma = 0.075$.

the lower welding speed at the start of the temperature rise. These simulations also indicate that lower welding speed generates higher peak temperature. This trend is the same as the experiments, as shown in the main effect plot in Figure 3.6 of the DOE study.

Examining Vibration Amplitudes

The vibration amplitude is examined at 28.5 μm, 30 μm, and 31.5 μm. As shown in Figure 5.8, the temperature profiles are the same for all three cases at the start.
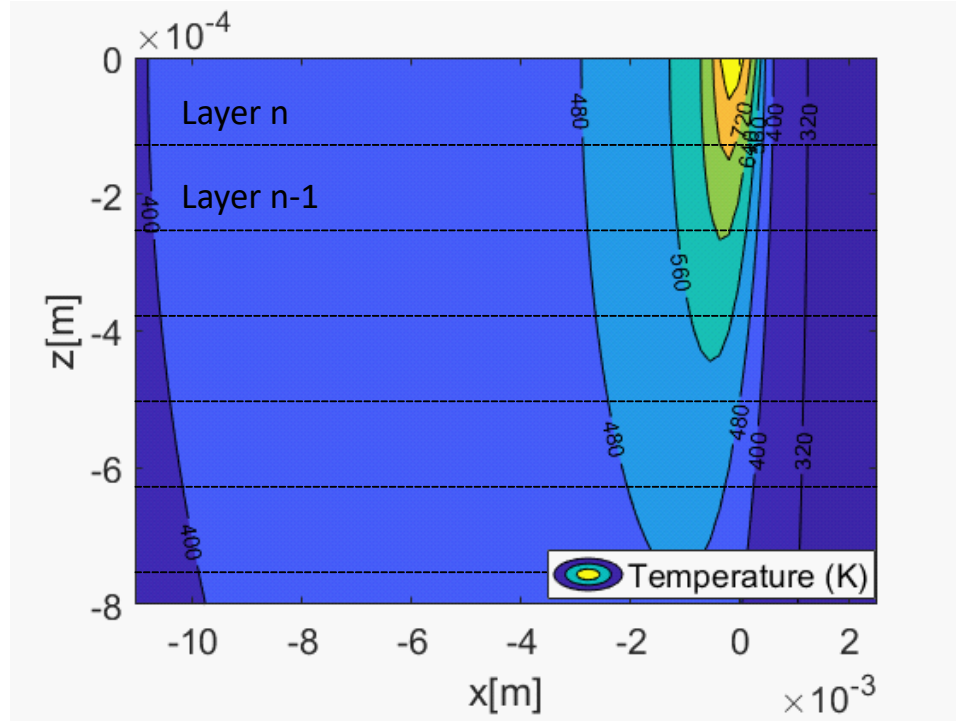
Figure 5.6: Predicted temperature contour plot of the x-z plane.

Higher amplitude generates higher peak temperature, which also agrees with the overall trend of the main effect plot in Figure 3.6.

Examining Normal Forces

The normal force is varied from 4000 N to 5000 N and 6000 N. The corresponding temperature profiles are shown in Figure 5.9. The majority of the temperature profiles are the same for these cases. Lower normal force generates higher peak temperature, which is consistent with the conclusion from the DOE study. It also worth noting that the peak temperature differences caused by these normal force changes are relatively low compared to the changes of amplitude and welding speed.
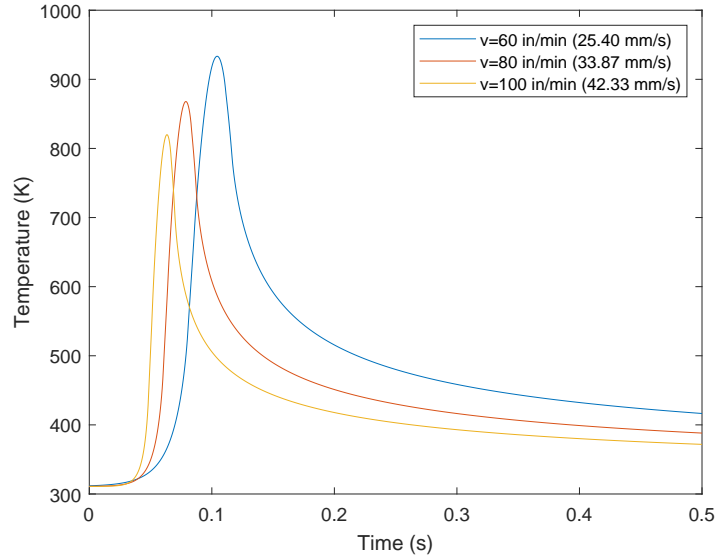
Figure 5.7: Predicted temperature profile with varied welding speed.

Examining Baseplate Temperatures

The baseplate temperature is varied from 310.95 K to 366.48 K and 422.04 K. The shape of the temperature profiles and the amount of temperature rise are nearly the same for these cases, as shown in Figure 5.10. The only difference is the starting point of the curves.
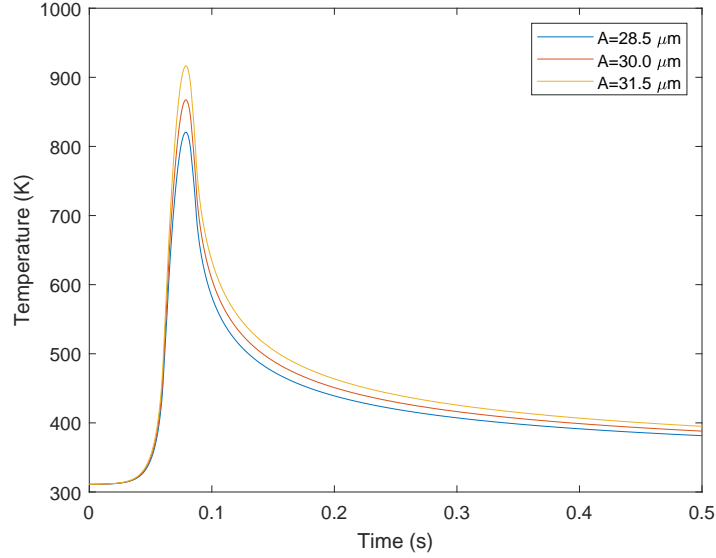
Figure 5.8: Predicted temperature profile with varied vibration amplitude.

5.3   Experimental Validation

The predicted temperature profile for PS3 is compared to measured profiles from the DOE study and $\gamma = 0.075$ is used. As shown in Figure 5.11, the predicted peak temperature is close to the measured values. The shape of the predicted temperature profile is also very similar to the measured profiles. However, the predicted temperature profile is sharper than the measured profiles. The interfacial temperature is predicted to reach the peak in less than 0.1 s during the temperature rise period, while the measured data shows that it takes about 0.25 s. This difference could be caused by experimental or computational imperfections. The measured temperature
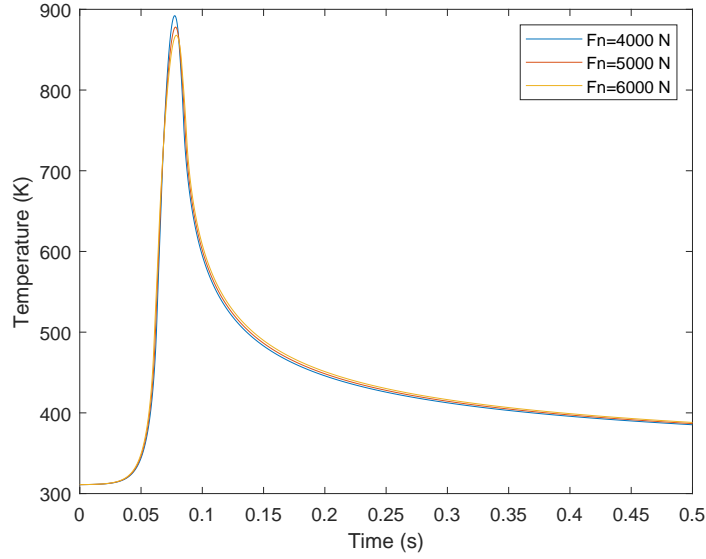
Figure 5.9: Predicted temperature profile with varied normal force.

was collected using a Type K AWG 40 thermocouple (0.080 mm tip diameter). Since the response time of the thermocouple mainly depends on the tip diameter, a thermocouple with a smaller diameter will response faster and provide a more accurate measurement of the "true" temperature profile, which will be sharper than the current measurement. The current thermal model incorporates the assumption that heat is only lost through the sonotrode to simplify the model. Considering the heat loss to the environment would make the predicted temperature rise slower, which would be more similar to the measured profiles.
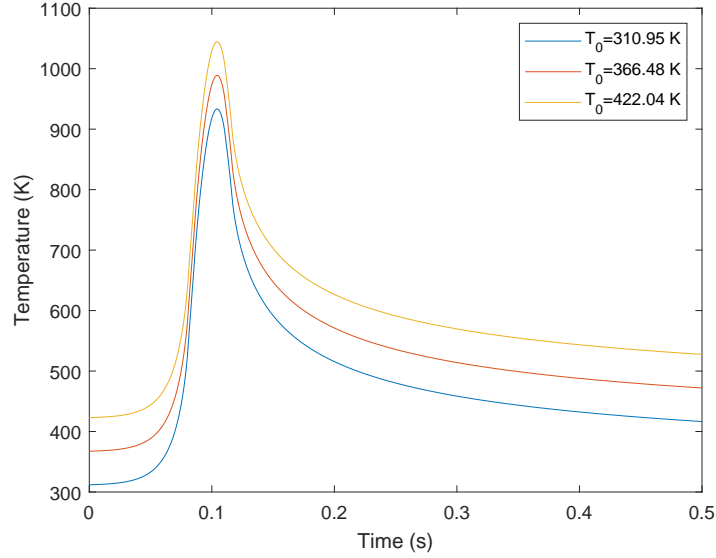
Figure 5.10: Predicted temperature profile with varied baseplate temperature.

Even though the simulation of the temperature profile helps to understand the contribution from each heat source to the temperature rise during welding, it is not directly related to the weld quality. As concluded from the DOE study, the peak temperature instead can be correlated the weld strength. Thus, the focus of the following study is to validate the model predicted peak temperatures with experiments. The process parameters used to define the model are selected from the DOE study, as shown in Table 3.1 and Table 3.2. The measured peak temperatures are summarized in Table 5.4. Even though the process parameters are the same for each parameter set (PS), variations in peak temperature measurements caused by the material and the machine are observed. To better represent the predictions, a simulated range

130
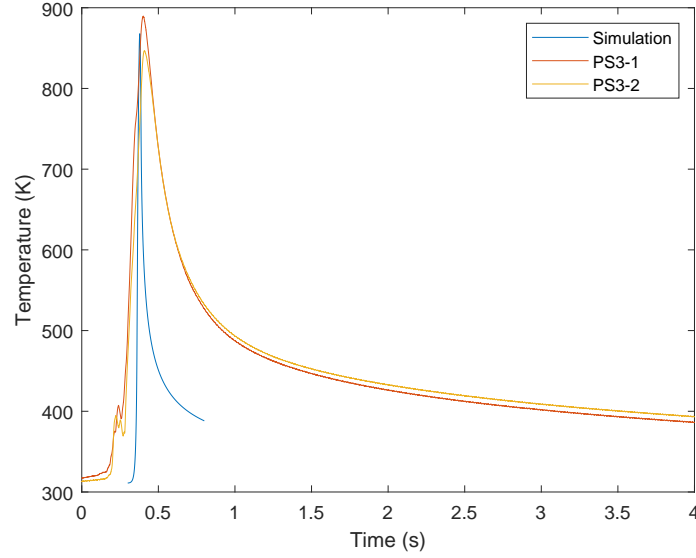
Figure 5.11: Simulated temperature profile compared to the measured profiles for PS3 from the DOE study.

instead of a predicted average peak temperature is obtained for each PS. The expectation is that all measurements should fall into this UAM thermal model simulated range. The force partition factors γ for predicting the lower and higher threshold of the simulated range are needed.

After trial and error, $\gamma = 0.068$ is used to define the lower threshold and $\gamma = 0.094$ is selected for the higher threshold for low baseplate temperature cases where $T_0 = 310.95$ K or $T_0 = 366.45$ K. The material properties are kept the same for the model. However, most of the material properties are temperature dependent. To compensate for the variation caused by the constant material properties, $\gamma = 0.050$ is utilized

Table 5.4: Measured peak interfacial temperature from the DOE study.

Parameter set	Peak temperature measurement 1 (K)	Peak temperature measurement 2 (K)
PS1	1007	993
PS2	985	1011
PS3	847	889
PS4	903	845
PS5	755	709
PS6	1132	1112
PS7	908	928
PS8	977	975
PS9	821	820
PS10	719	769
PS11	968	978
PS12	1060	1120
PS13	714	685
PS14	1047	956
PS15	1117	993
PS16	1194	1151

to define the lower threshold and $\gamma = 0.078$ is selected for the higher threshold for high baseplate temperature cases where $T_0 = 422.05$ K or $T_0 = 477.55$ K. After γ was selected, sixteen sets of simulations were performed. As shown in Figure 5.12, 26 out of 32 measured peak interface temperatures fall into the range predicted by the UAM thermal model. The 6 out-of-range measurements may be caused by the experimental variability. Further improvement of the thermocouple measurement process or development of the model to take the variations into account is needed.
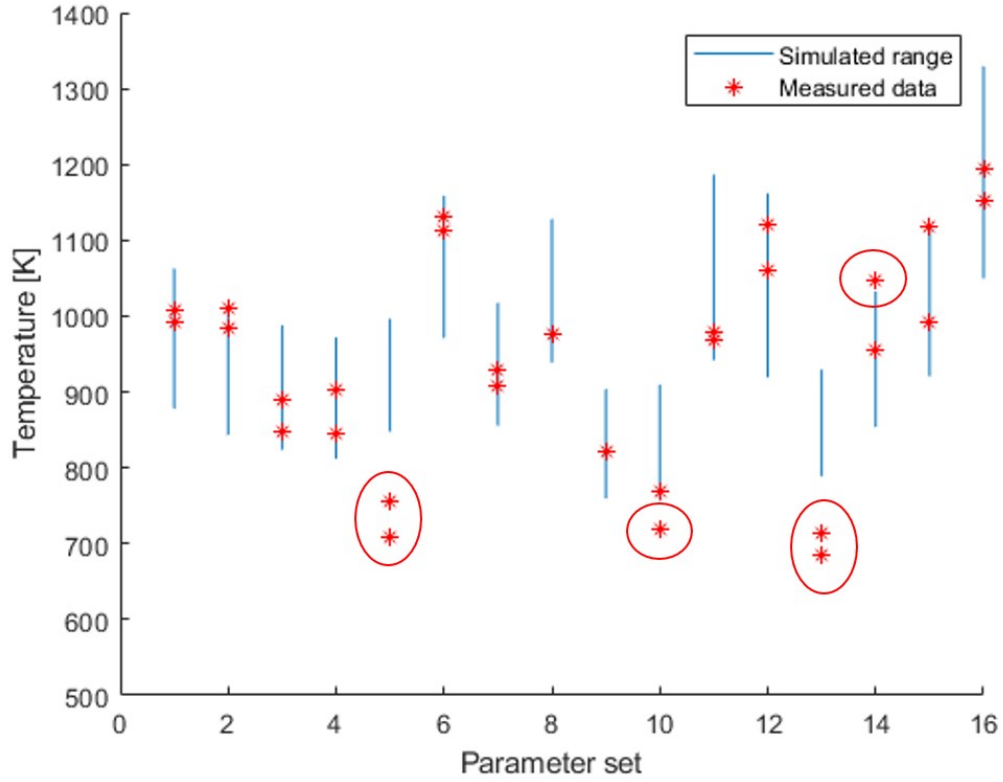
Figure 5.12: Simulated temperature ranges compared to the measured peak temperatures from the DOE study. Measurements that fall out of the simulated range are marked with red circles.

Considering the complexity of the UAM process, the overall agreement between model predictions and experimental results validates the UAM thermal model. Even though carbon steel 4130 is used in this study, the concept and structure of the UAM thermal model can be easily expanded to other material systems in the future.

5.4 Summary

A UAM thermal model describing heat generation from frictional sliding and plastic deformation during the UAM welding process is developed. The frictional sliding is demonstrated to contribute to most of the temperature rise. A two dimensional temperature field plot is simulated. The plot shows that the majority of the heat affected area (reaching at least 90% of the peak temperature) stays in the foil right underneath the welding interface. Multiple computational case studies have indicated that a decrease in welding speed, an increase in vibration amplitude, a decrease in normal force, or an increase in baseplate temperature would result in an increase in the peak temperature. These findings are consistent with the conclusion of the DOE study introduced in Chapter 3. The shape of the simulated temperature profile is found to be comparable to the measured profiles. Measured peak temperatures are also compared to the model simulated peak temperature range. Overall, 26 out of 32 measured peak temperatures fall within the UAM thermal model predicted range. Considering the complexity of the UAM process, this overall agreement between model predictions and experimental results validates the UAM thermal model.

Chapter 6

Conclusions and Future Work

6.1   Summary

A custom shear test method was designed to characterize the shear strength of a specific interface of UAM builds. The shear test method was validated with solid Al 6061 T6. The shape and dimensions of the shear sample are optimized through experiments and FE modelings. A stepped shape is selected for future testing of UAM samples due to its better accuracy. This shear test method is then used to measure the shear strength of UAM steel builds in this thesis. Stainless steel 410 was made using UAM. Increasing the baseplate temperature from 38 °C to 204 °C and applying post-treatment HIP provide a significant increase in shear strength. Post-shear fracture surface analyses show that as-welded/204 °C samples have larger ductile failure areas than as-welded/38 °C samples, which suggests that higher baseplate temperature promotes metallurgical bonding. A similar fracture study on HIP samples show that HIP further promotes metallurgical bonding. A pearlite layer is found between the baseplate and the first layer of SS 410 foil after HIP treatment. DICTRA simulations indicate that the pearlite layer occurs as an outcome of uphill carbon diffusion at the interface.   HIP treatment is shown to increase the overall hardness of UAM

SS 410 from 204±7 HV to 240±16 HV due to the formation of local martensite. Nanohardness tests show that the top of layer n is harder than the bottom of layer n+1. The increase in hardness at the interface is primarily due to grain boundary strengthening. In the second study, the effect of increased weld power on the shear strength of as-welded UAM steel 4130 was investigated.

An increased power of 2695 W/m² was applied to make the UAM steel build using a cobalt-chromium coated sonotrode. An average shear strength of 549 MPa is achieved in the UAM 4130 builds, which is comparable to that of bulk 4130 material. This represents a 195% increase over the shear strength of 186 MPa for samples fabricated using 2066 W/m² with an uncoated steel sonotrode without HIP. A peak temperature of 855 °C was measured at the welding interface using a thermocouple measurement method, which suggests significant softening of the material. This softening and increased plastic deformation caused by higher power input are speculated as the cause of the weld quality improvement. Even though the peak interfacial temperature is beyond the upper critical temperature (Ac3) of 801 °C for 4130 steel, a fully martensitic structure is not observed at the interface between the baseplate and the first layer of foil. This is attributed to an increase in critical temperatures due to the high heating rate (>400 °C/s) during UAM welding of steels.

Weld parameters for making UAM 4130 builds were optimized via a design of experiments study. The following combination of process parameters is identified to generate the highest shear strength within the selected process window: a baseplate temperature of 400 °F (204.4 °C), an amplitude of 31.5 μm, a welding speed of 40 in/min (16.93 mm/s), and a normal force of 6000 N. The influence of weld parameters including baseplate temperature, amplitude, welding speed, and normal force

on the interfacial temperature and shear strength was also investigated. Analysis of variance and main effect plots show that normal force, amplitude, and welding speed are significant for interfacial temperature. Similar analyses show that normal force and amplitude have a statistically significant effect on shear strength. The Pearson correlation coefficient is calculated as 0.227, which indicates a weak positive correlation between interfacial temperature and shear strength. These analyses reveal that the shear strength can be treated as a strong indicator of the weld quality, and that the interfacial temperature is a relatively weak indicator.

Residual stresses in UAM 4130 samples were measured using neutron diffraction for the first time. The aggregating pattern and residual stress distribution in UAM 4130 were computed and reported. Unlike the large tensile residual stress found in fusion-based additive manufactured steels, the maximum tensile residual stress for UAM 4130 is found to be relatively low at 176.5 MPa. This analysis indicates potentially better fatigue performance for as-printed UAM material compared with fusion-based AM material. For the same build height, residual stresses in UAM 4130 are found to reach a maximum near the end of the rolling direction in most of the cases.

FE models for describing the stress distribution and predicting the fatigue performance of UAM steel builds were developed. Under a typical UAM steel welding setup, the model predicts that fatigue cracking of the interface between the baseplate and the first layer of foil occurs while welding the 10th layer of 4130 steel foil onto the build. This prediction is consistent with the experimental observation, which validates the model. Furthermore, computational case studies were conducted to examine the effect of parameters on the fatigue damage in UAM builds. These analyses

indicate that a taller crack-free UAM steel build can be made if the interface between the baseplate and the first layer of foil is formed with a higher shear strength using a relatively higher welding speed and lower ultrasonic power input.

A UAM thermal model simulating the temperature rise due to heat generation from frictional sliding and plastic deformation during UAM welding process is developed. The frictional sliding is shown to contribute to the majority of the temperature rise. The two dimensional temperature map shows that the majority of the heat affected area (reaching 90% of the peak temperature) stays in the foil right beneath the welding interface. Computational case studies suggest that a decrease in welding speed, an increase in vibration amplitude, a decrease in normal force, or an increase in baseplate temperature would lead to an increase in the peak temperature. These findings are consistent with the conclusions of the DOE study. The simulated temperature profile is similar to the measured profiles. Overall, 26 out of 32 measured peak temperature falls into the UAM thermal model predicted range. This overall agreement between model predictions and experimental results validates the UAM thermal model.

6.2   Contributions

1. **Demonstrated methods to achieve robust UAM steel welds with high shear strength**

   - Increasing the baseplate temperature from 38 °C to 204 °C is proven to improve the weld quality of UAM SS 410

   - Post-treatment HIP further improves the shear strength of UAM SS 410 to be comparable to that of bulk 410 material

- An increased power applied with a cobalt-chromium coated sonotrode achieved UAM 4130 build with a shear strength that is comparable to that of bulk 4130 material

2. **Developed and validated a custom shear test method to characterize the mechanical strength of UAM samples**

   - Performed experiments to determine the optimal shape and dimensions of the shear sample

   - Built a FE model to understand the influence of different sample shapes on the shear test results

3. **Analyzed and modeled the fatigue behavior during UAM welding of steel**

   - Quantified the residual stress in UAM 4130 steel samples via neutron diffraction for the first time

   - Developed and validated a numerical model that describes the stress distribution in the workpiece and predicts fatigue performance during UAM welding of steels to aid design of welding parameters to mitigate cracking

   - Multiple computational case studies suggest that a taller crack-free UAM steel sample can be built if a higher shear strength at the interface between the baseplate and the first layer of foil can be achieved with a higher welding speed and lower power input

4. **Determined optimal process parameters for UAM steel 4130**

   - Investigated the effects of process parameters including vibration amplitude, welding speed, normal force, and baseplate temperature on the shear strength and interfacial temperature of UAM welding of steels

   - Studied statistical relationship between the interfacial temperature and shear strength of UAM steel 4130

   - Identified the optimal combination of process parameters to generate the highest shear strength within the selected process window

5. **Developed a UAM thermal model that combines heat generation due to friction and due to plastic deformation to predict interfacial temperature rise at the weld interfaces based on welding parameters and material properties**

   - Validated the model by comparing the simulations with the experimentally measured temperatures from the DOE study

   - Performed multiple computational case studies to investigate the effect of process parameters on interfacial temperature changes. The results suggest that a decrease in welding speed, an increase in vibration amplitude, a decrease in normal force, or an increase in baseplate temperature would result in an increase in the peak temperature.

6.3 Future Work

Even though this study significantly extends the fundamental understanding of the structure-property-process relationship of UAM steel welding, more research is needed

to fully realize the potential of UAM. AISI stainless steel 410 and AISI carbon steel 4130 were used as the material platform in this thesis. Using the understanding developed in this work to expand the design envelope into other steels and high strength materials is desired. The possibilities of expanding the design envelope of UAM will make this technology more attractive to automotive, aerospace, and other industries.

Increased weld power was demonstrated to improve the mechanical strength of as-welded UAM steel. A cobalt-chromium coated sonotrode was developed by UTK to increase the galling threshold and allow a higher power input, which led to a 195% improvement in the shear strength. However, the current upper limit of the power input without creating any galling damage represents 60% of the power capacity of the Fabrisonic 400 UAM machine. Further improvement in the design of the coated sonotrode is needed to fully realize the capability of UAM and expand the design envelope into stronger materials.

Residual stress formed in UAM steel 4130 during welding was measured using neutron diffraction for the first time. The aggregating pattern of residual stress as the build height increases was investigated. However, the relationship between the process parameters and the residual stress is unknown and needs further exploration. A design of experiment study is desired for this research. Since neutron diffraction is the only viable technique to do nondestructive high-resolution measurement of residual stress in UAM samples, it should continue to be used.

A UAM fatigue model was developed in this thesis to predict fatigue cracking behavior at the interface between the baseplate and the first layer of foils (0th interface). The model was validated with experimental observation. However, the model

makes a conservative estimate of the fatigue cracking using maximum stress at the 0th interface for welding different layers of foils. The fatigue process has a degree of randomness, which is not reflected by the current model. Including stochastic features into the current UAM fatigue model is necessary to further improve the model predication accuracy. There is evidence that UAM 4130 foil welded on A36 baseplate has a stronger interface between the baseplate and the first layer of foil than UAM 4130 foil welded on 4130 baseplate. Cracking also initiates at a later stage for UAM 4130 builds welded on A36 baseplate. However, causes for this phenomenon need to be investigated through microstructural analysis and modeling.

A UAM thermal model that describes heat generation from frictional sliding and plastic deformation during UAM welding process was developed. 26 out of 32 measured peak temperature falls into the UAM thermal model predicted range. This overall agreement between simulations and thermocouple measurements validates the UAM thermal model. To simplify the model, it is presumed that every location at the welding interface experiences the same temperature history. However, variations in measured temperature at different x and y positions were observed. To further improve the model prediction accuracy and capture the temperature difference in x and y, more thermal model development is necessary. Currently, the determination of the partition coefficient γ is done through a manual trial and error process. Instead, select the γ using least squares regression through a numerical tool would also help to improve the model prediction accuracy.

Prior to this work, most of the understanding of UAM welding of steels was developed based on experiments. This work has presented statistical, numerical, and analytical modeling efforts to understand and predict the fatigue behavior and the

temperature profile during welding. The peak temperature is proved to be a weak indicator of the weld quality. However, a direct connection between the weld quality and process parameters was not built. A model to predict the weld strength of UAM build based on parameters is needed to aid future process design.

Appendix A

Raw SEM Images of Fracture Surface of UAM SS410 Samples
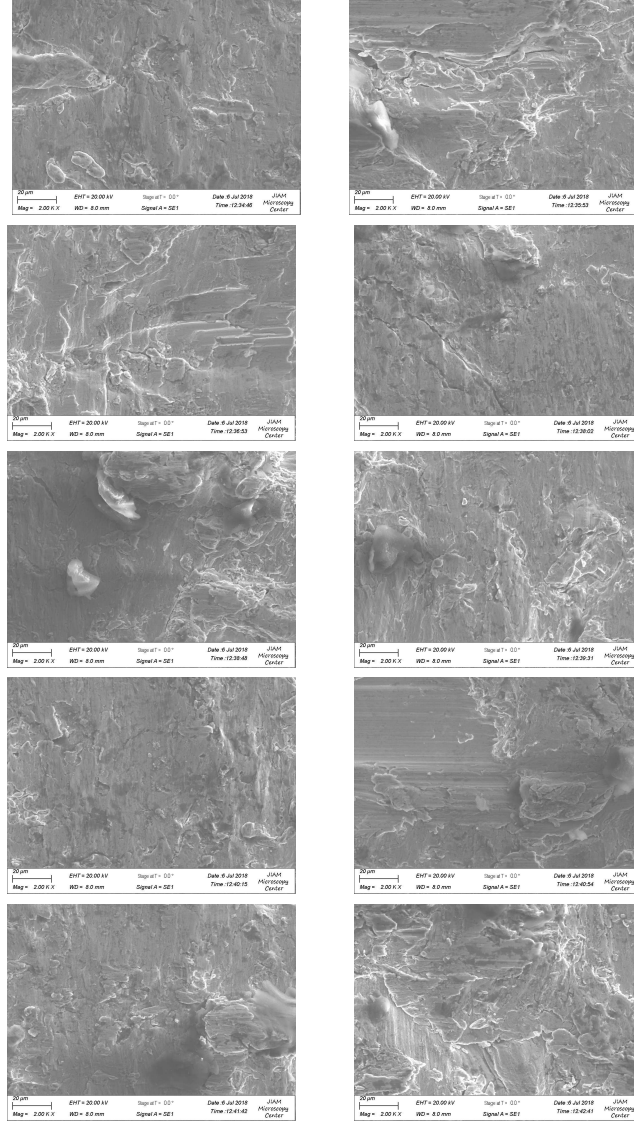
Figure A.1:   SEM images at ten random locations on the fracture surface for an as-welded/38°C UAM SS410 sample.
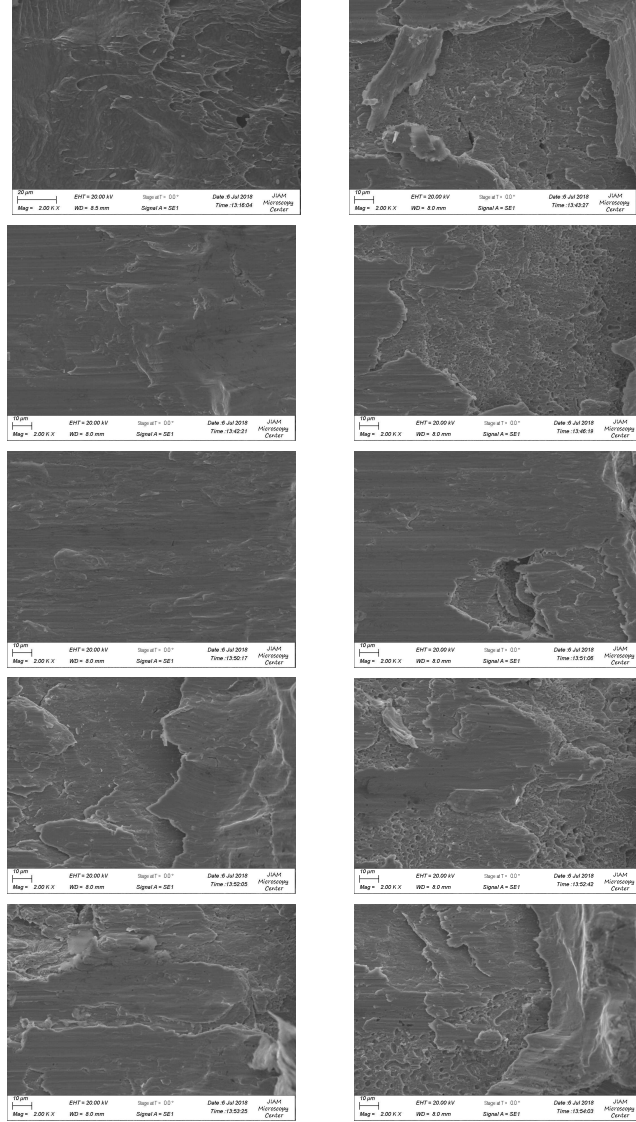
Figure A.2:   SEM images at ten random locations on the fracture surface for a HIP/38°C UAM SS410 sample.
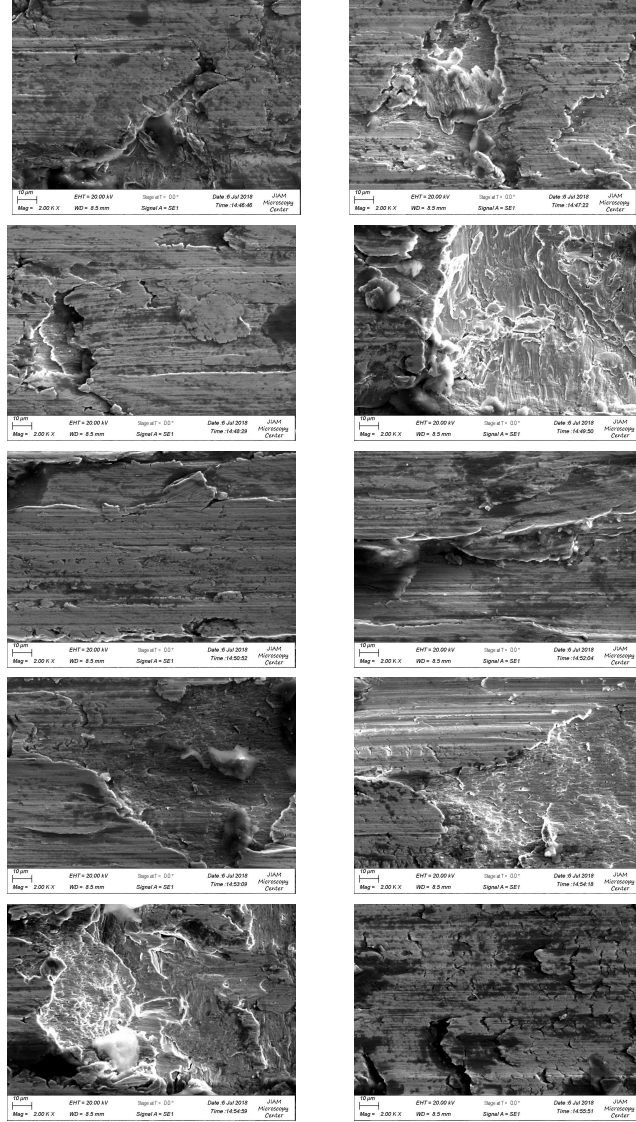
Figure A.3: SEM images at ten random locations on the fracture surface for an as-welded/204°C UAM SS410 sample.
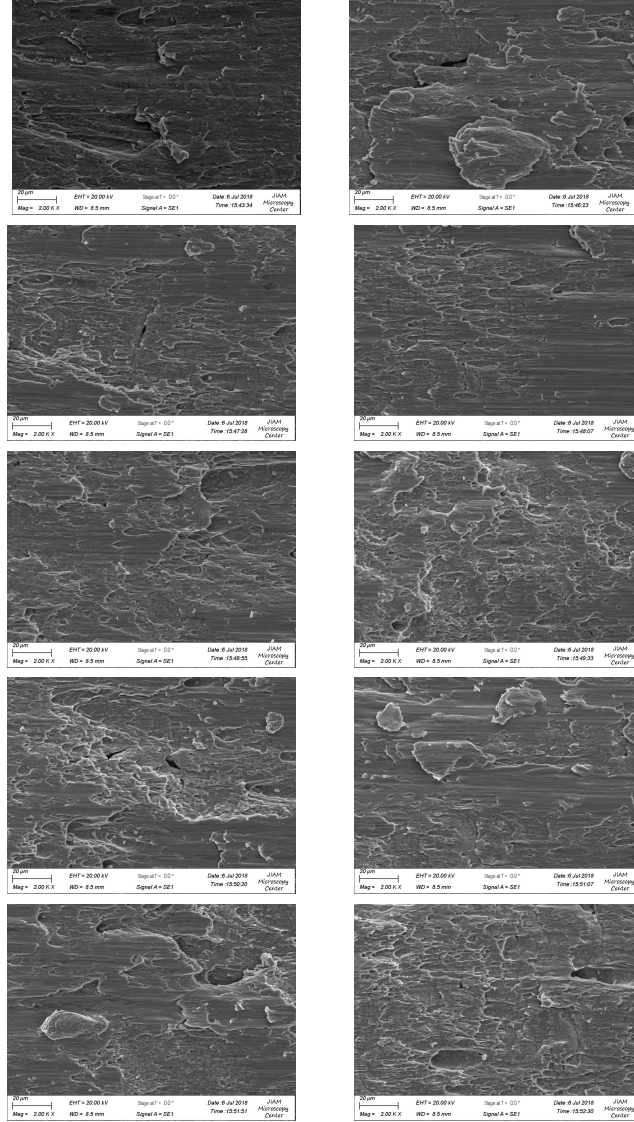
Figure A.4: SEM images at ten random locations on the fracture surface for a HIP/204°C UAM SS410 sample.

Appendix B

CAD Drawings of the Custom Shear Test Fixture

The fixture is composed of two identical "L" shape shearing blocks and two identical shearing plates. Shearing blocks are made of 4130 steel and shearing plates are made of heat treated S7 tool steel. The details of using this shear test fixture are provided in Chapter 2.1. Application examples of this shear testing method are also shown in Chapter 2.2 and 2.3. Only the drawings of the block and the plate are presented here.

Figure B.1: CAD drawing of the shearing block

150
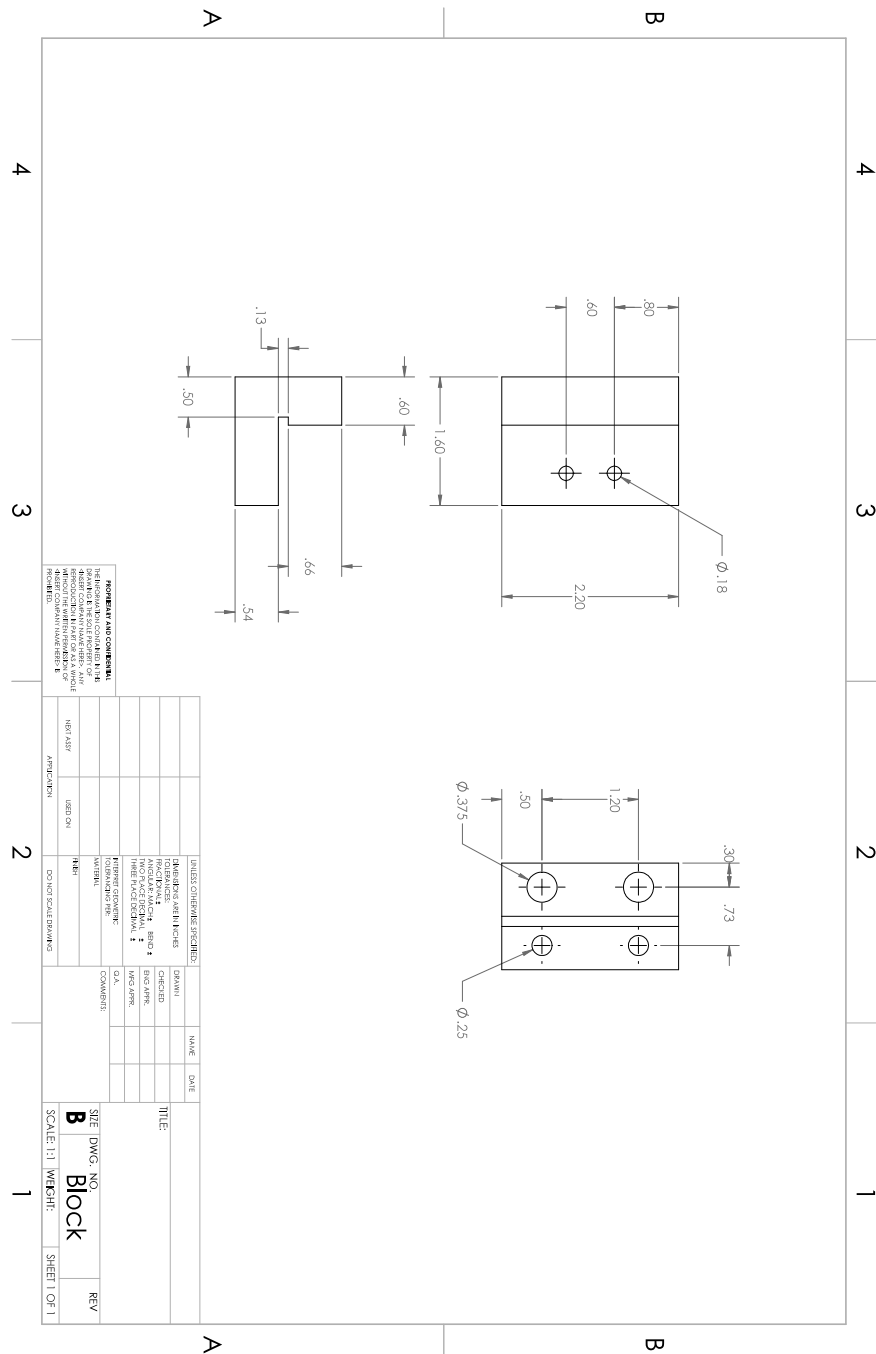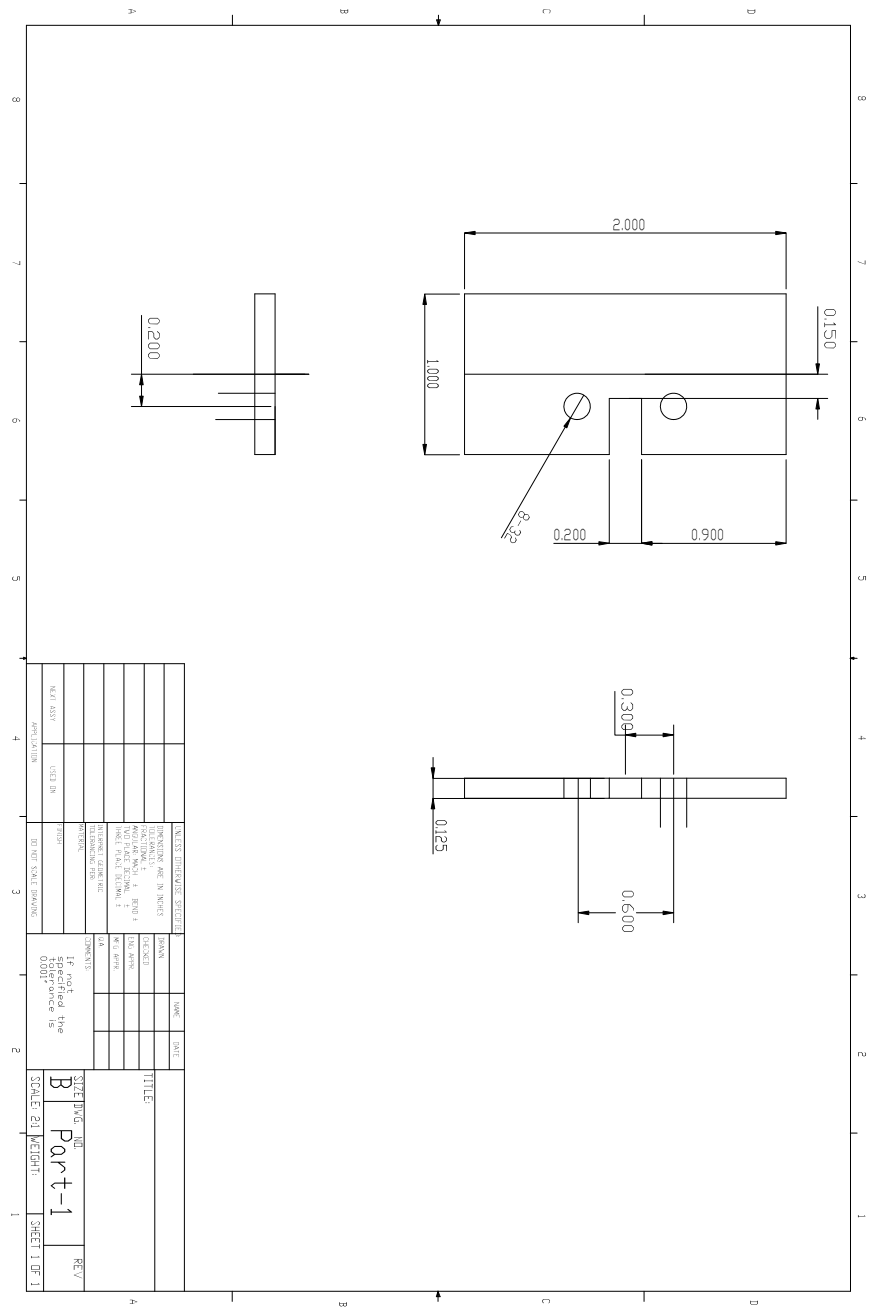
Figure B.2: CAD drawing of the shearing plate

Bibliography

[1] Mechanical properties of SAE-AISI 4130 (SCM430, G41300) Cr-Mo steel. *https://www.makeitfrom.com/material-properties/SAE-AISI-4130-SCM430-G41300-Cr-Mo-Steel*, [accessed 25 July 2020].

[2] Pearson product-moment correlation. *https://statistics.laerd.com/statistical-guides/pearson-correlation-coefficient-statistical-guide.php*, [accessed 25 July 2020].

[3] Shear strength of Al 6061 T6. *http://asm.matweb.com/search/SpecificMaterial.asp?bassnum=MA6061T6*, [accessed 05 October 2020].

[4] B. AlMangour, D. Grzesiak, and J.-M. Yang. Selective laser melting of TiB2/316L stainless steel composites: The roles of powder preparation and hot isostatic pressing post-treatment. *Powder Technology*, 309:37–48, 2017.

[5] B. AlMangour and J.-M. Yang. Improving the surface quality and mechanical properties by shot-peening of 17-4 stainless steel fabricated by additive manufacturing. *Materials & Design*, 110:914–924, 2016.

[6] K. An, L. Yuan, L. Dial, I. Spinelli, A. D. Stoica, and Y. Gao. Neutron residual stress measurement and numerical modeling in a curved thin-walled structure by laser powder bed fusion additive manufacturing. *Materials & Design*, 135:122–132, 2017.

[7] A. Borgenstam, L. Höglund, J. Ågren, and A. Engström. Dictra, a tool for simulation of diffusional transformations in alloys. *Journal of Phase Equilibria*, 21(3):269, 2000.

[8] D. Brown, J. Bernardin, J. Carpenter, B. Clausen, D. Spernjak, and J. Thompson. Neutron diffraction measurements of residual stress in additively manufactured stainless steel. *Materials Science and Engineering: A*, 678:291–298, 2016.

152

[9] J. Cao, M. A. Gharghouri, and P. Nash. Finite-element analysis and experimental validation of thermal residual stress and distortion in electron beam additive manufactured ti-6al-4v build plates. *Journal of Materials Processing Technology*, 237:409–419, 2016.

[10] L. W. Cheah. *Cars on a diet: the material and energy impacts of passenger vehicle weight reduction in the US*. PhD thesis, Massachusetts Institute of Technology, 2010.

[11] S. C. Davis, S. W. Diegel, R. G. Boundy, et al. Transportation energy data book. Technical report, Oak Ridge National Laboratory, 2015.

[12] S. T. de Freitas and J. Sinke. Adhesion properties of bonded composite-to-aluminium joints using peel tests. *The Journal of Adhesion*, 90(5-6):511–525, 2014.

[13] E. De Vries. *Mechanics and mechanisms of ultrasonic metal welding*. PhD thesis, The Ohio State University, 2004.

[14] D. C. Dean and J. Goldstein. Determination of the interdiffusion coefficients in the Fe-Ni and Fe-Ni-P systems below 900°c. *Metallurgical Transactions A*, 17(7):1131–1138, 1986.

[15] T. DebRoy, H. Wei, J. Zuback, T. Mukherjee, J. Elmer, J. Milewski, A. M. Beese, A. Wilson-Heid, A. De, and W. Zhang. Additive manufacturing of metallic components–process, structure and properties. *Progress in Materials Science*, 92:112–224, 2018.

[16] Z. Deng, M. B. Gingerich, T. Han, and M. J. Dapino. Yttria-stabilized zirconia-aluminum matrix composites via ultrasonic additive manufacturing. *Composites Part B: Engineering*, 151:215–221, 2018.

[17] R. Doherty, D. Hughes, F. Humphreys, J. Jonas, D. J. Jensen, M. Kassner, W. King, T. McNelley, H. McQueen, and A. Rollett. Current issues in recrystallization: a review. *Materials Science and Engineering: A*, 238(2):219–274, 1997.

[18] Y. Gao and X. Wu. Experimental investigation and fatigue life prediction for 7475-t7351 aluminum alloy with and without shot peening-induced residual stresses. *Acta Materialia*, 59(9):3737–3747, 2011.

[19] W. W. Gerberich, H. E. Martens, and R. A. Boundy. Tensile properties of five low-alloy and stainless steels under high-heating-rate and constant-temperature conditions. Technical report, Jet Propulsion Lab.(JPL), Pasadena, CA (United States), 1962.

[20] M. Ghasri-Khouzani, H. Peng, R. Rogge, R. Attardo, P. Ostiguy, J. Neidig, R. Billo, D. Hoelzle, and M. Shankar. Experimental measurement of residual stress and distortion in additively manufactured stainless steel components with various dimensions. *Materials Science and Engineering: A*, 707:689–700, 2017.

[21] T. Gnäupel-Herold, H. Prask, A. Clark, C. Hehman, and T. Nguyen. A comparison of neutron and ultrasonic determinations of residual stress. *Measurement Science and Technology*, 11(4):436, 2000.

[22] R. Gonzalez and B. Stucker. Experimental determination of optimum parameters for stainless steel 316l annealed ultrasonic consolidation. *Rapid Prototyping Journal*, 18(2):172–183, 2012.

[23] K. Graff, M. Short, and M. Norfolk. Very high power ultrasonic additive manufacturing (VHP UAM) for advanced materials. In *Solid freeform fabrication symposium, Austin, TX*, 2010.

[24] H. Guo, M. B. Gingerich, L. M. Headings, R. Hahnlen, and M. J. Dapino. Joining of carbon fiber and aluminum using ultrasonic additive manufacturing (UAM). *Composite Structures*, 208:180–188, 2019.

[25] R. Hahnlen and M. J. Dapino. NiTi-Al interface strength in ultrasonic additive manufacturing composites. *Composites Part B: Engineering*, 59:101–108, 2014.

[26] T. Han, C.-H. Kuo, N. Sridharan, L. M. Headings, S. S. Babu, and M. J. Dapino. Effect of preheat temperature and post-process treatment on the microstructure and mechanical properties of stainless steel 410 made via ultrasonic additive manufacturing. *Material Science and Engineering: A*, 769(2):138457, 2020.

[27] T. Han, C.-H. Kuo, N. Sridharan, L. M. Headings, S. S. Babu, and M. J. Dapino. Effect of weld power and interfacial temperature on mechanical strength and microstructure of carbon steel 4130 fabricated by ultrasonic additive manufacturing. *Manufacturing Letters*, 25:64–69, 2020.

[28] A. Hehr and M. J. Dapino. Interfacial shear strength estimates of NiTi-Al matrix composites fabricated via ultrasonic additive manufacturing. *Composites Part B: Engineering*, 77:199–208, 2015.

[29] A. Hehr and M. J. Dapino. Dynamics of ultrasonic additive manufacturing. *Ultrasonics*, 73:49–66, 2017.

[30] A. J. Hehr. *Process control and development for ultrasonic additive manufacturing with embedded fibers*. PhD thesis, The Ohio State University, 2016.

[31] D. Herzog, V. Seyda, E. Wycisk, and C. Emmelmann. Additive manufacturing of metals. *Acta Materialia*, 117:371–392, 2016.

[32] J. Hines and K. Vecchio. Recrystallization kinetics within adiabatic shear bands. *Acta Materialia*, 45(2):635–649, 1997.

[33] C. Hopkins, P. Wolcott, M. J. Dapino, A. Truog, S. Babu, and S. Fernandez. Optimizing ultrasonic additive manufactured Al 3003 properties with statistical modeling. *Journal of Engineering Materials and Technology*, 134(1):011004, 2012.

[34] N. Iosipescu. New accurate procedure for single shear testing of metals. *Journal of Materials*, 2:537–566, 1967.

[35] J. Jaeger. Moving heat sources and friction temperature. In *Proc. Roy. Soc. NSW*, volume 76, pages 203–224, 1942.

[36] P. Knysh and Y. P. Korkolis. Determination of the fraction of plastic work converted into heat in metals. *Mechanics of materials*, 86:71–80, 2015.

[37] S. Koellhoffer, J. W. Gillespie Jr, S. G. Advani, and T. A. Bogetti. Role of friction on the thermal development in ultrasonically consolidated aluminum foils and composites. *Journal of Materials Processing Technology*, 211(11):1864–1877, 2011.

[38] C. Kong, R. Soar, and P. Dickens. Characterisation of aluminium alloy 6061 for the ultrasonic consolidation process. *Materials Science and Engineering: A*, 363(1):99–106, 2003.

[39] C. Kong, R. Soar, and P. Dickens. Optimum process parameters for ultrasonic consolidation of 3003 aluminium. *Journal of Materials Processing Technology*, 146(2):181–187, 2004.

[40] C.-H. Kuo, N. Sridharan, T. Han, M. J. Dapino, and S. S. Babu. Ultrasonic additive manufacturing of 4130 steel using Ni interlayers. *Science and Technology of Welding and Joining*, 24(5):382–390, 2019.

[41] S. S. Lee, T. H. Kim, S. J. Hu, W. W. Cai, J. A. Abell, and J. Li. Characterization of joint quality in ultrasonic welding of battery tabs. *Journal of Manufacturing Science and Engineering*, 135(2):021004, 2013.

[42] A. Levy, A. Miriyev, N. Sridharan, T. Han, E. Tuval, S. S. Babu, M. J. Dapino, and N. Frage. Ultrasonic additive manufacturing of steel: method, post-processing treatments and properties. *Journal of Materials Processing Technology*, 256:183–189, 2018.

[43] G. Li and P. Wang. *Advanced analysis and design for fire safety of steel structures*. Springer Science & Business Media, 2013.

[44] T. J. Lienert, S. S. Babu, V. L. Acoff, N. Y. Zhou, E. DeGuire, S. Lampman, E. Marquard, B. Musgrove, and B. Riley. ASM Handbook. *Welding Fundamentals and Processes*, 2011.

[45] J. Lins, H. Sandim, H.-J. Kestenbach, D. Raabe, and K. Vecchio. A microstructural investigation of adiabatic shear bands in an interstitial free steel. *Materials Science and Engineering: A*, 457(1-2):205–218, 2007.

[46] T. Lolla, G. Cola, B. Narayanan, B. Alexandrov, and S. S. Babu. Development of rapid heating and cooling (flash processing) process to produce advanced high strength steel microstructures. *Materials Science and Technology*, 27(5):863–875, 2011.

[47] B. Million, J. Ržičková, J. Velíšek, and J. Vřešťál. Diffusion processes in the Fe-Ni system. *Materials Science and Engineering*, 50(1):43–52, 1981.

[48] J. Mollendorf. Thermal stresses from a lowing band source of heat on the surface of a semi-infinite solid. *Journal of Engineering for Industry*, 100:43, 1978.

[49] C. Moosbrugger. Atlas of stress-strain curves. *ASM international, Ohio*, page 299, 2002.

[50] L. Nickels. A new generation of hip. *Metal Powder Report*, 71(3):146–148, 2016.

[51] I. C. Noyan and J. B. Cohen. *Residual stress: measurement by diffraction and interpretation*. Springer, 2013.

[52] A. J. Rosakis, J. J. Mason, and G. Ravichandran. The conversion of plastic work to heat around a dynamically propagating crack in metals. *Journal of the Mechanical Behavior of Materials*, 4(4):375–386, 1993.

[53] S. Roy, T. Bose, and K. Debnath. Behaviour of glass fiber-reinforced composite with delamination under iosipescu shear test. In *International Journal of Modern Manufacturing Technologies*, pages 119–125, 2019.

[54] J. J. Schomer, A. J. Hehr, and M. J. Dapino. Characterization of embedded fiber optic strain sensors into metallic structures via ultrasonic additive manufacturing. In *SPIE Smart Structures and Materials+ Nondestructive Evaluation and Health Monitoring*, pages 980320–980320. International Society for Optics and Photonics, 2016.

[55] J. E. Shigley, R. G. Budynas, and C. R. Mischke. *Mechanical engineering design*. McGraw-hill, 2004.

[56] C. Shih, Y. Katoh, J. O. Kiggans, T. Koyanagi, H. E. Khalifa, C. A. Back, T. Hinoki, and M. Ferraris. Comparison of shear strength of ceramic joints determined by various test methods with small specimens. *Ceramic Materials fo Energy Application IV, John Wiley & Sons*, pages 139–149, 2015.

[57] S. Shimizu, H. Fujii, Y. Sato, H. Kokawa, M. Sriraman, and S. Babu. Mechanism of weld formation during very-high-power ultrasonic additive manufacturing of Al alloy 6061. *Acta Materialia*, 74:234–243, 2014.

[58] T. Simson, A. Emmel, A. Dwars, and J. Böhm. Residual stress measurements on aisi 316l samples manufactured by selective laser melting. *Additive Manufacturing*, 17:183–189, 2017.

[59] M. Smith. *ABAQUS/Standard User's Manual, Version 6.9*. Dassault Systèmes Simulia Corp, United States, 2009.

[60] R. T. Smith. *Development of a nitrogen-modified stainless-steel hardfacing alloy*. PhD thesis, The Ohio State University, 2015.

[61] N. Sridharan, E. Cakmak, and R. R. Dehoff. Microstructure evolution during laser direct energy deposition of a novel Fe-Cr-Ni-WB hardfacing coating. *Surface and Coatings Technology*, 358:362–370, 2019.

[62] N. Sridharan, R. R. Dehoff, B. H. Jordan, and S. S. Babu. Development of coatings for ultrasonic additive manufacturing sonotrode using laser direct metal deposition process. Technical report, Oak Ridge National Lab.(ORNL), Oak Ridge, TN (United States), 2016.

[63] N. Sridharan, M. Gussev, R. Seibert, C. Parish, M. Norfolk, K. Terrani, and S. Babu. Rationalization of anisotropic mechanical properties of Al-6061 fabricated using ultrasonic additive manufacturing. *Acta Materialia*, 117:228–237, 2016.

[64] N. Sridharan, M. N. Gussev, C. M. Parish, D. Isheim, D. N. Seidman, K. A. Terrani, and S. S. Babu. Evaluation of microstructure stability at the interfaces of Al-6061 welds fabricated using ultrasonic additive manufacturing. *Materials Characterization*, 139:249–258, 2018.

[65] N. Sridharan, M. Norfolk, and S. S. Babu. Characterization of steel-Ta dissimilar metal builds made using very high power ultrasonic additive manufacturing (VHP-UAM). *Metallurgical and Materials Transactions A*, 47(5):2517–2528, 2016.

[66] N. Sridharan, P. Wolcott, M. Dapino, and S. S. Babu. Microstructure and mechanical property characterisation of aluminium-steel joints fabricated using ultrasonic additive manufacturing. *Science and Technology of Welding and Joining*, 22(5):373–380, 2017.

[67] N. Sridharan, P. Wolcott, M. J. Dapino, and S. Babu. Microstructure and texture evolution in aluminum and commercially pure titanium dissimilar welds fabricated using ultrasonic additive manufacturing. *Scripta Materialia*, 117:1–5, 2016.

[68] M. Sriraman, S. S. Babu, and M. Short. Bonding characteristics during very high power ultrasonic additive manufacturing of copper. *Scripta Materialia*, 62(8):560–563, 2010.

[69] M. Sriraman, M. Gonser, D. Foster, H. T. Fujii, S. Babu, and M. Bloss. Thermal transients during processing of 3003 Al-H18 multilayer build by very high-power ultrasonic additive manufacturing. *Metallurgical and Materials Transactions B*, 43(1):133–144, 2012.

[70] M. R. Sriraman, M. Gonser, H. T. Fujii, S. S. Babu, and M. Bloss. Thermal transients during processing of materials by very high power ultrasonic additive manufacturing. *Journal of Materials Processing Technology*, 211(10):1650–1657, 2011.

[71] Q. Sun, H.-N. Dui, and X.-L. Fan. A statistically consistent fatigue damage model based on miner's rule. *International Journal of Fatigue*, 69:16–21, 2014.

[72] J. Takahashi, K. Kawakami, and M. Ueda. Atom probe tomography analysis of the white etching layer in a rail track surface. *Acta Materialia*, 58(10):3602–3612, 2010.

[73] R. B. Tuttle. Feasibility study of 316l stainless steel for the ultrasonic consolidation process. *Journal of Manufacturing Processes*, 9(2):87–93, 2007.

[74] M. Uday, M. Ahmad-Fauzi, A. M. Noor, S. Rajoo, et al. Current issues and problems in the joining of ceramic to metal. In *Joining Technologies*. IntechOpen, 2016.

[75] A. A. Ward, Y. Zhang, and Z. C. Cordero. Junction growth in ultrasonic spot welding and ultrasonic additive manufacturing. *Acta Materialia*, 158:393–406, 2018.

[76] P. Withers, M. Preuss, A. Steuwer, and J. Pang. Methods for obtaining the strain-free lattice parameter when using diffraction to determine residual stress. *Journal of Applied Crystallography*, 40(5):891–904, 2007.

[77] C. Wittman, M. Meyers, and H.-R. Pak. Observation of an adiabatic shear band in aisi 4340 steel by high-voltage transmission electron microscopy. *Metallurgical Transactions A*, 21(2):707–716, 1990.

[78] P. Wolcott, N. Sridharan, S. Babu, A. Miriyev, N. Frage, and M. J. Dapino. Characterisation of Al-Ti dissimilar material joints fabricated using ultrasonic additive manufacturing. *Science and Technology of Welding and Joining*, 21(2):114–123, 2016.

[79] P. J. Wolcott and M. J. Dapino. Ultrasonic additive manufacturing. In *Additive Manufacturing Handbook: Product Development for the Defense Industry*. CRC Press/Taylor and Francis Boca Raton, Florida, 2017.

[80] P. J. Wolcott, A. Hehr, and M. J. Dapino. Optimized welding parameters for Al 6061 ultrasonic additive manufactured structures. *Journal of Materials Research*, 29(17):2055–2065, 2014.

[81] I. Wolf, H. Grabke, and P. Schmidt. Carbon transport through oxide scales on Fe-Cr alloys. *Oxidation of Metals*, 29(3-4):289–306, 1988.

[82] W. Woo, D.-K. Kim, E. J. Kingston, V. Luzin, F. Salvemini, and M. R. Hill. Effect of interlayers and scanning strategies on through-thickness residual stress distributions in additive manufactured ferritic-austenitic steel structure. *Materials Science and Engineering: A*, 744:618–629, 2019.

[83] X. Wu, T. Liu, and W. Cai. Microstructure, welding mechanism, and failure of Al/Cu ultrasonic welds. *Journal of Manufacturing Processes*, 20:321–331, 2015.

[84] C. S. Zhang, A. Deceuster, and L. Li. A method for bond strength evaluation for laminated structures with application to ultrasonic consolidation. *Journal of Materials Engineering and Performance*, 18(8):1124, 2009.